GRAPHENE@MICROALGAE-BASED NANOHYBRID STRUCTURES AS ADSORBENTS FOR REMOVAL OF Cr(VI) IONS IN AQUEOUS SOLUTIONS

R. MULOVHEDZI

2024

NELSON MANDELA UNIVERSITY

GRAPHENE@MICROALGAE-BASED NANOHYBRID STRUCTURES AS ADSORBENTS FOR REMOVAL OF Cr(VI) IONS IN AQUEOUS SOLUTIONS

By

ROLIVHUWA MULOVHEDZI

A treatise submitted in partial fulfilment of the requirements for the degree of Magister Scientiae: Nanoscience (Coursework) to be awarded at the Nelson Mandela University

DECEMBER 2024

Supervisor : Prof SD MHLANGA

Co-supervisors : Dr AS OGUNLAJA

: Dr K YOKWANA

DECLARATION

I, Rolivhuwa Mulovhedzi of student number 226115755, hereby declare that the treatise/ dissertation/ thesis for MSc (Nanoscience) Coursework/Research is my own work and has not previously been submitted for assessment or completion of any other postgraduate qualification at any other university or tertiary institution. The report does not contain any other person's writing unless specifically acknowledged and referenced accordingly.

……

Rolivhuwa Mulovhedzi

Official use:

In accordance with Rule G5.11.4, I hereby declare that the above-mentioned treatise/ dissertation/ thesis is my own work and that it has not previously been submitted for assessment to another University or for another qualification. However, material from publications by the student may be embodied in a treatise/dissertation/ thesis

DEDICATION

This work is dedicated to my mother, N.S. Maguvhe, my father, M.E. Mulovhedzi, and my daughter, Wamashudu Angel-sent. Their love, support, and encouragement were important to my determination and perseverance to accomplish this work.

ACKNOWLEDGEMENTS

First and foremost, I would like to thank the Almighty God, who has bestowed upon me the fortitude to reach this point. Once again, I would like to extend my sincere appreciation to the following individuals and organizations for their aid and support throughout my master's study period:

- I would like to convey my heartfelt gratitude to my supervisor, Prof. S.D. Mhlanga, for his exceptional mentorship, valuable counsel, and unwavering patience during my research. I would like to express my gratitude to my co-supervisor, Dr. A.S. Ogunlaja, for his invaluable assistance, insightful recommendations, and considerate remarks in guiding my research endeavours.
- My deepest gratitude goes to my co-supervisor, Dr. K. Yokwana, for her unrelenting dedication, inspiration, and kind guidance during my research project. Furthermore, I appreciate her enthusiasm for assisting with the laboratory work and proofreading of this dissertation.
- I would also like to convey my affection and appreciation to my cherished family for the immense love and unwavering support they have bestowed upon me throughout my existence. To be specific, my mother, N.S. Maguvhe, and my father, M.E. Mulovhedzi, for their unwavering trust and consistent support during my academic journey. My sincere thanks also go to the source of my strength, my daughter Wamashudu, for always understanding that mommy must pursue her dreams.
- Special thanks go to my friends, for their prayers, support, and advice, which provided me with the necessary motivation and guidance during my academic journey, regardless of the circumstances.
- InnoVenton: Institute for Chemical Technology for providing us with microalgae biomass samples to use in this work.
- I wish to express my profound gratitude to the Nelson Mandela University and the Department of Chemistry for providing a conducive research environment and facilities that made all this work possible. Finally, my sincere appreciation to the Department of Science and Innovation (DSI) for financial assistance.

PRESENTATIONS AND PUBLICATIONS

The research outcomes derived from this study have been presented at regional conferences and will be submitted to peer-reviewed journals for publication.

Publications:

1. R. Mulovhedzi, K. Yokwana, A.S. Ogunlaja, S.D. Mhlanga. Ultrasonic-assisted synthesis of nanostructured graphene oxide@algae nanohybrids for the removal of Cr(VI) from aqueous solutions. (Under preparation to be submitted by Feb-March 2024).

Presentations:

1. R. Mulovhedzi, K. Yokwana, A.S. Ogunlaja, S.D. Mhlanga. Synthesis of nanostructured graphene oxide@algae composite materials for the removal of Cr(VI) from aqueous solutions. **Poster presentation**. 11th Annual Eastern Cape Nanosciences Young Researcher's Symposium (NYRS) held at Nelson Mandela University on the 07 of September 2023. The poster won the 3rd best poster award in the Master's category.

2. R. Mulovhedzi, K. Yokwana, A.S. Ogunlaja, S.D. Mhlanga. Synthesis of nanostructured graphene oxide@algae composite materials for the removal of Cr(VI) from aqueous solutions. **Oral presentation**. The Eskom Water and Wastewater Technologies Conference will be held at Eskom Academy of Learning, Midrand, Johannesburg, South Africa from 28 February – 1 March 2024.

ABSTRACT

The efficient removal of heavy metals using carbon-based nanoadsorbents poses a substantial challenge in the domain of water purification. Graphene-based materials have been extensively utilised in the treatment of water and wastewater due to their tremendous surface areas, porosity, turntable nature to different functional groups, and photo-catalytic properties. In this project, graphene oxide (GO) was synthesised *via* the modified Hummers method. A similar method was used to produce nitrogen-doped graphene oxide (NGO), with urea as the nitrogen precursor. Utilising biomass materials to dope graphene-based nanocomposites can effectively enhance their application in water treatment.

In this work, graphene oxide-microalgae (GO@Algae) and N-doped graphene oxide-microalgae (NGO@Algae) nanocomposites were synthesised by combining GO or NGO with green *Scenedesmus* microalgae. This was done through a solution self-assembly mixing method using ultrasonication. The resulting nanocomposites were used to remove Cr(VI) from water solutions. The influence of microalgae content deposited on GO and NGO nanosheets at different weight ratios (1:1, 3:1, and 1:3) on the chemical, structural, morphological, and thermal characteristics of nanoadsorbents was evaluated using various techniques such as Brunauer-Emmett-Teller (BET), scanning electron microscopy (SEM), thermogravimetric analysis (TGA), Fourier Transform Infrared Spectroscopy (FT-IR), X-ray diffraction (XRD) and X-ray photoelectron spectroscopy (XPS). The flat nanosheet-like morphology of GO@Algae and NGO@Algae nanostructured materials was observed through SEM, confirming microalgae's incorporation within the GO and NGO matrices. The thermal stability and surface area properties of GO and NGO nanocomposite materials decreased with the incorporation of microalgae content. The incorporation of microalgae into GO nanosheets showed enhancements in chemical and structural properties due to the presence of the strong covalent interaction (oxygen and nitrogen-containing groups) between the interfaces of nanocomposites. XPS and FT-IR analyses revealed the existence of amides, carboxylic acids, and phosphates, which exhibited positive charges below the pH 2.03 point-of-zero charge.

The second phase of the study involved assessing the adsorption capabilities of the GO, NGO nanosheets, and GO@Algae and NGO@Algae nanocomposites in removing Cr(VI)

from the water solution. Adsorption parameters such as the effect of solution pH, contact time, adsorbent dosage and metal ion concentrations were evaluated for Cr(VI) removal. When comparing GO, NGO, GO@Algae, and NGO@Algae, it was found that GO@Algae and NGO@Algae exhibited superior adsorption performance due to the available functional groups and well-developed pores. Additionally, a mixed ratio of GO or NGO and algae at a ratio of 1:3 was found to be the most suitable for GO@Algae and NGO@Algae. The adsorption efficiency of nanostructured materials for Cr(VI) is significantly influenced by their surface charge, porosity and specific surface area. The results revealed that the adsorption capabilities of GO@Algae (1:3) and NGO@Algae (1:3) were 2.24 and 2.01 times higher than GO and NGO which were 1.64 and 1.89, respectively, at a solution of pH 2 where $HCrO_4^-$ species are predominant compared to a solution of pH 5 which predominate a mix of $Cr_2O_7^{2-}$ and CrO_4^{2-} species. The enhanced performance of the GO@Algae and NGO@Algae nanocomposites is attributed due to their increased surface functionalities and porosity. The adsorption of Cr(VI) ions by the GO/NGO@Algae nanocomposites declined with increasing initial concentration of Cr(VI) species in the water medium. The adsorption kinetics data for GO, NGO, GO@Algae (1:3), and NGO@Algae (1:3) exhibited a good fit with the pseudo-second-order model ($R^2 > 0.995$) suggesting that chemisorption governed the adsorption process. Similarly, the isotherm adsorption findings showed a good fit with the Freundlich model ($R^2 > 0.961$). The findings indicated that the adsorption mechanism process was characterised by monolayer adsorption onto a heterogeneous adsorbent surface. Furthermore, the GO@Algae (1:3) was found to have the maximum adsorption capacity of 10.85 mg/g surpassing the capacities of both unmodified and NGO@Algae counterparts. The application of GO@Algae and NGO@Algae has the potential to promote the green reuse of graphene-based nanomaterials. In summary, GO@Algae and NGO@Algae show great potential as eco-friendly adsorbents for the feasible treatment of heavy metal-contaminated water.

TABLE OF CONTENTS

LIST OF FIGURES

LIST OF TABLES

LIST OF ABBREVIATIONS

AC	Activated carbon
BET	Brunuer-Emmett-Teller
CBNMs	Carbon-based nanomaterials
CNTs	Carbon nanotubes
DSC	Differential Scanning Calorimetry
DTG	Differential thermogravimetric
FT-IR	Fourier transform infrared spectroscopy
GN	Graphene
GO	Graphene oxide
IPD	Intraparticle diffusion
MWCNTs	Multi-walled carbon nanotubes
NGO	Nitrogen-doped graphene oxide
PFO	Pseudo-first order
PSO	Pseudo-second order
rGO	Reduced graphene oxide
rpm	Revolutions per minute
SEM	Scanning electron microscopy
SWCNTs	Single-walled carbon nanotubes
TGA	Thermogravimetric Analysis
UV-Vis	Ultraviolent–Visible spectrophotometer
WHO	World Health Organization
XPS	X-ray photoelectron spectroscopy
XRD	X-ray diffraction

CHAPTER 1:
INTRODUCTION

1.1 Background

Natural resources such as clean water are becoming increasingly scarce around the world because of population growth, economic upheaval, and climate change. The emergence of the water, energy, and food (WEF) nexus has provided a paradigm for comprehending interdependencies and effectively managing resources at different levels (Mabhaudhi et al., 2019). Water constitutes 50% to 90% of the mass of all living organisms, rendering it a vital constituent for the sustenance of life on our planet. In addition to being essential for maintaining life and health, industry and agriculture also play a crucial role in sustaining local and national economies. Water is essential to everything we do daily, ranging from industrial processes to agricultural pursuits, and we are completely reliant on it. Furthermore, a mere 3% of the freshwater found on Earth's crust is accessible for human use, while the remaining 97% is seawater. Most of the freshwater is confined within ice caps and glaciers, accounting for 68.7% of the available 3% of freshwater on Earth as shown in Figure 1.1 (Sharma et al., 2011). However, the amount of freshwater has been decreasing over time, making clean water a scarce resource. The primary causes of this can be mainly ascribed to the subsequent factors:

(i) Rising water consumption and declining water quality standards.

(ii) Owing to disparities in climate, population expansion, economic level, and culture, different nations exhibit significant variations in their water requirements. Studies have indicated an increase in population growth in several regions worldwide, namely in the sub-Saharan area of Africa. Consequently, there is a greater need for water to fulfil the demands of these individuals (Mabhaudhi et al., 2019).

(iii) The causes of poor water quality are diverse and include several human endeavours, including industrial operations and urbanisation (such as battery, tannery, textile, domestic sewage, mine, and smelting industries), and

agricultural practices. These activities have the potential to contaminate water both organically and inorganically (Abiodun et al., 2023; Baby et al., 2019).

The presence of these waterborne contaminants has detrimental effects on human health and aquatic ecosystems since they enter the body through water consumption and contribute to the development of various diseases (Anfar et al., 2020; Yang et al., 2019). Approximately two-thirds of the African continent consists of arid or semi-arid regions, with over 300 million individuals residing in water-scarce areas within sub-Saharan Africa. Every hour, 115 individuals in Africa succumb to illnesses associated with inadequate sanitation, hygiene, and polluted water sources. Factors such as population growth, urban development, and heightened water demands in households and industries exacerbate this situation (WHO, 2023). For instance, several regions in rural South Africa, including the Eastern Cape Province, continue to lack access to potable and uncontaminated water. The rural areas of the province are experiencing a significant impact. Water scarcity is a pressing concern, as populations continue to rely on rivers as their primary water source, which is also shared with domestic livestock. The government's endeavours to ensure universal access to clean water have proven unsuccessful in numerous aspects. Approximately 24% of households in the province depend on inadequate water sources. Residents utilise this water for culinary purposes, drinking, and laundering garments, frequently leading to diseases associated with colon-related infections. Therefore, it is essential to investigate and create practical, easy-to-use and efficient heavy metal removal techniques in order to provide clean water, especially in remote areas.

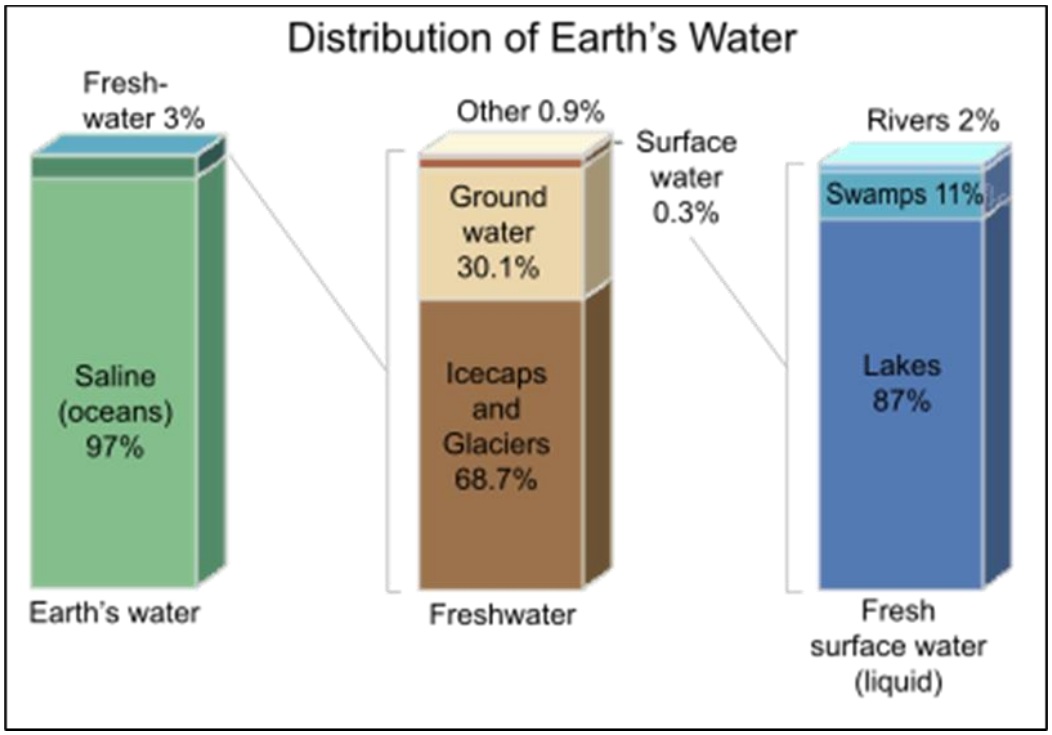

Figure 1.1: Distribution of the Earth's Water (Sharma et al., 2011)**.**

1.2 Problem Statement

Heavy metals are widely recognised as highly hazardous contaminants in water. The increasing issue of heavy metal contamination is becoming a significant cause for alarm, especially in developing nations because of the growing prevalence of industrial and urban activities. Significant sources of pollution include solid waste disposal and waste recycling operations, as well as the release of contaminated wastewater from a variety of sectors, such as coal-fired power stations and mining operations (Sabzehmeidani et al., 2021; Yang et al., 2019). For example, South Africa (SA) possesses 75% of the global viable chromite ore reserves. It is also the primary producer of ferrochrome in the Western Bushveld Complex worldwide. The Merensky Reef, stretching from Rustenburg to Marikana, contains the largest concentration of extractable chromite. The activities of chromite-mining and ferrochrome industries not only contaminate the land and water but also play a significant role in air pollution (Coetzee et al., 2020). Indeed, a wide range of pollutants are frequently identified in different water sources, such as wastewater, groundwater, surface water, and even potable water. Even at low levels, the existence of heavy metals can have harmful effects on aquatic ecosystems and human health. This is because they tend to bioaccumulate in species, such as fish, as they go up the food chain, which can cause both immediate and

long-term damage. Hence, it is imperative to implement immediate mitigation measures to eliminate perilous contaminants, thereby safeguarding aquatic ecosystems and, eventually, human well-being from potential contact. Exposure to chromium and lead, for instance, can result in many different health problems, including anaemia, lung cancer, nephropathy, gastrointestinal colic, central nervous system disorders and many other serious diseases (McNeill et al., 2012; Padmavathy et al., 2016).

Hence, it is necessary to undertake the remediation of these hazardous heavy metals prior to the disposal of wastewater effluent. Various technologies have been created and implemented with varying degrees of success. The methods encompass coagulation, membrane separation techniques, advanced oxidation processes, biological treatments, chemical precipitation, and adsorption (Matebese and Moutloali, 2022; Pillay et al., 2009; Stylianou et al., 2015; Yang et al., 2019). Due to their ease of use, and environmental friendliness, adsorption techniques have become a preferred technique for successfully removing heavy metals from wastewater (Gusain et al., 2020; Nasrollahzadeh et al., 2021). The adsorption efficiency varies depending on the specific nanoadsorbent used. Hence, the exploration of novel categories of adsorbents and their utilisation for the elimination of heavy metals has emerged as the primary focus and obstacle for environmental remediation researchers worldwide.

Graphene (GN) and its derivatives, including reduced graphene oxide (rGO) and graphene oxide (GO), are currently the most commonly used carbon-based nanostructured adsorbents in water remediation processes because of their high specific surface area, high oxygen-containing surface functionalities, highly porous structure, and flexibility for surface modification. (Brito et al., 2023; De Beni et al., 2022). Although GN, graphite, GO, and rGO possess exceptional characteristics, they tend to agglomerate in water-based solutions, resulting in a loss in their ability to effectively remove contaminants on account of the decrease in surface area. In order to reduce the agglomeration of these graphene nanosheets, their surface can be altered through the incorporation of surfactants and polymers, heteroatom doping, or they can be combined with other nanomaterials to produce graphene-based nanocomposites (De Beni et al., 2022; Lian et al., 2020; Lingamdinne et al., 2017). This approach has been proven to be effective in enhancing their stability, properties, and adsorption performance. Therefore, there is a demand for the creation of eco-friendly

adsorbents that are both renewable and possess a strong adsorption capacity and regeneration potential.

1.3 Justification

The primary goal of water treatment is to generate water that is uncontaminated and suitable for its intended consumptive use. GO-based nanomaterials have been extensively used for this purpose, and their efficacy has been demonstrated due to their substantial porous structure, large surface area, high capacity, and hydrophilic characteristics (Abdelfattah et al., 2023; Hussain et al., 2021; Kumar et al., 2021). However, GO-based nanoadsorbents have notable challenges in terms of regeneration. Consequently, current research is now concentrating on utilising microalgae for modification to provide renewable adsorbent. Microalgae biomasses possess a substantial amount of protein, carbohydrates, lipids, and chitin. Their tissues consist of various polysaccharides that are connected to the inner fibrous structure and the outer amorphous matrix inside the cells. In addition, microalgae cells possess many functional groups, including hydroxyl, carboxylic acid, phosphates, sulfate, amide, carbonyl, halides, and ether, which facilitate the biosorption of heavy metals as they can act as binding sites. Therefore, this study has established the need to integrate microalgae cells onto a support material composed of GO nanosheets (matrix). This matrix functions to immobilise the algae cells while facilitating their exposure to aquatic environments for interaction. As a result, it reduces the agglomeration of GO nanosheets, enhances their regeneration, improves their properties, decreases the expenses associated with graphene-based nanoadsorbent, and enhances their ability to adsorb toxic heavy metal ions such as cadmium, copper, arsenic, and chromium from wastewater.

1.4 Aim

The aim of this study was to develop novel nanostructured graphene-microalgae biomass hybrid materials that possess a high capacity for removing Cr(VI) ions from aqueous solutions.

1.5 Objectives of the study

The specific objectives of the study were as follows:

(i) To synthesise GO and NGO nanostructured materials or nanosheets using the Hummers method.

(ii) To modify the GO and NGO nanosheets by reinforcing them with microalgae through the self-assembly technique.

(iii) To Analyse the surface morphology, thermal properties, and chemical structure of the synthesized nanocomposites using various techniques such as FT-IR spectroscopy, BET analysis, Zeta potential distribution, SEM, XRD, TGA, and XPS.

(iv) To conduct batch adsorption experiments in order to identify the most effective conditions for removing Cr(VI) of synthesised GO@Algae and NGO@Algae nanocomposites. The study examined several factors including initial adsorbate concentration, pH, contact time, and adsorbent dose.

(v) To evaluate the adsorption kinetics and isotherm models of the experimental data collected from the batch adsorption equilibrium, by fitting the data to different adsorption isotherms and kinetic models. To assess the efficiency and mechanism by which the adsorbents remove Cr(VI) from a water-based solution.

1.6 Research hypotheses

The introduction of microalgae into GO and NGO lattices offers extra active sites that could play an important role in improving their properties, such as surface area, surface chemistry, and structural defects. The properties will facilitate efficient contact with metal ions and active adsorption sites, subsequently enhancing adsorption performance. Therefore, we anticipate that graphene@microalgae-based nanohybrids will exhibit high removal efficiency in the adsorption of Cr(VI) ions from water solutions.

1.7 Research questions

- Does incorporating microalgae into GO and NGO nanostructures have an effect on their properties, such as morphology, surface area, surface chemistry, hydrophilicity, and thermal stability?
- What impact does microalgae have on the characteristics of GO and NGO in relation to the elimination of Cr (VI)?
- Will the adsorption capabilities of GO and NGO nanosheets be enhanced by modifying them with microalgae biomass?
- Which of the GO-algae and NGO-algae-based nanostructured materials will have the highest Cr(VI) ion removal performances?

1.8 Significance of the study

The significance of this research lies in the advancement of adsorption technology to address the issue of water contamination caused by Cr(VI) ions. It aids in mitigating the challenges related to wastewater treatment and management in industrial sectors. Additionally, it offers details regarding the altered graphene@microalgae-based nanoadsorbent and urges relevant entities to do further investigation on the subject and its associated fields.

1.9 Project outline

The thesis outline provides a concise overview of the topics that will be addressed in each chapter:

Chapter 1: Focuses on the rationale behind the synthesis of graphene@microalgae-based nanohybrids (GO@Algae and NGO@Algae).

Chapter 2: This chapter provides a comprehensive literature review that elucidates the present state of water source contamination caused by heavy metal ions and their impact on human health. Moreover, this chapter provides an overview of adsorption as an effective technique for water separation. It also provides a discussion on various carbon-based adsorbents and graphene-based adsorbents.

Chapter 3: Provides a comprehensive explanation of the materials, experimental methodologies, and instrumentation methods employed to characterise the graphene@microalgae-based nanohybrids. As well as the evaluation of efficacy and adsorption experiments for Cr(IV) ions onto the surfaces of graphene@microalgae-based nanohybrids.

Chapter 4: This chapter discusses the results and analysis of the characterisation and adsorption studies performed on graphene@microalgae-based nanohybrids before and after adsorption.

Chapter 5: Provides the overall conclusions and recommendations derived from this study, as well as suggestions for future research to improve the adsorption capabilities of nanostructured graphene@microalgae-based nanocomposites.

CHAPTER 2:

REMOVAL OF HEAVY METALS USING GRAPHENE-BASED AND BIOMASS ADSORBENTS: LITERATURE REVIEW

2.1 Heavy metal remediation techniques

Heavy metals are components of the earth's crust. They have distinct metallic characteristics and are dense. Furthermore, they adversely affect human health and the environment. Human health can be seriously threatened by exposure Cd^{2+}, Zn^{2}, Cu^{2+}, Cr^{3+}, Hg^{2+}, Mn^{2+}, Pb^{2+}, and As^{2+}, and these risks are growing daily because of industrialisation (Priya et al., 2022; Yang et al., 2019). Chromium (Cr) is categorised as a hazardous heavy metal ion. Chromium exists in two forms: trivalent (III), which is a pollutant with low levels of hazard and may be easily absorbed by different adsorbents in alkaline or neutral conditions, and hexavalent (VI), as illustrated in Figure 2.1. Due to its high solubility and mobility, Cr(VI) is highly hazardous and can be more readily absorbed by the human body through eating, inhalation, and skin contact compared to Cr(III). In addition, Cr(VI), in the forms of chromate (CrO_4^{2-}), dichromate ($Cr_2O_7^{2-}$), or hydrochromate ($HCrO_4^{-}$), enters the cell by a nonspecific anion channel using facilitated diffusion. On the other hand, Cr(III) enters the cell through passive diffusion or phagocytosis (Al-Homaidan et al., 2018). Prolonged exposure to Cr(VI) has the potential to induce various health complications, including respiratory distress, fibrosis, and cancer. As per the standards set by the United States Environmental Protection Agency (US EPA), the allowable concentrations of Cr(VI) in potable water and wastewater are 20 and 200 $\mu g\ L^{-1}$, respectively (Jung et al., 2013).

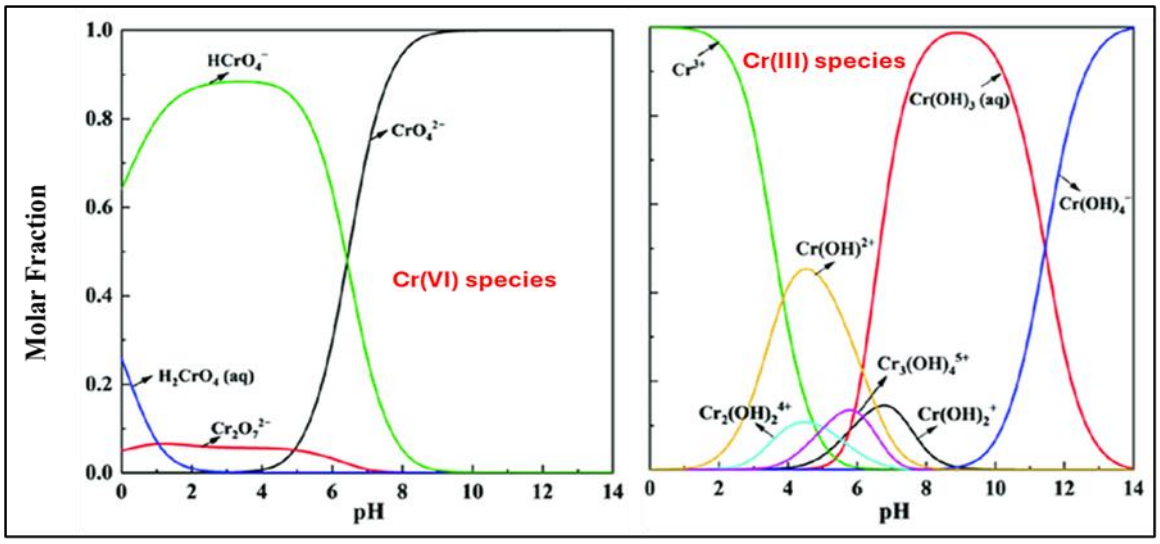

Figure 2.1: Chromium speciation diagram as a function of pH **(Yuan et al., 2023).**

Diverse strategies have been employed to address the issue of heavy metals; they encompass both traditional and innovative techniques that can be categorised into physical, chemical, and biological ways, as seen in Figure 2.2. The methods used include (i) advanced oxidation processes (AOPs), which function by generating hydroxyl radicals, and technologies (AOTs); (ii) biological treatments; (iii) membrane separation processes; (iv) coagulation/flocculation; (v) chemical precipitation and (vi) adsorption with varying levels of success (Baby et al., 2019; Matebese and Moutloali, 2022; Stylianou et al., 2015. Although these processes offer significant benefits in terms of rapid efficiency, they also have several downsides. These include the production of by-products that can be more detrimental than the intended component and the possible requirement for large quantities of chemicals and energy and they have sludge disposal requirement. Membrane separation technology can be adversely affected by extremely polluted waters, resulting in significant membrane fouling. This issue necessitates substantial initial investment and energy consumption (Abiodun et al., 2023; Priya et al., 2022). Biological approaches are known for their slow pace and complexity, requiring careful maintenance to maintain an environment conducive to microbial growth with limited ability to degrade specific chemicals. Adsorption is a particularly advantageous technique when compared among these options owing to its numerous merits, such as convenient manipulation, design simplicity, high selectivity, high separation efficiency, and outstanding removal efficacy (Piekarski et al., 2022; Yang et al., 2019).

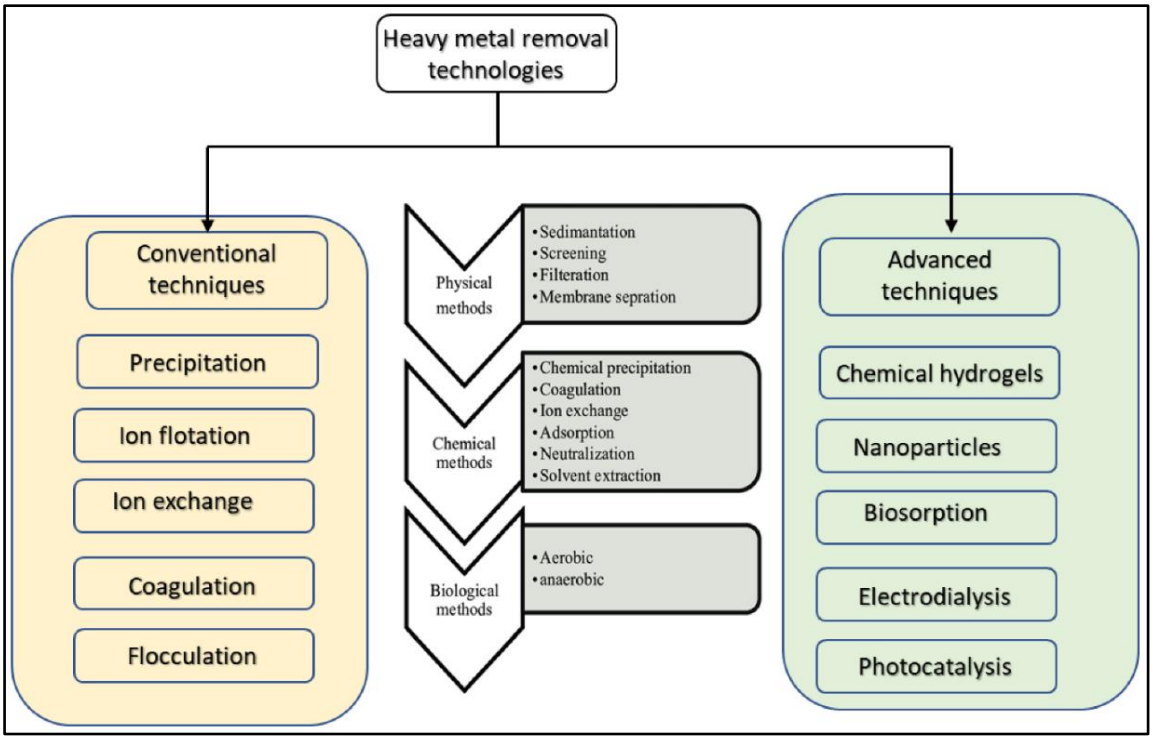

Figure 2.2: Common procedures for remediating metal ions from wastewater (Abiodun et al., 2023).

2.2 Adsorption process

Adsorption is the mechanism through which molecules of the solute (adsorbate) are transferred from the bulk fluid phase to the surface of a solid adsorbent. The adsorption process at the solid-liquid interface consists of three primary phases. The following are the sequential mechanistic steps: The process involves three steps: (a) the solute adsorbate diffuses from the bulk aqueous phase to the surface of the adsorbent through film diffusion; (b) Subsequently, it is adsorbed at the available binding sites that are specifically targeted on the adsorbent surface; and finally the adsorbate molecules internally diffuse within the solid adsorbent through either pore diffusion or bonded to a solid surface (Abiodun et al., 2023; Baby et al., 2019).

In simple terms, the adsorption of heavy metals in the aqueous phase can be defined as a phenomenon wherein a solid adsorbent phase interacts with a liquid solvent phase to

selectively bind and remove these metal ions. In this process, the pollutants are present as dissolved solute adsorbate molecules and play a role in the separation that takes place at the boundary between the solid-liquid phases. The adsorptive separation process on the surface and inner pore structure of the nanoadsorbents is driven by various mechanisms, including chemisorption, ion exchange, physisorption, and complexation formation at the interface between the adsorbate and adsorbent (Anfar et al., 2020; Zhou et al., 2022). These mechanisms are influenced by the presence of a concentration gradient for mass transfer and diffusional processes, as shown in Figure 2.3.

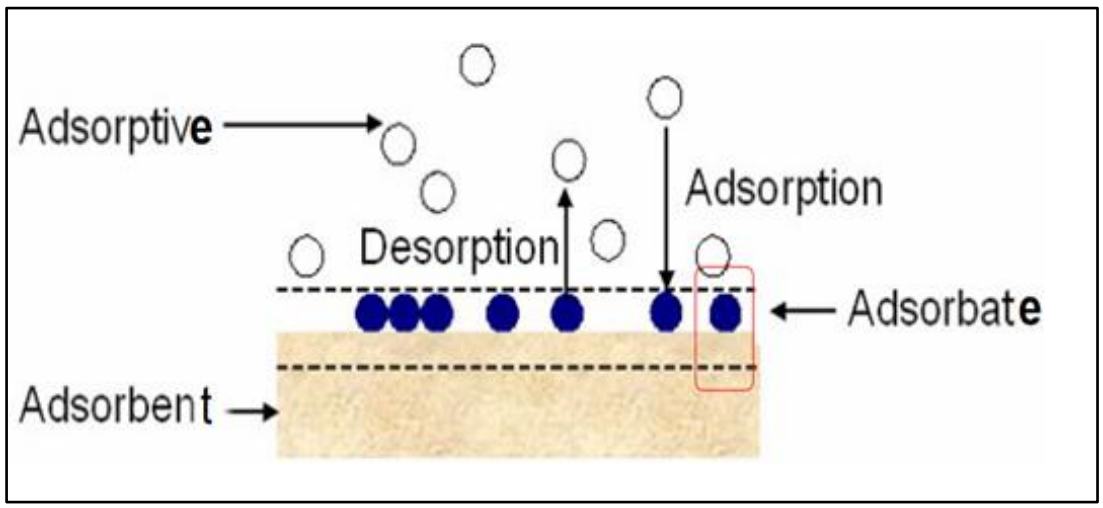

Figure 2.3: Schematic representation of the adsorption process (Lyubchik et al., n.d.).

Various adsorbent materials have been employed for the purpose of water and wastewater treatment. These materials can be classified as either natural adsorbents, derived from the Earth's crust and biological sources, or synthetic (non-natural adsorbents) adsorbents, which are generated in the laboratory or purchased from commercial organizations (Madima et al., 2020). Among the commonly used adsorbents, carbon-based nanomaterials are widely used as adsorbents in water and wastewater remediation. The materials in question have garnered considerable attention due to their distinctive characteristics, which comprise a small particulate size, high surface area, elevated porosity, remarkable thermal stability, and abundant active surface functional groups (Anfar et al., 2020; Baby et al., 2019; Yang et al., 2019). The significance of these properties plays a crucial role in the surface chemistry of carbon materials and the adsorption of heavy metals. Furthermore, the efficacy of adsorption as a water purifying/separation technique is contingent upon various factors including the

specific environmental conditions during operation, the choice of adsorbent material, the mechanism of adsorption employed by the adsorbent, the water solution conditions such as pH, temperature, adsorbate concentration, and the presence of other adsorbates in the liquid, the ability to regenerate or reuse the adsorbent, and the appropriate disposal method (Abiodun et al., 2023; Baby et al., 2019).

2.2.1 Carbon-based nanomaterials for adsorption

Carbon nanomaterials encompass a wide range of carbon allotropes, including zero-dimensional (0D) fullerenes and quantum dots clusters and particles, 1-dimensional (1D) nanotubes and nanowires, 2D nanosheets nanoplates and layers, and three-dimensional (3D) bundles of nanowires and nanotubes (Asha & Narain, 2020). The exceptional physicochemical features of carbon-based nanomaterials (CBNMs), such as carbon nanotubes (CNTs), activated carbon, biochar and graphene and its derivatives have garnered significant attention in the domain of pollution remediation (Figure 2.4). This is due to their huge specific surface areas, superior acid stability, and thermal resistance. These carbon materials have been shown to be excellent adsorbents for eliminating various environmental contaminants, including dyes, hydrogen sulfide, nitric oxide, heavy metals, and pharmacological compounds (Anfar et al., 2020; Yang et al., 2019). However, dispersing them in a water-based environment and retrieving them after being adsorbed can be challenging due to their hydrophobic nature and small dimensions. In addition, specific carbon nanomaterials, such as graphene and CNTs, exhibit a propensity to aggregate, leading to a reduction of both their surface area and surface chemistry. Consequently, this results in a substantial reduction in their ability to adsorb substances. To mitigate these drawbacks, significant effort has been devoted to enhancing the properties of carbon nanostructures. As a result of the thorough functionalisation of carbon nanomaterials, a wide range of modified carbon nanoadsorbents have been developed.

For example, they have undergone chemical modification and can be endowed with diverse organic functionalities, including oxygen-, nitrogen-, and sulfur-containing functional moieties such as hydroxyl (–OH), carboxyl (–COOH), amino ($–NH_2$), $–3SO_3H$, $–CONH_2$, and carbonyl (–C=O) groups (Baby et al., 2019; Khan and Alamry, 2022). On the other hand, these CBNMs can also be modified by incorporating metal or oxide nanoparticles (NPs)

(such as Fe_3O_4, Al_2O_3, TiO_2 and Ag) to produce carbon-based nanomaterials specifically designed for water treatment applications (Baby et al., 2019; Yang et al., 2019). Researchers have discovered that by integrating metal or metal oxide NPs into carbon-based nanomaterials and altering their structure using functional groups, it is possible to enhance their properties and adsorption performance to remove impurities during water purification (Yang et al., 2019).

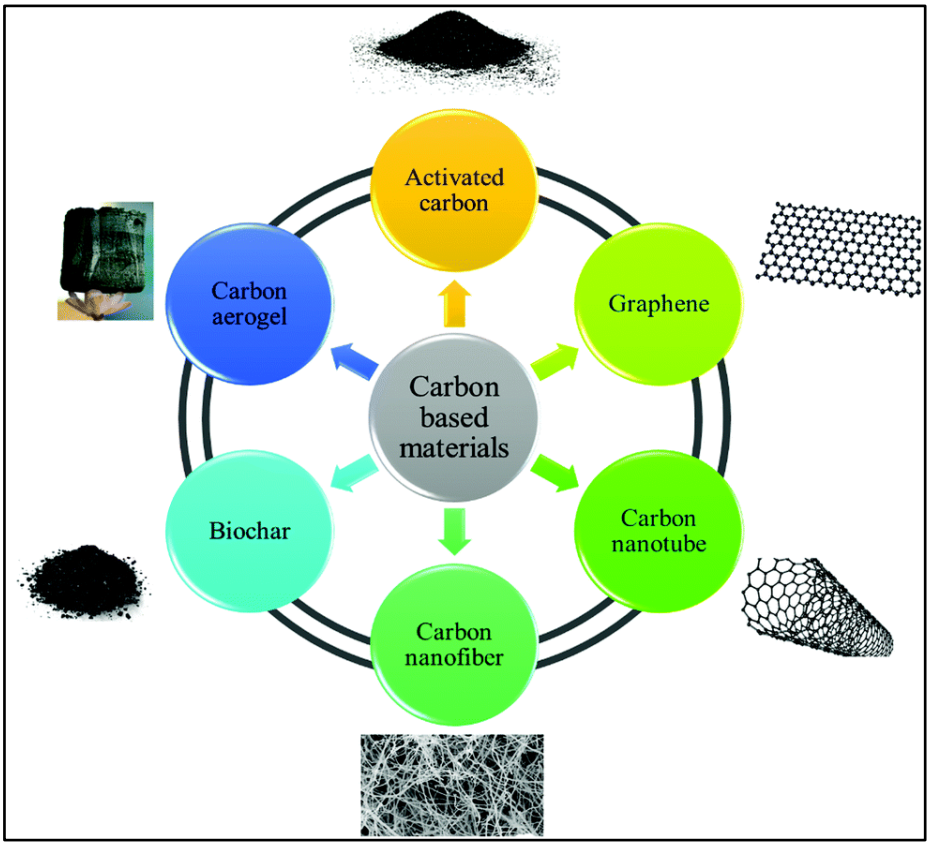

Figure 2.4: Various applicable carbon-based nanomaterials in adsorption processes (Sabzehmeidani et al., 2021).

2.2.1.1 Carbon nanotube adsorbents

Carbon nanotubes (CNTs), an emerging variant of carbon, were initially discovered in 1991 by Sumio Iijima at the NEC Laboratory in Tsukuba. These nanotubes exhibit remarkable physical, chemical, thermal stability, excellent thermal conductivity, and mechanical characteristics, which render them exceptionally auspicious for a vast array of applications

in fields such as nanoelectronics, microelectronic devices, medicine, catalyst support, and field emission (Ali et al., 2014; Rao et al., 2007). CNTs are predominantly comprised of cylindrical graphite sheets, which are arranged in interconnected aromatic rings on a cylindrical surface and can be classified into two main categories based on their shell structures: single-wall carbon nanotubes (SWCNTs) and multi-wall carbon nanotubes (MWCNTs) (refer to Figure 2.5). CNTs have exhibited superior adsorption capabilities compared to conventional adsorbents, owing to their porous and tubular structure, expansive surface area, chemical stability, and strong interaction with pollutant molecules (Oliveira et al., 2021; Tofighy and Mohammadi, 2011). The poor solubility of homogenous bundles of CNTs are often results in the manifestation of strong van der Waals forces. Hence, the functionalisation of CNTs holds significant importance due to its capacity to enhance their solubility and processing capabilities (Ahmadzadeh Tofighy and Mohammadi, 2012; Rao et al., 2007).

Various modification approaches, such as physical and chemical alterations involving different chemical functionalisation and incorporation of metal oxide NPs, have been utilised to produce nanomaterials with improved physiochemical properties (Rao et al., 2007). This is done with the aim of enhancing their solubility and their effectiveness in adsorption applications. The adsorption removal and affinity for carbon nanotube-based nanoadsorbents exhibit variations across distinct adsorbent and metal species. As demonstrated by (Stafiej and Pyrzynska, 2007), the authors ranked a selection of metal ions in terms of their affinity for oxidized CNT sheets at pH = 9. The order of affinity, from lowest to highest, was found to be as follows: $Mn^{2+} < Zn^{2+} < Co^{2+} < Pb^{2+} < Cu^{2+}$. Two further investigations conducted by (Rao et al., 2007; Tofighy and Mohammadi, 2011) have also validated the affinity ordering as follows: $Cu^{2+} < Zn^{2+} < Co^{2+} < Cd^{2+} < Pb^{2+}$ and $Pb^{2+} > Ni^{2+} > Zn^{2+} > Cu^{2+} > Cd^{2+}$, respectively, oxidized CNT sheets oxidized with different methods. Therefore, it can be argued that the adsorption efficiency of CNTs is greatly affected by their inherent properties. Furthermore, the alteration of CNTs through the incorporation of polymers and nanoparticles has garnered considerable attention owing to their unique characteristics and wide-ranging uses (Ali et al., 2014). Thus, functionalised, or modified CNTs have shown superior efficacy in removing heavy metals as compared to non-modified CNTs.

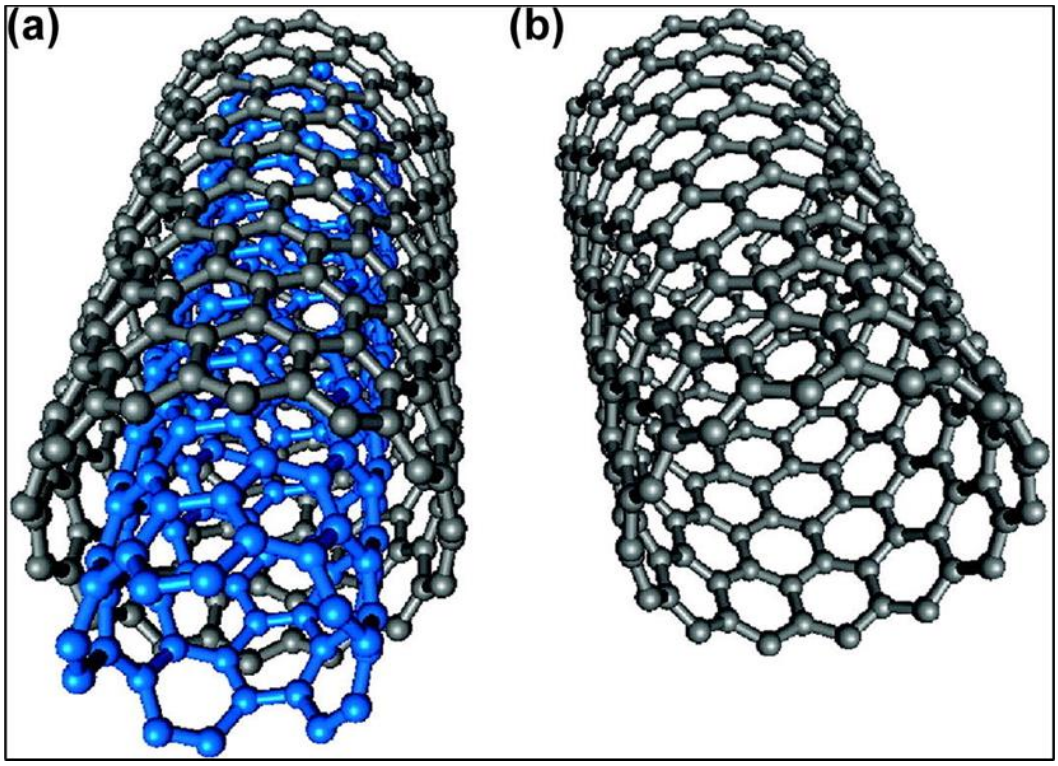

Figure 2.5: Schematic illustrations of (a) MWCNT and (b) SWCNT (Ali et al., 2014).

2.2.1.2 Graphene and their derivative nanomaterials

GN and its derivatives exhibit nearly identical structures, giving rise to the formation of two-dimensional carbon materials. However, slight differences between them result in unique physicochemical properties (Kumar et al., 2022; Xu et al., 2022). GN may be divided into two primary derivatives: GO and rGO. GO can be produced through the oxidation of graphite, while rGO can be made by reducing GO. GO possesses a diverse array of functional groups, such as epoxy carboxyl, and hydroxyl groups. These functionalities enable GO to bind with various types of molecules, particularly biomolecules, polymers and nanoparticles, facilitating its utilisation in a broad spectrum of applications (Kumar et al., 2022; Sabzehmeidani et al., 2021; Xu et al., 2022). The rGO exhibits oxygenated functional groups and surface defects, resulting in a structure that closely resembles pure GN. The level of oxygen-containing groups and surface defects can be controlled by modifying the intensity of the reduction reaction [24]. The predominant technique for transforming GO into GN entails the reduction of GO by thermal, chemical, and electrochemical processes. This procedure generates rGO, which exhibits a considerably lower amount of oxygen functional

groups in comparison to GO (Figure 2.6). Moreover, different reducing agents will yield distinct carbon-to-oxygen ratios and chemical contents in rGO. Due to these characteristics, such as great ability to be dispersed in water, amphiphilicity, and aptitude for surface functionalization, GO and rGO nanosheets are highly promising for membrane technology in water purification, desalination applications, and water purification through adsorption (Xu et al., 2022).

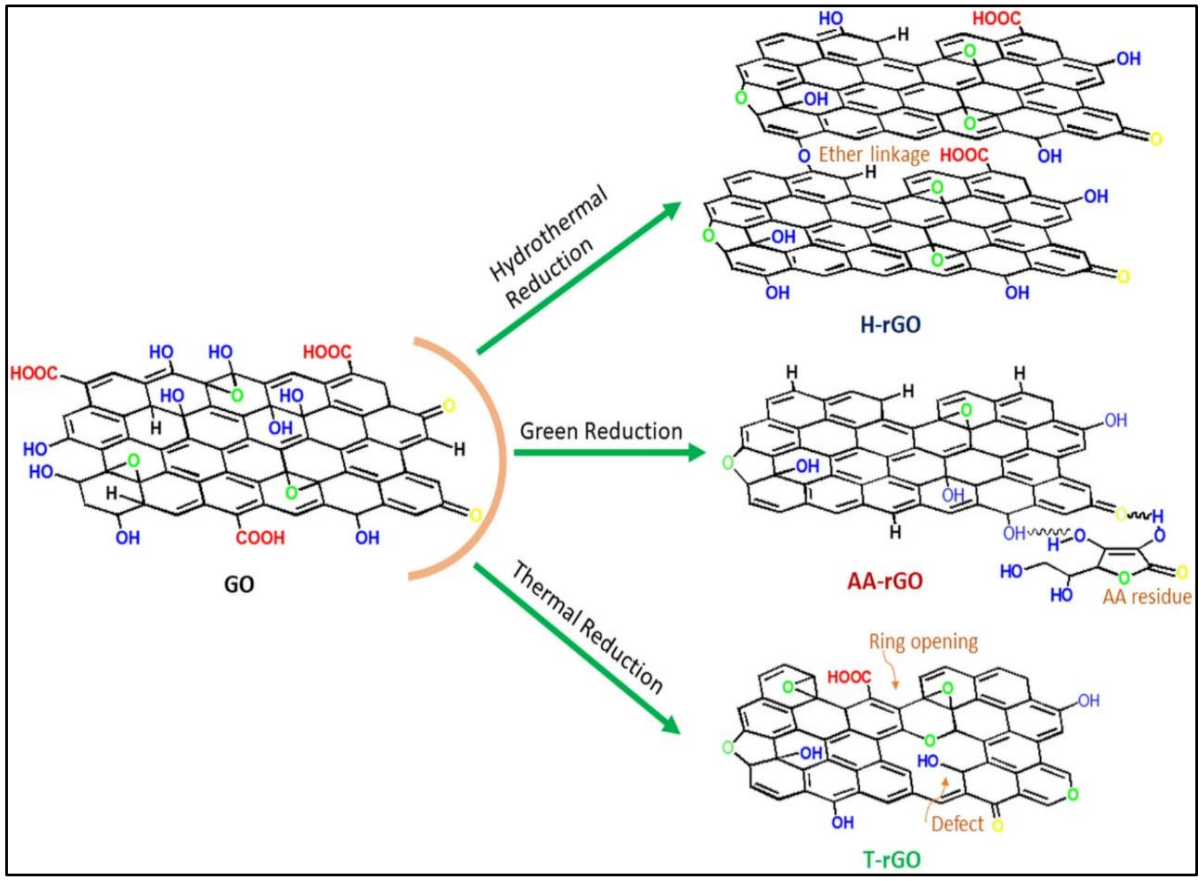

Figure 2.6: Diagram depicts the process of reducing GO nanosheets to rGO by thermal, green, and hydrothermal reduction techniques (Kumar et al., 2022).

Furthermore, GN and its derivatives ca be modified using doping with heteroatoms such as nitrogen (N), phosphorus (P), and sulphur (S) (Alsaiari et al., 2022; Yokwana et al., 2018). Heteroatom doping of graphene-based nanomaterials not only modifies their surface structure, but also impacts the surface chemistry and surface area of the carbon network, leading to enhanced adsorption performance. For example, Kota et al. (2016) and Lu et al. (2013) reported on nitrogen doping into the GN lattice and its adsorption performance of

various heavy metal, organic, and emerging water pollutants. Currently, researchers are widely using GO nanosheets as a starting material instead of pristine GN for the production of doped-GN-based nanomatrials to enhance their physicochemical properties, potentially boosting their efficacy in water purification processes (Liang et al., 2018). Additionally, the enhanced surface heterogeneity of GO can be attributed to the combination of its hydrophilic oxygenated surface, high surface area, easy incoporation of heteroatoms into its lattice, and the introduction of defects (Huo et al., 2019; Lu et al., 2013). This enables doped-GO to effectively adsorb various pollutants through hydrophobic interactions, Van der Waals forces, hydrogen bonding, electrostatic interactions, and π-π stacking (Alsaiari et al., 2022).

2.2.2 Graphene oxide-based nanomaterials for heavy metal removal

Nanotechnology has led to extensive research into GN-based materials, such as GO and reduced GO, due to its promise for removing heavy metals. The presence of different surface functionalities on GN-based nanomaterials significantly influences the adsorption of heavy metals. Hence, various methods are employed to alter GO, such as nitrogen doping, sulfuration, oxidation, and nitrogenation, with the intention of enhancing its specific surface area, pore structure, and surface chemistry. Thus, an enhanced abundance of metal ions can be adsorbed. For instance, Setshedi et al. (2015) investigated the adsorption process of Cr(VI) ions on polypyrrole-graphene oxide (PPy-GO). The results demonstrated that PPy-GO had a remarkable adsorption capacity of 625 mg/g and achieved complete removal of the material at a pH of 2, due to the presence of surface functional groups specifically O-H and C=O (Setshedi et al., 2015). Wang et al. (2015), on the other hand, found that the C=O and O–C=O oxygen-containing groups in Ppy-Fe_3O_4/rGO were what facilitated the attraction of heavy metals to the nanomaterial surface via electrostatic forces. At a pH of 2, the adsorption capacity of Ppy-Fe_3O_4/rGO for Cr(VI) was 293.3 mg/g with an efficiency of 98%. In another study, when chitosan-Fe_3O_4/GO (Chi@Fe_3O_4-GO) nanocomposite was used towards Cr(VI) removal, it achieved a maximum adsorption capacity of around 100.51 mg/g and complete removal of 100%. This effectiveness was credited to the existence of hydroxyl and carboxyl groups (Subedi et al., 2019). Hosseini et al. (2018) used $MgFe_2O_4$ nanoparticles to modify GO to produce magnetic nanocomposites of $MgFe_2O_4$–GO. These nanocomposites showed a remarkable ability to remove Cr(VI), achieving an efficiency of

up to 97% at pH 2. Furthermore, they exhibited exceptional reusability when recycled using a super magnet (Hosseini et al., 2018). Table 2.1. provides a succinct summary of studies conducted by various researchers using GO-based materials for the removal of chromium species.

Table 2.1: Summary of some of the GO-based materials used for the removal of Cr^{6+}

Nanoadsorbents	Initial concentration	Performance	References
ZnO-GO	5 mg/L	96% for Cr(VI) at pH 8	(Singh et al., 2022)
PEI–KOH/rGO	100 mg/L	398.9 mg/g and 100% for Cr(VI) removal at pH 2	(Tadjenant et al., 2020)
PPy–GO	100 mg/L	625 mg/g and 100% at pH 2	(Setshedi et al., 2015)
Ppy–Fe_3O_4/rGO	250 mg/L	293.3 mg/g at pH2	(Wang et al., 2015)
MoS_2/Rgo	-	80.8 mg/g and 75.9% at pH 2	(Zhou et al., 2020)
CaO-GO	10 mg/L	38.04 mg/g and 80.86% at pH 3.3	(Singh et al., 2022)
Fe_3O_4/RGO	-	99.9% at pH 1	(Zhang et al., 2021)
Chi@Fe_3O_4–GO	40 mg/L	100.51 mg/g at pH 2	(Subedi et al., 2019)

$MgFe_2O_4$–GO	40 mg/L	97% at pH 2	(Hosseini et al., 2018)

2.2.3 Biomass-based as adsorbents

Several researchers have employed diverse inexpensive adsorbents, such as biomass materials, to eliminate heavy metals from solutions. Biomass-derived adsorbents offer a sustainable and environmentally conscientious approach to tackling water pollution problems (Chugh et al., 2022; Daneshvar et al., 2019). Biomass materials, such as food waste, industrial, agricultural waste, and microalgae, are employed in the production of adsorbent materials that exhibit high efficacy in the removal of harmful heavy metals, including lead, mercury, and cadmium. The aforementioned approach demonstrates cost-effectiveness, renewability, and sustainability in contrast to conventional chemical methodologies. Agricultural residues possess a porous and unbound structure that encompasses hydroxyl and carboxyl groups, which play a significant role in adsorption mechanisms. Due to their minimal need for significant and expensive processing, biomass materials present a feasible substitute for conventional adsorbents, which are classified as non-renewable adsorbents. Adsorbents derived from biomass such as food waste, industrial, and agricultural waste, and microalgae, fungi, bacteria, cellulose, chitosan etc. have demonstrated considerable efficacy and exhibit tremendous potential in the realm of pollutant removal from wastewater, particularly with regard to heavy metals, dyes, and various other contaminants (Ova and Övez, 2013; Husien et al., 2019).

2.2.3.1 Microalgae

Microalgae are eukaryotic organisms that possess chlorophyll and perform oxygenic photosynthesis. These microorganisms are considered to be renewable natural biomasses that proliferate ubiquitously and abundantly. Microalgae biomasses are highly promising organisms for use as novel adsorbents of metal ions, especially in bioremediation processes (Almutairi et al., 2021; Ata et al., 2012). Microalgae biomasses have gained interest because they are abundant, have a large surface area, can absorb significant amounts of metals, are

easy to retrieve and reuse, and have the potential to achieve high efficiencies in a short amount of time. Typically, both living and non-living microalgal cells can be utilised to efficiently eliminate harmful heavy metals from effluent or wastewater. The following microalgae species have been employed as biosorbents in the removal of chromium species in water and wastewater and are represented in Table 2.2. Some of these species are *Scenedesmus, Chlorella, Sargassum sp, Gracilaria verrucosa, Chlamydomonas, Nitzschia closterium, etc* (Gunasundari and Kumar, 2017; Sibi, 2016). The interaction between biomass and Cr species is influenced by affinity, which causes the metal ions to be captured and attached to the biomass. Various algae biosorbents exhibit varying adsorption capabilities. Due to the different functionalities present within the biosorbent's structure, which enable it to bind with metals in aqueous media.

For example, in a study conducted by Pena-Castro et al. (2004), the effect of the adsorption capability of the algal strain *Scenedesmus incrassatulus on* cadmium (II), chromium (VI), and copper (II) was investigated. They found that *Scenedesmus incrassatulus* algal species have a high removal and binding capability of 25-78% for these heavy metals (Peña-Castro et al., 2004). They also demonstrated that in comparison to other metal ions, *S. incrassatulus* algae have a far stronger affinity for chromium. The complete elimination of Cr ions from water was achieved by microalgal biochar, as reported by the study conducted by Daneshvar et al. (2019). Yen et al. (2017), Sibi (2016), and Al-Homaidan et al. (2018) investigated the removal of Cr(VI) from wastewater by using both living and dead species of *Chlorella vulgaris and Cladophora glomerata alga*. They found that microalgae have a high Cr adsorption effectiveness of 43–85% (Al-Homaidan et al., 2018; Sibi, 2016; Yen et al., 2017). Additionally, Shokri et al. (2015) investigated the binding ability of biosorbents generated from microalgae biomass, which contained lipids (9.2%), protein (43.5%), and carbohydrates (20.2%). Afterwards, the adsorption of Cr(III) and Cr(VI) metal ions was performed. The maximum removal of Cr(III) was found to be 98.3% at pH 6.0, while at pH 1, the maximum adsorption for Cr(VI) was 47.6% (Shokri et al., 2015). In a different study by Pradhan et al. (2019) biomass from Scenedesmus sp. algae was used to remove Cr(VI) ions from aqueous solutions. Scenedesmus sp. was able to remove 92.9% of Cr(VI) (Pradhan et al., 2019).

Table 2.2: Summary of work done by various researchers using microalgae as biosorbents for the removal of chromium species.

Microalgae biosorbent	Experimental condition	Removal efficiency (%) and Q_{max} (mg/g)	References
Sargassum dentifolium	CT: 12h, pH: 7, T: 50 °C; 100 mg/L	Cr(VI): 99.68% and 53.28 mg/g	(Husien et al., 2019)
Gracilaria verrucosa (red algae)	CT: 24h, pH: 5, T: 25 °C; 100 mg/L	Cr(VI): 77% and 113.2 mg/g	(Ata et al., 2012)
Chlamydomonas Reinhardtii	CT: 120 min, pH: 2, T: 25 °C; 100 mg/L	Cr(VI): 95% and 11.2 mg/g	(Arica et al., 2005)
Spirulina platensis	CT: 30 min, pH: 3,; 50 mg/L	Cr(VI): 99.9% and 577.9 mg/g	(Gunasundari and Kumar, 2017)
Immobilized Chlorella sorokiniana	CT: 90 min, pH: 2–4, T: 25 °C	Cr(III): 69·26 mg g^{-1}	Akhtar *et al*. (2003)
Scenedesmus quadricauda-based biochar	CT: 4 h, pH: 2, T: 35 °C, 10 mg/L	Cr(VI): 100%	(Daneshvar et al., 2019)
Chlorella vulgaris	CT: 4h, pH: 2; 50 mg/L	Cr(VI): 81.6% and 98 mg g^{-1}	(Sibi, 2016)
Scenedesmus quadricauda	CT: 120 min, pH: 6 and 1; 100 mg/L	Cr(III): 98·3%, 58.47 mg g^{-1} and Cr(VI): 47·6%, 46.51 mg g^{-1}	(Shokri Khoubestani et al., 2015)

Scenedesmus sp.	CT: 120 min, pH: 1; T:30 °C; 100 mg/L	Cr(VI): 92.89% and 0.301 mg g^{-1}	(Pradhan et al., 2019)
Spirulina platensis	10 mg/L, 30 °C, pH: 1.5	Cr(VI): 99% and 0.301 mg g^{-1}	(Gokhale et al., 2009)
Chlorella sorokiniana	pH: 4.0; T 25 °C; 25 mg/L;	Cr(III): 98% and 69.26 mg g^{-1}	(Nasreen et al., 2008)

2.2.4 Adsorption mechanisms

Figure 2.5. illustrates the mechanisms that govern the removal of heavy metals using carbon-based adsorbent materials such as activated carbon, biochar, CNTs, fullerene, and GN and its derivatives. The interactions between the functionalities of carbon-based materials and pollutants are usually complex. The efficacy of adsorption depends on the physicochemical properties of the carbon-based materials, the parameters of the water-based solution, and the nature of the substance being adsorbed (Yang et al., 2019). Furthermore, the adsorption mechanisms on carbon adsorbents might entail physisorption, which comprises physical adsorption and electrostatic interaction, as well as chemisorption, which involves surface ion exchange, complexation, and precipitation (Anfar et al., 2020; Yang et al., 2019). Electrostatic attraction refers to the interaction between the positively charged on heavy metals and negatively charged surfaces on carbon-based adsorbents or vice versa. This interaction is influenced by the presence of functional groups (such as -OH, $-NH_2$, $-SO_3H$, and -COOH) on their surface, which can become ionized and create a charged interface (Akhter et al., 2023; Yang et al., 2019). The ion exchange process typically occurs between divalent metals and protons, which are found in oxygen-containing functional groups such as carboxyl and hydroxyl groups. This process is influenced by factors such as the pH of the solution, the size of the metal contaminant ions, and the chemical composition of the surface functional groups of the adsorbent (Akhter et al., 2023). Whereas, the process of physical adsorption relies on various factors, such as the distribution of pore sizes, the surface area of the adsorbents, and the characteristics of the heavy metal involved. Furthermore, heavy metals diffuse into the carbon adsorbent's pores, followed by their deposition onto the pores

without the formation of chemical bonds (Akhter et al., 2023; Raji et al., 2023). In the case of surface complexation process, multiatom structures are generated, leading to distinct binding interactions between metal ions and functional groups. On the other hand, during precipitation, the heavy metals dissociate from water in the form of solid precipitates by reacting with ions or groups present on the adsorbent surface (Yang et al., 2019). Chemisorption typically has a greater influence than physisorption in removing pollutants from aqueous solutions (Rao et al., 2007; Yang et al., 2019).

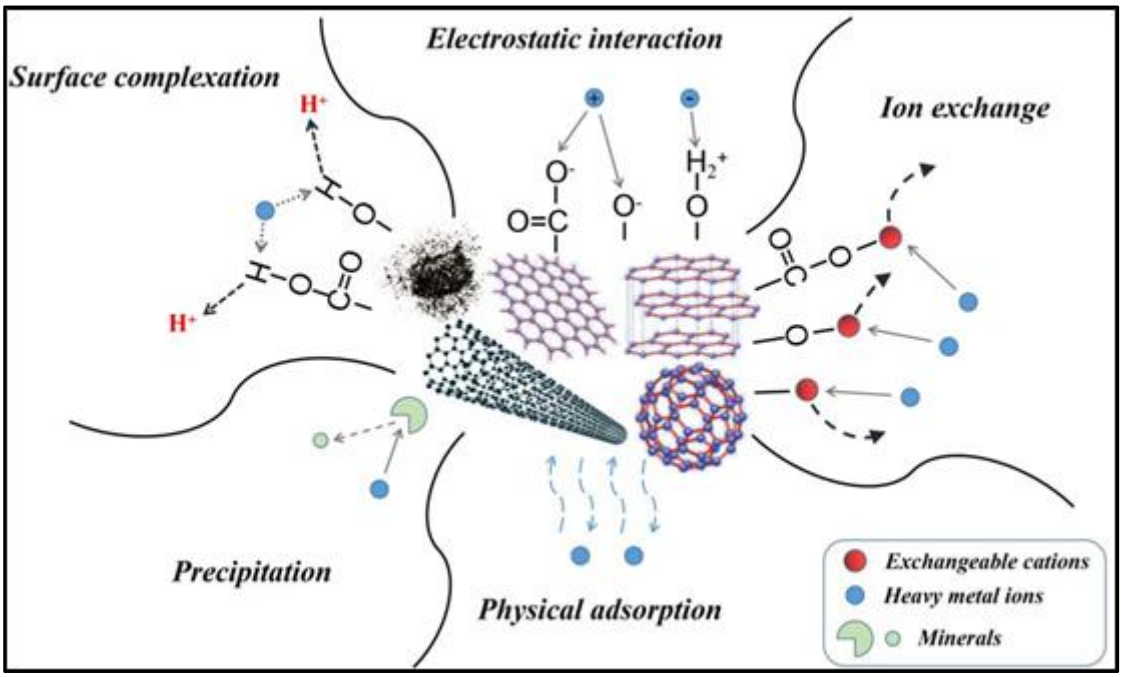

Figure 2.7: Schematics of adsorption mechanisms of heavy metals onto carbon-based nanoadsorbents (Yang et al., 2019).

The microalgae species have the ability to concentrate metal species from diluted aqueous solutions and store them internally or on the surface of their cell structures. The intricate nature of the microorganism's cellular architecture suggests that there are numerous mechanisms by which the metal can be sequestered by the cell. These mechanisms can be categorized based on two characteristics. The initial criterion is based on cell metabolism, which can be categorized as either (1) metabolism-dependent or (2) metabolism-independent (Chugh et al., 2022; Suresh Kumar et al., 2015). Another criterion categorizes the methods of biosorption based on the specific site within the cell where the metal is stored after adsorption. This location can be either outside the cell, on the cell surface, or inside the cell

(Pradhan et al., 2022; Zhou et al., 2022). Figure 2.6. provides a concise overview of the interconnections between various biosorption pathways.

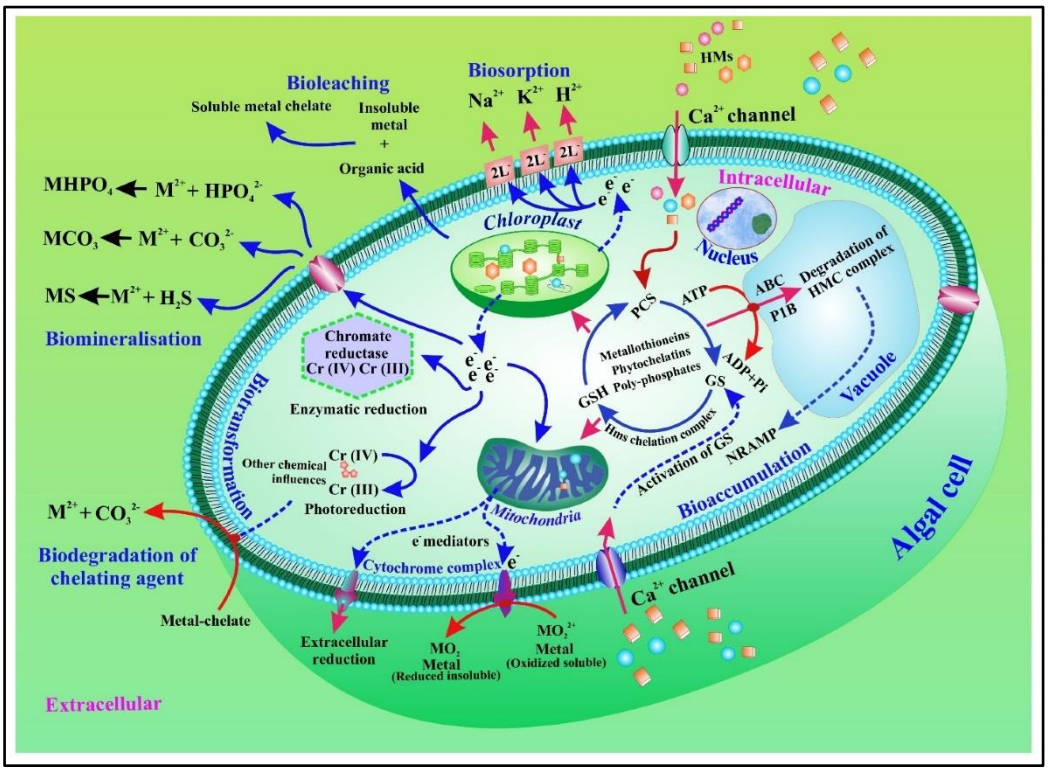

Figure 2.8: Schematics of heavy metals mechanism based on microalgae-based systems (Pradhan et al., 2022).

CHAPTER 3

MATERIALS AND EXPERIMENTAL PROCEDURES

3.1 Experimental

3.1.1 Materials

The microalgae (*Scenedesmus*) biomass used in this study was supplied by InnoVenton: Institute for Chemical Technology which is a Research Institute at the Nelson Mandela University. All chemicals used in this study are provided in Table 3.1.

Table 3.1: List of the chemicals used in this research.

No	Material	Purity	Supplier
1	Graphite powder	99%, < 20 μm	Sigma Aldrich
2	Urea	99-100.5%	Sigma Aldrich
3	Potassium permanganate ($KMnO_4$)	≥ 99%	Sigma Aldrich
4	Sodium nitrate ($NaNO_3$)	99%	SAARCHEM
5	Sulphuric acid (H_2SO_4)	98%	ACE
6	Hydrogen peroxide solution (H_2O_2)	30% w/w	Sigma Aldrich
7	Hydrochloric acid (HCl)	30%	ACE
8	Ethanol	99.9%	Spellbound
9	Microalgae	-	-
10	Potassium dichromate	99.5%	SAARCHEM

3.1.2 Synthesis of graphene oxide

Graphene oxide (GO) was synthesized using a modified Hummers method (Kumar et al., 2022; Oliveira et al., 2018) (Figure 3.1). Graphite powder (2.5 g, 3.47 mol/L) and $NaNO_3$ (2.5 g, 0.490 mol/L) were dissolved in a concentrated H_2SO_4 (60.0 mL, 18.67 mol/L) and stirred for 4h in an ice bath. Subsequently, $KMnO_4$ (7.0 g, 0.740 mol/L) was incrementally introduced over 30 min intervals and thereafter stirred for an hour. The ice bath was removed, and the mixture was continuously agitated at 35 °C for 2 h. After continuous stirring, 50.0 mL of distilled water was introduced and agitated at 90 °C for 2 h. Thereafter, 100 mL of distilled water was added while stirring until the mixture reached ambient temperature, and then H_2O_2 (50 mL, 1.63 mol) was added to the suspension. The suspension was then first centrifugally washed with a 10% HCl solution and then distilled water several times at 2000 rpm for 10 min until the pH of the decanted water reached ~ 7.0. The obtained GO paste was dried in an oven at 60 °C for 72 h.

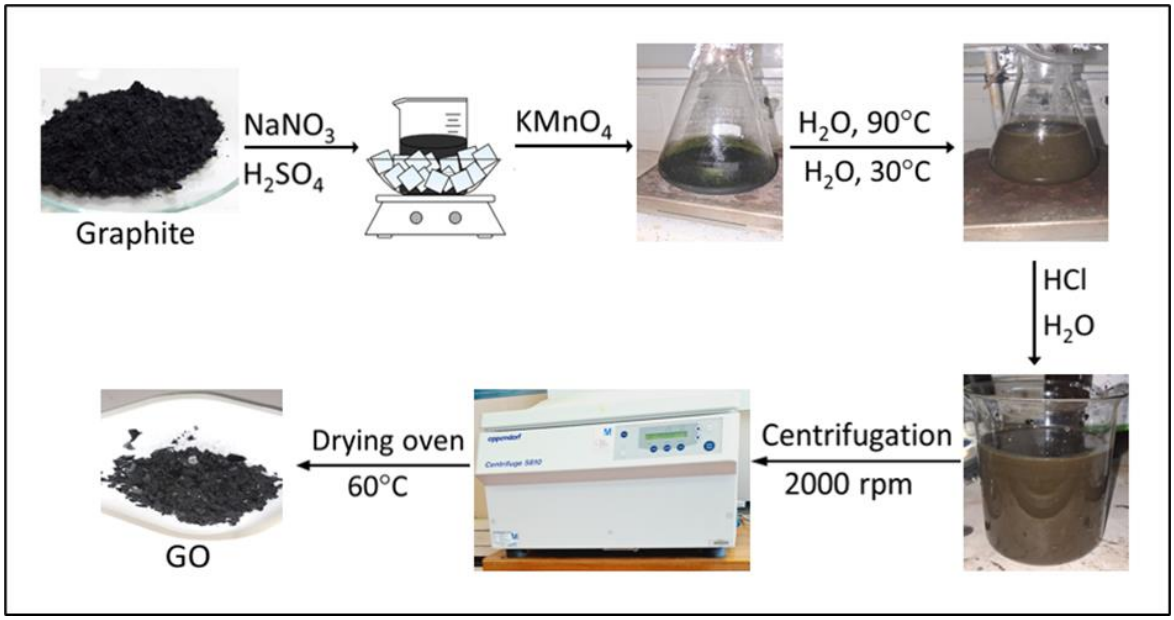

Figure 3.1: Schematic representation of the synthesis process for graphene oxide.

3.1.3 Synthesis of nitrogen-doped graphene oxide

Nitrogen-doped graphene oxide (NGO) was synthesized using the modified Hummer's method similar to GO (Section 3.1.2). The only exception, in this case, was that urea was used as a nitrogen precursor added during the reaction. Urea (2.5 g, 0.042 mol) was added after the removal of the ice bath, the reaction continued to stir overnight at 30 °C. Figure 3.2. shows in situ/one-pot synthesis of NGO nanosheets.

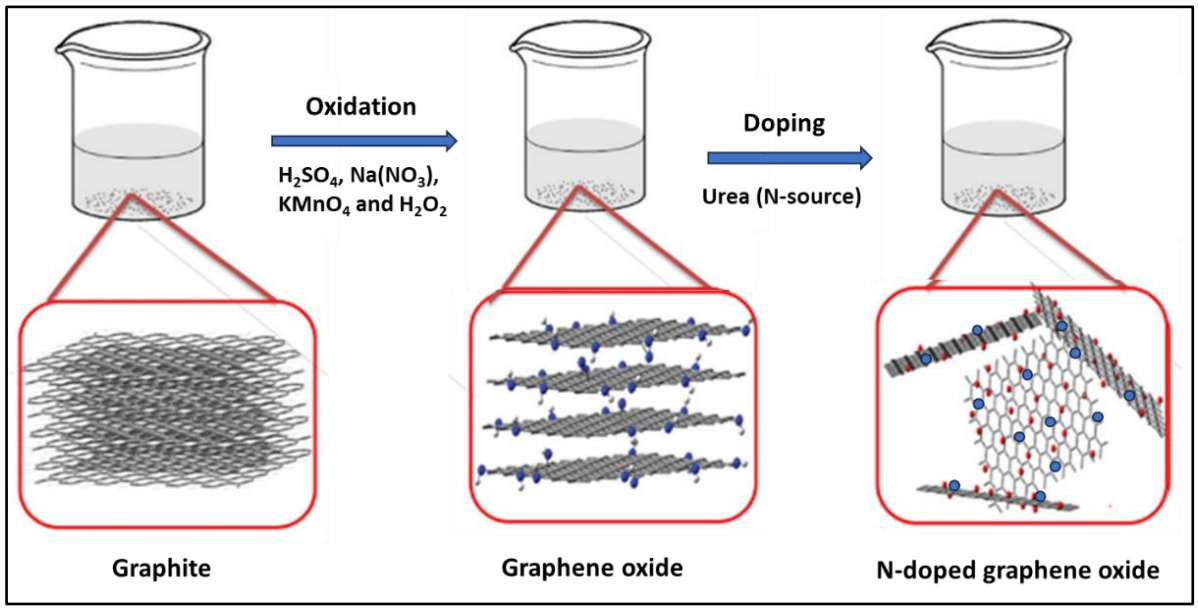

Figure 3.2: Schematic of the NGO synthesis process. Blue and red colour dots represent the oxygen- and nitrogen-containing functional groups.

3.1.4 Synthesis of graphene@biomass nanohybrid materials

A self-assembly method (without external stimuli) incorporated *Scenedesmus* microalgae with GO and NGO (see Figure 3.3). Firstly, a specific amount of GO materials was dispersed in distilled water for 2 h through sonication, and then various amounts of microalgal supernatant were added into the solution according to the ratio GN-based (GO and NGO): algae (wt./wt.) and continuously sonicated for about 8 h. Thereafter, the mixture was centrifuged at 2000 rpm for 15 min. The obtained product was dried in the oven at 65 °C. The mix proportions of the GO@microalae (GO@Algae (1:1), GO@Algae (3:1), and

GO@Algae) (1:3)) and NGO@microalgae (NGO@Algae (1:1), NGO@Algae (3:1) and NGO@Algae (1:3)) composites, respectively and their description are given in Table 3.2.

Table 3.2: Mix composition of the GO@algae and NGO@algae nanohybrids.

Samples ID	Graphene-based/mg	Algae/mg	Ratio
GO	-	-	-
GO@Algae-1:1	400	400	1:1
GO@Algae-3:1	600	200	3:1
GO@Algae-1:3	200	600	1:3
NGO	-	-	-
NGO@Algae-1:1	400	400	1:1
NGO@Algae-3:1	600	200	3:1
NGO@Algae-1:3	200	600	1:3

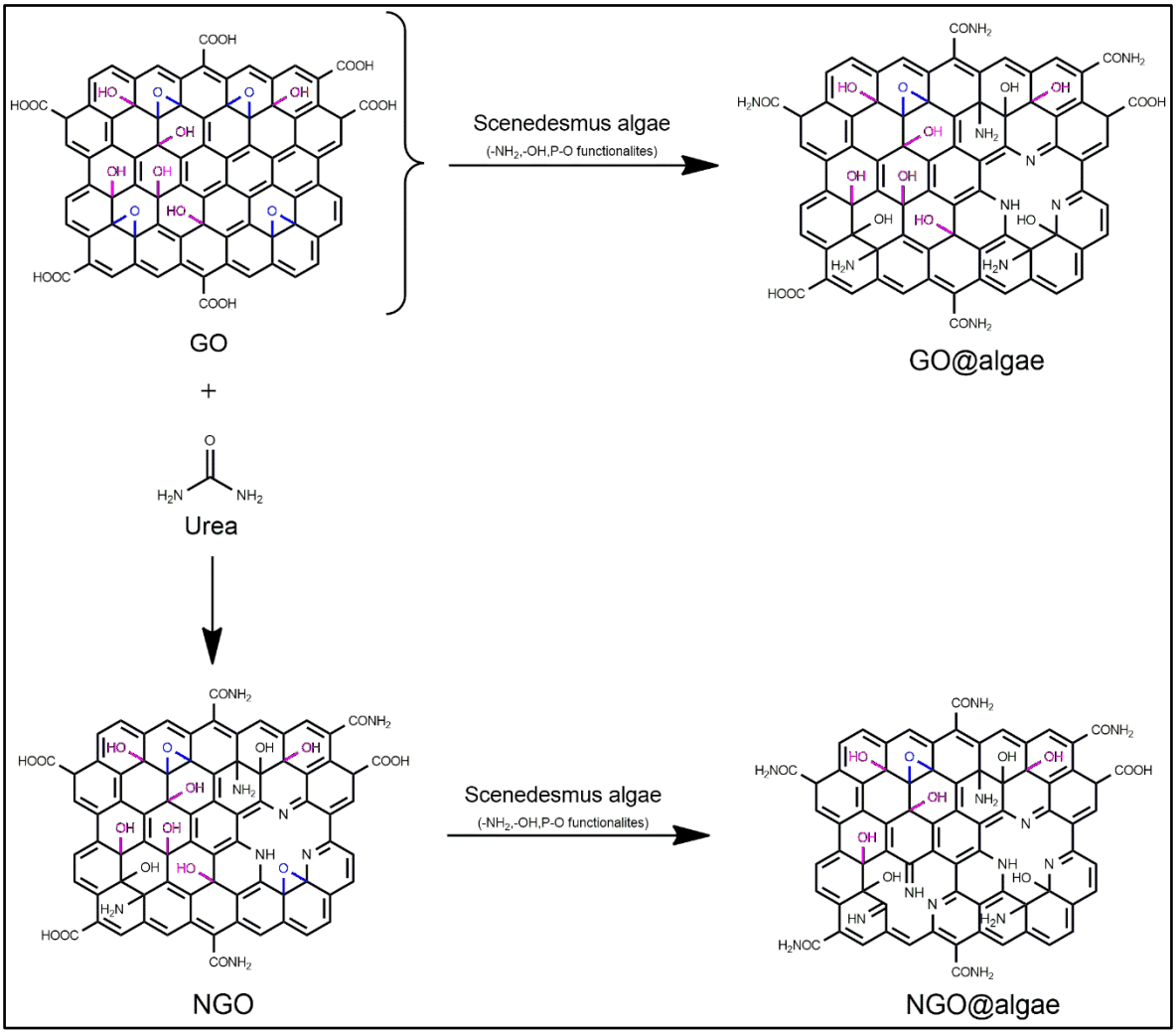

Figure 3.3: Schematic presentation of GO@algae and NGO@algae nanohybrids preparations.

3.2 Characterisation of graphene@biomass-based nanohybrid materials

Several techniques that were used to characterize the GN-based@biomass nanocomposite are; Brunauer-Emmett-Teller (BET), Zeta potential, Fourier Transform Infrared Spectroscopy (FT-IR), X-ray diffraction (XRD), Scanning Electron Microscopy (SEM), Ultraviolet-visible spectroscopy (UV-Vis), X-ray photoelectron spectroscopy (XPS) and Thermogravimetric/differential thermal (TGA).

3.2.1 Fourier-Transform Infrared Spectroscopy

FT-IR spectroscopy is an analytical technique used to detect changes in the overall composition of nanomaterials, composites, and microorganisms by analysing alterations in functional groups within their matrix. Additionally, it quantifies how infrared radiation at a particular wavelength affects the molecular vibrations and rotations of the samples. In this work, the FT-IR instrument shown in Figure 3.3, (Brunker platinum ATR Tensor 27 spectrometer, LabSpec software) with an accessory attached to a diamond crystal was used to determine chemical bonds and the functionalities present on the nanostructured materials. The FT-IR spectra were acquired using reflectance mode, with a resolution of 4 cm^{-1}, covering a spectral range of 500−4000 cm^{-1}. The spectrum that was generated and showed an absorption peak is a molecular signature of the material. The fine powder sample was placed on the diamond grid and pressed down for characterisation. Such a technique can provide a direct means of observing the interactions between the surface of GN-based nanohybrids and adsorbed species.

Figure 3.4: Brunker platinum ATR Tensor 27 IR spectrophotometer used in this work.

3.2.2 UV-vis spectroscopy

UV-vis analysis was performed to measure the absorption of the materials concerning the reference. The Thermofisher Scientific Evolution 200 series spectrophotometer software used was the spectrophotometer available at Nelson Mandela University, Chemistry Department. The photograph of the instrument is shown in Figure 3.5. The wavelength used was between 200 nm and 800 nm. To perform the analysis, the material was diluted with the reference (deionised water) and placed in a quartz cuvette. The concentration of Cr(VI) was also determined by UV-Vis spectroscopy employing the 1,5-diphenylcarbazide (DPC) method, as described by Gilcreas et al. and Mahajan and Sud 2012. After adsorption, the samples were acidified with phosphoric acid and dilute sulfuric acid prior to complexation. Then a solution of 1,5-diphenylcarbazide (1.2 mL) was into a 20 mL sample to complex Cr(VI) and after 15 min the resulting mixture was analysed by measuring its absorbance at a wavelength of 540 nm.

Figure 3.5: Thermofisher Scientific spectrophotometer (UV-Vis Evolution 200 series) used in this research.

3.2.3 X-ray diffraction

X-ray diffraction (XRD) is a flexible characterisation technique that yields information about the phases present in nanomaterials by analyzing their crystallographic structure and characteristics. The graphene@microalgea-based nanohybrids were analysed using a Malvern Panalytical Aeris Powder X-ray Diffractometer (Billerica, MA, USA), which was fitted with a Co source (λ = 1.789 Å) and operates at 40 keV. The data was evaluated with the comprehensive Rietveld refinement technique and the Bruker TOPAS v6 software. The XRD patterns of the nanohybrids were obtained using a continuous mode measurement covered a range of 5 to 70 degrees 2θ, at 0.02 steps, and a scan speed of 0.4 0.4 sec/step. The instrument is located at the North Campus at eNtsa, Nelson Mandela University.

3.2.4 Brunauer-Emmett-Teller surface area and porosity analyzer

The Brunauer-Emmett-Teller (BET) surface area and porosity analyser were used to determine the specific surface area, pore size, and total pore volume distributions of the prepared nanohybrids. The BET surface area was determined using a Micrometrics TriStar II 3020 BET v3.02 analyser (Figure 3.6). The adsorptive gas during the analysis was nitrogen. The analysis conditions were set out to the pre-set program "uYilo Std BET 5-point analysis". Before analysis, the nanohybrids were first degassed at 120 °C for 4 h and then N_2 adsorption-desorption isotherms were measured.

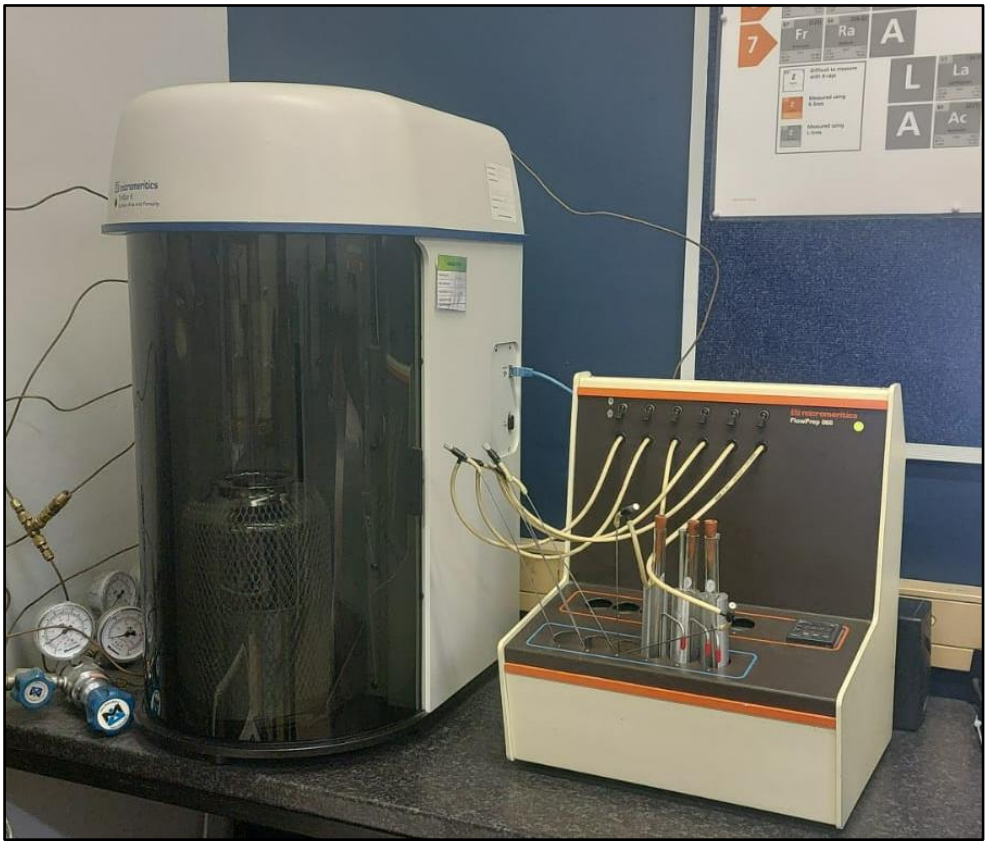

Figure 3.6: Brunauer-Emmett-Teller analyser used in this research.

3.2.5 Scanning electron microscopy

The scanning electron microscopy – energy dispersive spectroscopy (SEM-EDS) technique was employed to investigate the morphology of GO and NGO nanosheets and graphene@microalgae-based nanohybrids. The instrument used for this analysis was the JEOL JSM 5600 InTouchScope™.

3.2.6 Thermal analysis studies

Thermogravimetric/differential thermal analysis (TGA/DTA) was employed to assess the thermal stability of the nanomaterials (Figure 3.7). The experiments were carried out on an SDT-Q600 Simultaneous DSC-TGA (TA Instruments, USA) with a sample weight of ~ 0.003 g. The experiments were conducted in a nitrogen environment with a flow rate of 100 mL/min and a heating rate of 10 °C/min over a temperature range of 30 ^{o}C to 600 ^{o}C for the

decomposition process. The TGA program was utilized to record the weight and temperature data, which were then used to construct differential thermogravimetric (DTG) curves.

Figure 3.7: TA Instrument SDT-Q600 DSC-TGA.

3.2.7 Zeta potential

The surface charge of the fabricated nanocomposites was analysed with a Zetasizer Nano ZS nanometer (Malvern Panalytical, UK). The samples were initially dispersed into deionised water using sonication. Subsequently, pH was adjusted using 0.1 M solutions of NaOH and HCl. In order to determine the zeta potential of nanoadsorbents, a volume of 1 mL of the sample was transferred into a cuvette for analysis.

3.2.8 X-ray photoelectron spectroscopy

X-ray photoelectron spectroscopy (XPS) was utilized to quantify the surface chemical composition of microalgae, including the elemental ratio, macromolecule composition, and composition of functional groups. An XPS examination was conducted on the dry

graphene@microalgae nanohybrid material using an Al X-ray (1486 eV) source on a Physical Electronics (Quantum 2000) spectrometer.

3.3 Batch mode adsorption experiments

The optimization of parameters for the nanostructured graphene@microalgae-based materials was accomplished through laboratory batch tests. These tests included the investigation of the influence of solution pH, adsorbent dose, adsorption time, and initial Cr^{6+} concentration, see Table 3.3. All adsorption experiments were carried out in duplicate under ambient conditions at a temperature of approximately 30 °C. At first, a solution containing 1000 mg/L of Cr(VI) was prepared. This was achieved by dissolving 2.827 g of $K_2Cr_2O_7$ in a 1 L volumetric flask using deionized water. Subsequently, a sequence of functional standard solutions with varying concentrations was created by suitably diluting the original solution.

A series of batch experiments was conducted to optimize the pH of the solution. Each experiment utilized 10 mL of a solution containing an initial concentration of 10 mg L^{-1} of Cr(VI) with an adsorbent dose of 0.05 g at pH of 2 and 5 (the pH range was based on previous studies indicating that Cr(VI) is effectively adsorbed by GO-based nanomaterials at low pH levels) (De Beni et al., 2022). Studies were undertaken to determine the best initial chromium content by testing a range from 5 to 80 mg L^{-1}. The studies were carried out at a solution pH of 2 and utilizing a fixed amount of 0.05 g of the adsorbent. The determination of the equilibrium contact time was conducted within a contact time interval range of 10 to 360 minutes. For this purpose, 0.05 g of adsorbents were placed in 15 mL stoppered vials containing 10 mg L^{-1} initial concentration of Cr^{6+}, while the solution pH was maintained at 2.0. In addition to optimizing other significant batch characteristics, the quantity of the adsorbent was also optimized. The optimum dose was evaluated by varying the dosage of adsorbent within the range of 2.0–80 mg while maintaining a constant solution pH of 2.0 and an initial adsorbate concentration of 10 mg L^{-1}. The suspensions were agitated for a contact period of 360 minutes.

To achieve the intended result, the suspensions were transferred into stoppered vials and subjected to agitation at a speed of 250 revolutions per minute (rpm) using a mechanical

shaker. After the adsorption process, the samples were centrifuged and subsequently filtered using a 0.45 µm nylon syringe filter. The remaining Cr^{6+} concentrations in the filtrates were then measured using UV-Vis spectrophotometry, refer to Figure 3.8 for visual representation.

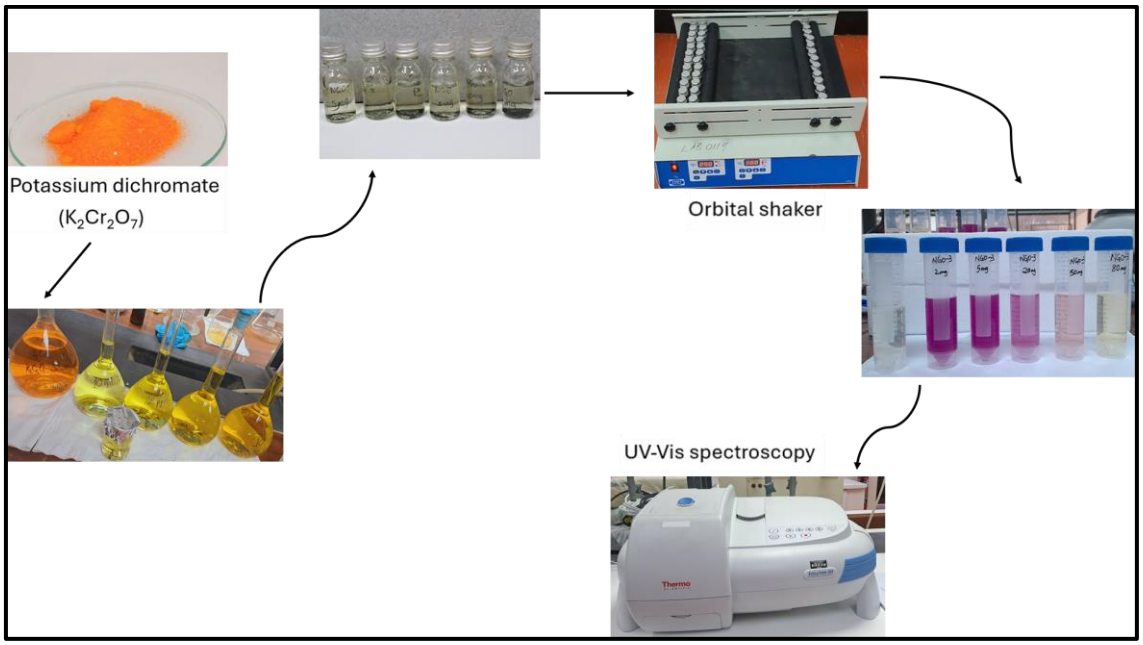

Figure 3.8: Schematic illustration of the batch adsorption studies.

The removal efficiency (%) and the amount of sorbed Cr species at equilibrium (q_e) were computed according to the formulas (3.1) and (3.2), respectively.

$$\text{Removal\%} = \frac{C_i - C_f}{C_i} x\, 100\% \qquad (3.1)$$

$$q_e = \frac{C_i - C_f}{C_i} x \frac{V}{m} \qquad (3.2)$$

where:

m is the weight of the dry nanoadsorbents used in (g), C_i and C_f are the concentrations of adsorbate prior to and after adsorption equilibrium (mg/L), respectively, and V represents the volume of the adsorbate species solution (L).

Table 3.3: The parameter values of batch mode adsorption process.

Dosage (mg)	**Time (min)**	**Initial concentration of Cr (mg/ L)**	**pH**
2.0, 5.0, 20.0, 50.0 and 80.0	10, 30, 60, 90, 180, and 360	5, 10, 20, 50, 80	2 and 5

3.3.1 Study on adsorption kinetics

In order to ascertain the rate of adsorption, an initial concentration of 10 mg/L was subjected to different contact durations ranging from 10 to 360 min. The remaining experimental parameters, including the adsorbent dose, adsorbate concentration and the pH of the solution used, were kept constant. To get a better understanding of the adsorption mechanism, which encompasses chemical reactions and mass transfer, several kinetic models were used. These included the pseudo-first-order (PFO), pseudo-second-order (PSO), and intra-particle diffusion (IPD) adsorption kinetic models.

The PFO model, also known as the Lagergren equation, describes that the adsorption mechanism occurs through physical interaction via diffusion through the interface. It is the first-rate equation specifically designed for sorption in liquid-solid systems (Sabzehmeidani et al., 2021). The linearized PFO equation is presented in Eq.3.3.

$$\log(q_e - q_t) = log q_e - {k_1 t}/{2.303} \qquad (3.\ 3)$$

where:

q_e is the amount of metal ions adsorbed at equilibrium (mg/g), while q_t (mg g^{-1}) is the uptake of Cr^{6+} metal ions by adsorbent at time *t*. k_1 (min^{-1}) represents the rate constant of PFO sorption.

The PSO kinetics is predicated on the premise that sorption adheres to a mechanism of the second order, with chemisorption serving as the step that restricts the rate. The rate at which adsorption sites are filled is directly related to the square of the number of sites that are not currently occupied (Pradhan et al., 2019).

Pseudo-second-order kinetic model:

$$t/q_t = k_2 q_e^2 + t/q_e \quad (3.4)$$

where:

k_2 (g/mg·min) represents the rate constant of PSO sorption.

Lastly, IPD which can be expressed by Eq. (3.5) (Nithya et al., 2019).

$$q_t = K_p t^{0.5} + C \quad (3.5)$$

where:

K_p represents the intra-particle diffusion rate constants (mg/g.min) for Weber and Morris, and C (mg g^{-1}) is the constant linked to the boundary layer and thickness around the adsorbent.

3.3.2 Study on adsorption isotherms

The purpose of using adsorption isotherms is to establish the precise correlation between the concentration of the adsorbate in the bulk phase at equilibrium and the amount of adsorbate that is attached to the surface. The equilibrium result for the adsorption of Cr(IV) onto graphene@microalgae-based nanohybrids was evaluated using the Langmuir and Freundlich isotherm models. The Langmuir isotherm is predicated on the notion that sorption occurs within a monolayer, namely at uniform and homogenous sites within the sorbent. Furthermore, in the presence of a solute, the occupation of a site prevents any additional

sorption from occurring at that particular site (Yokwana et al., 2018). This isotherm is expressed by Eq. (3.6):

$$q_e = K_L q_m {}^{C_e}/_{1} + K_L C_e \quad (3.6)$$

where:

q_m is the adsorption capacity or maximum amount of Cr(VI) species to be absorbed (mg/g), C_e is the after-adsorption equilibrium concentration (mg/L) and K_L (L/mg) denote the Langmuir coefficient, represents the binding energy associated with the Langmuir adsorption isotherm.

The Langmuir isotherm Equation (3.6) can be rearranged to the following linear form as expressed in Eq (3.7):

$${C_e}/{q_e} = {1}/{K_L q_m} + {C_e}/{q_m} \quad (3.7)$$

By plotting C_e/q_e against C_e with a slope of $1/q_m$ and intercepts of $1/K_L q_m$, one can derive a linear graph and the values of the constants K_L and q_m can be obtained.

The fundamental attributes to predict the feasibility of the Langmuir isotherm were articulated in relation to the dimensionless constant or separation factor (R_L), as denoted by Equation (3.8) (Pradhan et al., 2019):

$$R_L = 1/(1 + K_L C_0) \quad (3.8)$$

where: The adsorption process can be characterized by the relationship between the dimensionless equilibrium parameter R_L. When R_L>1: the outcome is considered unfavourable; if R_L= 1: the outcome is linear; 0 <R_L<1: the outcome is considered favorable; Lastly, when R_L is equal to 0, the outcome is irreversible.

The Freundlich adsorption isotherm was introduced by Freundlich in 1906 as a practical equation that can be used to describe non-ideal sorption characteristics. However, this

phenomenon aligns with the principles of heterogeneous adsorption thermodynamics (Wanees et al., 2012). This is due to the activation of adsorption sites, which presumably results in increased adsorption via the surface exchange mechanism. Unlike the Langmuir model, the Freundlich model assumes that adsorption occurs through multilayer adsorption on a heterogeneous surface and is expressed by Eq. (3.9) (Gunasundari and Kumar, 2017):

$$q_e = K_F C_e^{1/n} \tag{3.9}$$

To transform this equation into a linear form, a logarithmic operation to both sides is applied as follows:

$$\log q_e = \log K_F + {}^{1}/_{n}\ \log C_e \tag{3.10}$$

Where K_F and $1/n$ denote Freundlich constants, which are associated with the adsorption capacity and intensity, respectively. When log q_e is plotted against log C_e, a linear graph is produced where the intercept is log K_F and the slope is $1/n$.

CHAPTER 4

CHARACTERISATION AND APPLICATION OF GRAPHENE OXIDE@MICROALGAE-BASED NANOCOMPOSITES FOR ADSORPTION OF CHROMIUM(VI) FROM AQUEOUS MEDIUM

4.1 Introduction

This chapter discusses the characterization and application of nanostructured GO and NGO@microalgae-based nanomaterials using FT-IR, XPS, SEM, TGA, BET, XRD, and Zeta potential. These techniques were previously covered in Chapter 3, Section 3.2. The synthesis of nanostructured graphene oxide@microalgae-based nanohybrids is presented in Chapter 3, Section 3.1.4. Section 4.2 discusses the physiochemical properties of nanoadsorbents, such as porosity, thermal stability, pore volume, surface area, and surface reactivity. Section 4.3 discusses the impact of adsorption parameters, such as solution pH, adsorption time, initial ions concentration, and adsorbent dose, on the efficacy of the prepared GO@Algae and NGO@Algae nanoadsorbents in removing Cr(VI). Furthermore, the analysis of both the kinetic and isotherm adsorption data was carried out.

4.2 Results and Discussion

4.2.1 FT-IR results

The structural composition of the *Scenedesmus* microalgae, GO, NGO, GO@Algae-(1:1, 3:1, 1:3), and NGO@Algae-(1:1, 3:1, 1:3), was identified using FT-IR spectroscopy with wave numbers between 500 to 4000 cm^{-1}, as depicted in Figure 4.1(a) and (b). The microalgae show *v*N–H peak at 3281 cm^{-1} from amines, Additionally, they also have other functionalities such as amides and amino groups in proteins (Arica et al., 2005). The adsorption bands at 1637, 1543 and 1399 cm^{-1} for microalgae are attributed to O=C–N–H_2, *v*C=N, and N–H bending respectively, which shows the existence of protein-based carbonyl, amide–I, and amide–II bonding (Daneshvar et al., 2019). O–H bending vibrations due to carboxylic acids appear at approximately 1405 cm^{-1}. The adsorption bands around 1246 and 1035 cm^{-1} correspond to C–N and P–O stretching from organic phosphates. For GO and

NGO the major distinctive peaks coincide with findings from previous studies, as they both contain oxygen-related bands (Oliveira et al., 2018; Zafar et al., 2022). A wide and intense peak is observed between 3286 cm^{-1}, which is attributed to the presence of *v*O–H stretches associated with carboxylic acid moieties. The intense absorbance band located at 1726 cm^{-1} is due to the presence of the C=O carbonyl group. The peak at 1391 cm^{-1} can be assigned to the stretching of epoxy groups (C−O−C), whereas the 1051 cm^{-1} band is attributed to the C–O carboxylic stretch band. However, after the N-doping, the intensity of oxygen-containing functional groups in NGO decreased dramatically and some disappeared due to the removal of the oxygen group (Figure 4.1(b)). The NGO spectrum, on the other hand, revealed new broad absorption peaks at 2077 cm^{-1}, confirming the existence of carbohydrate amino groups (–CO–NH– bond) which is due to the nitrogen doping (Zafar et al., 2022). New bands at 1554 and 1209 cm^{-1}, have surfaced, which may be associated with the bending of NH in the newly formed amide groups and the C−N stretching vibrational band. Moreover, the band located at 1720 cm^{-1} in GO shifted to a lower frequency of 1700 cm^{-1} in NGO. This change is caused by the stretching frequency of carbonyl bonds that are generated in the amide groups as a result of the NH_2 bending and the stretching of carboxylic groups. Hence, it can be concluded that N atoms were successfully introduced to the GO lattice.

Meanwhile, all the graphene oxide@algae-based nanohybrids exhibited distinctive GO and algal absorption bands in their FT-IR spectra. For instance, the oxygen-containing functional group peaks related to the vibrational stretching frequency of the C-O epoxy, C-O alkoxy, and C=O carbonyl are observed at 1220, 1041, and 1708 cm^{-1}, respectively. The new peaks are observed at 1591 cm^{-1}, 1270 $cm^{-1,}$ and 731 cm^{-1}, corresponding to strong N=H modes of carbonyl unsaturated ketone amide and C−N, indicating the formation of GO@Algae and NGO@Algae nanocomposites as reported by Gholami et al. (2020). Furthermore, the broad absorption peaks originating from the stretching of NH_2 groups in microalgae at 3280 cm^{-1} and carboxylic OH stretch in GO at 3500–2700 cm^{-1} have fused into two narrow broad bands at 3390 and 3259 cm^{-1}. The NH_2 groups from the algae bind on the GO surface to generate the absorption band, these functional groups are therefore the important sorption sites.

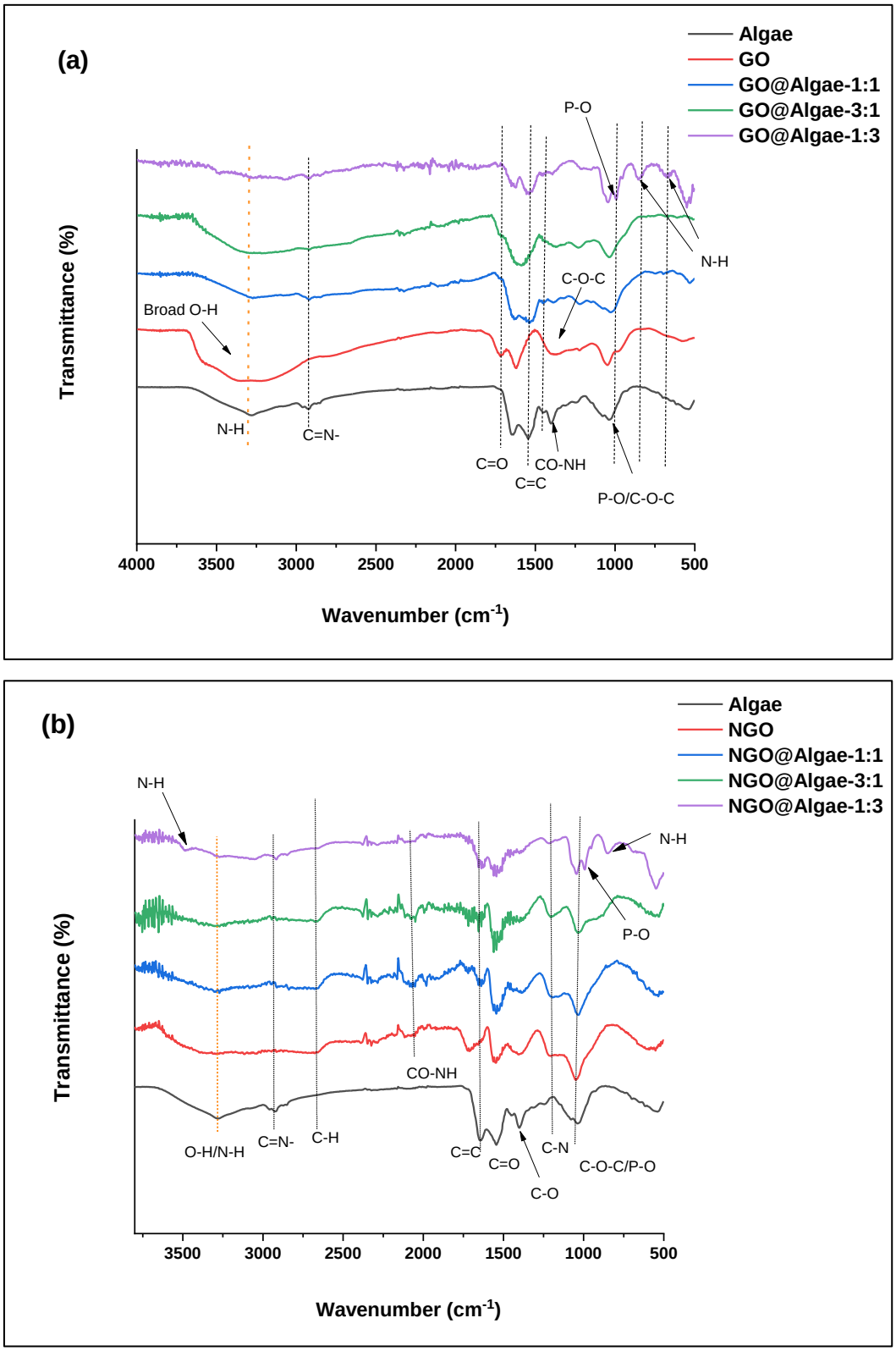

Figure 4.1: FTIR spectra for (a) Algae, GO and GO@Algae nanocomposites and (b) spectra of NGO and NGO@Algae nanocomposites.

4.2.2 UV−Visible Spectroscopy Analysis

Figures 4.2(a) and (b) show the UV-Vis absorption spectra of the microalgae, GO, GO@Algae-(1:1, 3:1, 1:3), NGO, and NGO@Algae-(1:1, 3:1, 1:3). The UV-vis results revealed that their optical properties were substantially different. Figure 4.2(a) displayed pure GO with two distinct absorption peaks: a sharp absorption peak at 230 nm, which indicated the π–π* transition of aromatic C–C bonds, and a shoulder peak at 304 nm, corresponding to the n–π* transitions of C=O bonds (Johra et al., 2014). On the other hand, a new absorption peak at 262 nm was introduced in NGO, which indicates the formation of carbon-nitrogen bonds such as amine, C=N, and pyridine groups on the lattice of GO. In addition, the n–π* shoulder peak observed at ∼304 nm disappeared, suggesting that some groups on the GO surface were eliminated and the conjugated structure was restored after N doping (Figure 4.2(b)) (Kumar et al., 2017).

Meanwhile, when GO and NGO were modified with different algae content, the observed peak at 230 nm shifted to a longer wavelength (red-shift) of 257, and 268 nm for GO@Algae-(1:1, 1:3) and 230 to 226 nm for NGO@ Algae-(1:1, 3:1, 1:3), respectively though the peaks seems to disappear. This indicates the formation of microalgae in GO@Algae and NGO@Algae nanocomposites. However, the shoulder peak around 305 nm disappeared due to a reduction in the content of oxygen functionalities and an increase in aromatic rings, causing electrons to be easily excited at lower energy (Gholami et al., 2020). This signified an enhancement in the π-electron concentration and structural ordering, as well as the restoration of sp^2 carbon in the GO and NGO system (Chang et al., 2021).

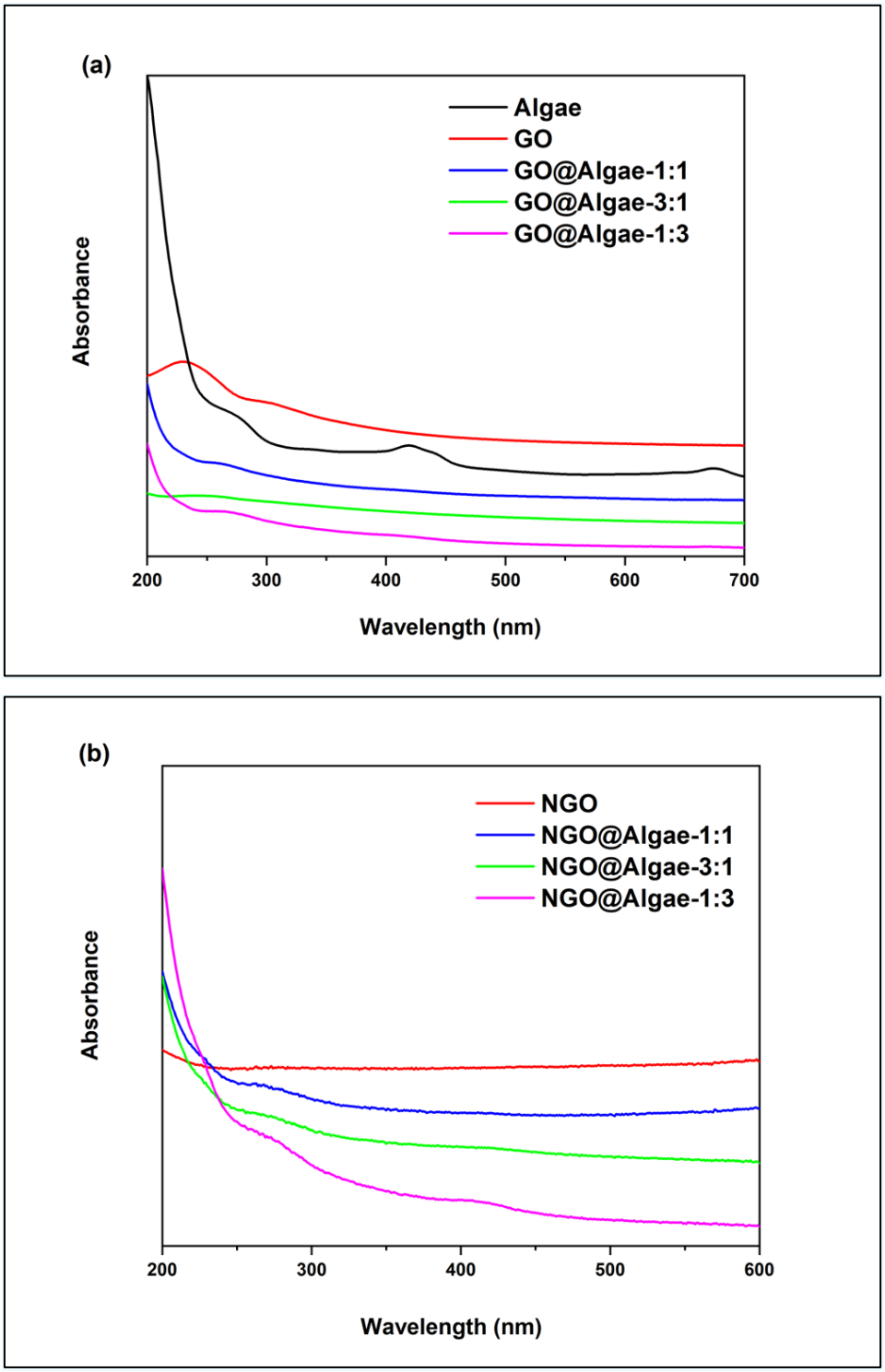

Figure 4.2: UV-vis spectra for (a) Algae, GO and GO@Algae composites and (b) spectra of NGO and NGO@Algae nanocomposites.

4.2.3 Structure and morphology of GO and NGO@Algae nanohybrids

The morphologies of algae, GO, NGO, GO@Algae and NGO@Algae nanohybrids were characterised using SEM imaging. SEM images are presented in Figure 4.3. Generally, the algae gave uneven flake-like morphology, while images of GO and NGO showed sheet-like and irregular morphological layers that are stacked against each other. In addition, the modified GO and NGO@Algae nanocomposites showed loosely stacked nanosheets compared to the bare GO and NGO nanosheets. The improvement in agglomeration of GO and NGO nanosheets and dispersion in the presence of algae suggested good compatibility between the microalgae and the matrices, resulting from excellent interfacial interaction. The GO@Algae and NGO@Algae nanocomposites images revealed a rough surface (Figure 4.3). The uneven surface morphology of the GO@Algae and NGO@Algae nanomaterials was ideal for enabling the algae nanofiller to offer a greater number of binding active sites, including defects in the form of pores and vacancies. Hence, the presence of pores and vacancies in the GO@Algae and NGO@Algae nanomaterials was the critical parameter responsible for the enhanced sorption performance.

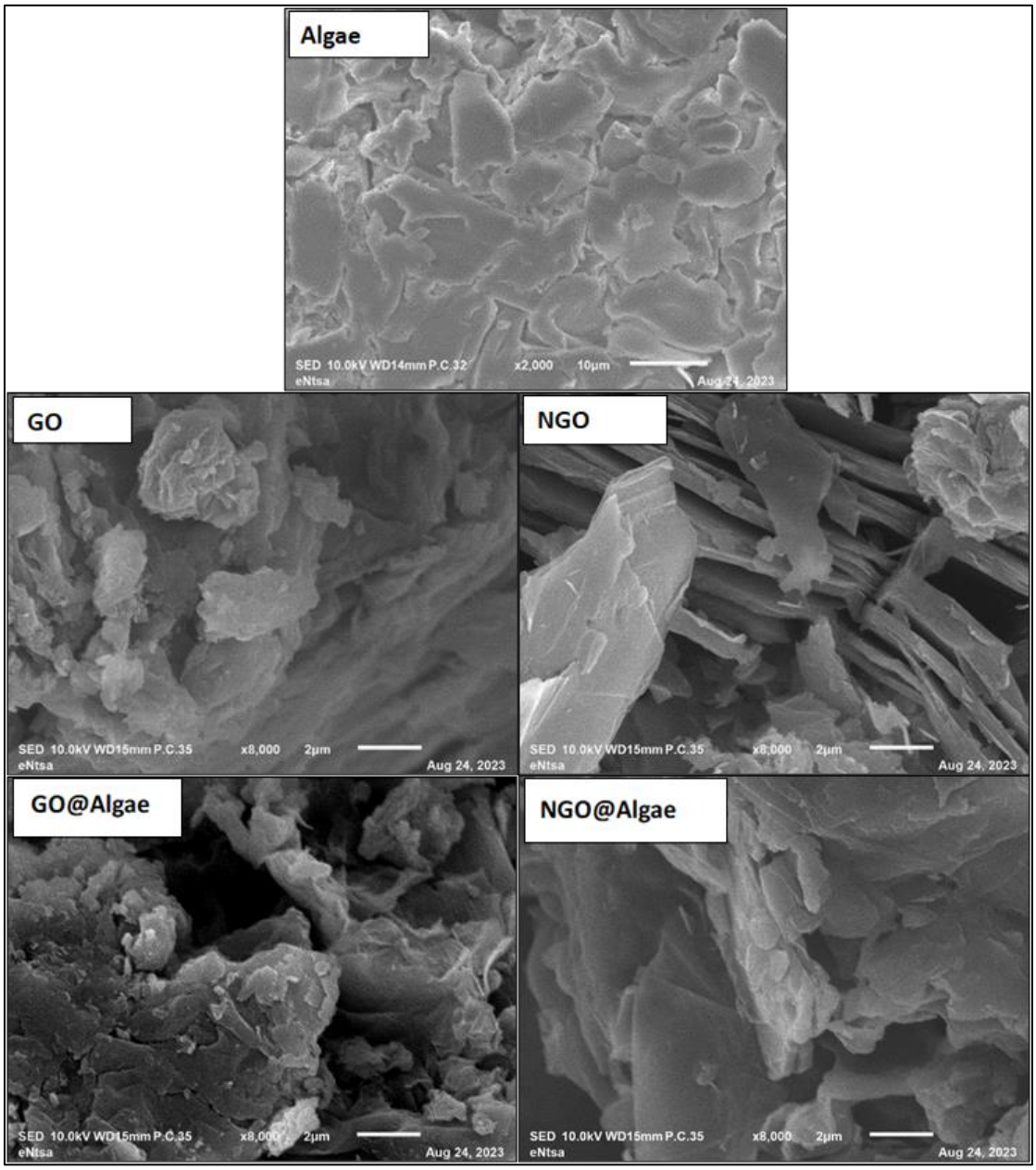

Figure 4.3: SEM micrographs for pure algae, GO, NGO, GO@Algae and NGO@Algae.

4.2.4 XRD results

X-ray diffraction measurements were carried out to identify the phases of the native GO, NGO, GO@Algae, and NGO@Algae-based nanocomposites. The recorded XRD scans of the nanohybrids are given in Figure 4.4. Corresponding crystallite size values has been determined by the Debye-Scherrer equation (4.1) as reported in Table 4.1. The diffraction

pattern in Figure 4.4(a) for GO showed a strong crystal plane peak at 2θ = 11.2° (001), which corresponds to an interlayer spacing of approximately 0.74 nm. This peak serves as an indication of the existence of oxygen functional groups within the GO lattice. After N-doping GO, the 2θ = 11.2° peak completely disappeared and a new peak at 2θ = 26.9° (002) emerged, which was due to the removal of the oxygen functional groups and intercalated water molecules into the GO lattice (Figure 4.4(b)) (Kumar Jaiswal et al., 2017b)). When the GO and NGO are modified with algae, the XRD scans of the nanocomposite show algae and GO diffraction peaks. The diffraction peaks of the incorporated GO materials diminish with an increase in the amount of microalgae added and there is a slight shift of the diffraction peaks observed. In comparison with GO@Algae and NGO@Algae, the intensity of the diffraction peak at 2θ = 26.3° (002) and 2θ = 50.5° (101), attributed to the NGO@Algae structure, appeared progressively when the NGO: Algae content was equivalent (1:1).

$$D = \frac{K.\lambda}{\beta.cos\theta} \qquad (4.1)$$

Where K is the broadening constant (0.94), λ is the X-ray wavelength (0.15406 nm), β is the area that corresponds to half of the maximum area at the peak point (FWHM), and θ is a diffraction peak position.

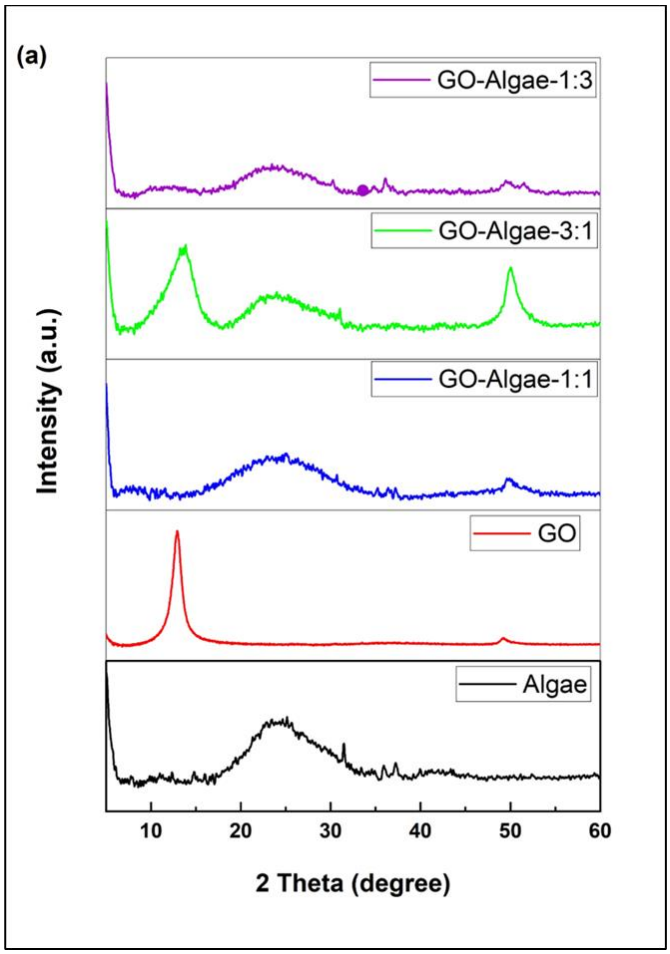
(a)
GO-Algae-1:3
GO-Algae-3:1
GO-Algae-1:1
GO
Algae
Intensity (a.u.)
10
20
30
40
50
60
2 Theta (degree)

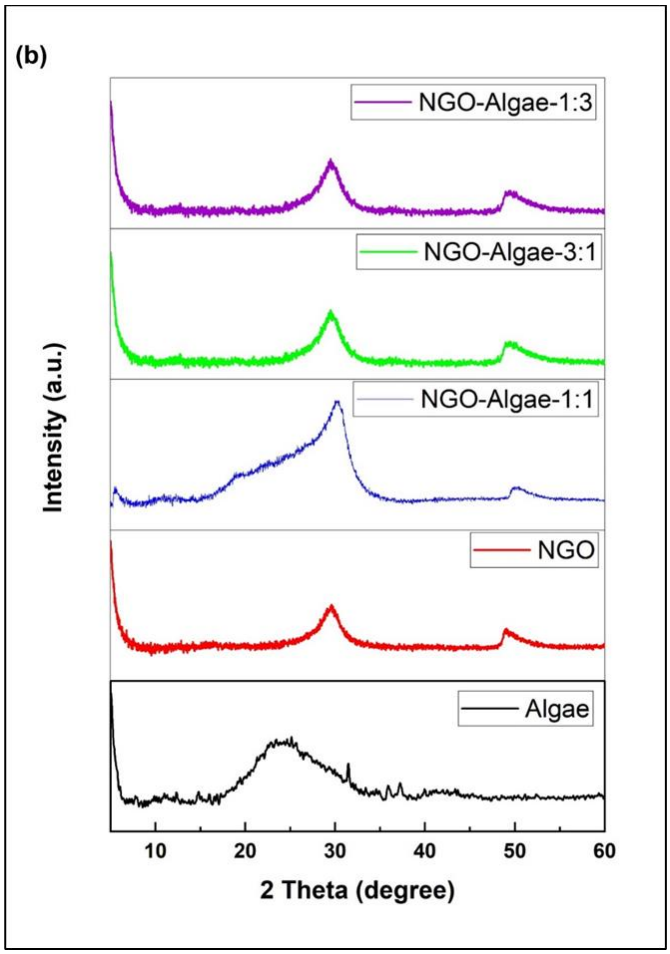

Figure 4.4: XRD spectra for (a) Algae, GO and GO@Algae nanocomposites and (b) spectra of NGO and NGO@Algae composites.

Table 4.1: XRD crystallite size of the synthesized nanocomposite materials

Nanoadsorbent	Peak position	FWHM	Average crystallite Size (nm)
Algae	24.93, 35.92 and 37.23	8.4242, 0.3297 and 0.391	2.612
GO	12.89	1.535	5.371
GO@Algae-1:1	24.58 and 50.55	11.183 and 4.511	1.001
GO@Algae-3:1	13.43, 24.39 and 50.19	2.828, 7.179 and 2.498	1.926
GO@Algae-1:3	11.63, 24.05, 36.10 and 49.90	5.752, 7.779, 0.706 and 1.294	2.062
NGO	29.57, 49.29 and 62.86	3.658, 2.647 and 5.287	1.967
NGO@Algae-1:1	20.99, 30.16 and 50.60	6.979, 3.683 and 4.507	1.570
NGO@Algae-3:1	29.57, 49.77 and 63.36	3.517, 3.276 and 3.216	2.276
NGO@Algae-1:3	29.61, 49.90 and 63.36	3.634, 2.929 and 2.529	2.505

4.2.5 BET analysis

The total pore volume, pore size, and surface areas of the GO, GO@Algae and NGO@Algae are provided in Table 4.2. GO had a significantly greater surface area of 34.801 m^2/g with an average pore size of 9.02 nm, which was notably higher than the surface area of microalgae at 8.189 m^2/g with an average pore size of 0.22 nm. The surface area of microalgae was determined to be consistent with 18.02 m^2/g and the total pore volume of 0.0011 cm^3/g reported by previous researchers (Esmaili et al. (2023). Incorporating the GN-

based materials with algae changed the surface area of the nanocomposite materials. It was observed that the surface area of the nanohybrid materials GO@Algae-1:1 decreased to 9.305 m^2/g (refer to Table 4.2). Kim et al. (2022) reported that the incorporation of GN-based materials with microalgae does have an effect on the surface area and the pore size. Additionally, it was noted that the GO@Algae-1:3 and NGO@Algae-1:3 composites, which had a higher proportion of microalgae, displayed lower surface area, pore volume, and pore size than their counterparts. The observed reduction in surface area, as well as the decrease in pore size and volume for the GO@Algae and NGO@Algae samples, was attributed to the partial restacking of GN layers and the presence of blocked pores. The results obtained from the BET analysis are consistent with the XRD findings presented in Section 4.2.4, Figure 4.4.

Table 4.2: BET surface area, pore volume and pore size of the synthesized nanocomposite materials

Nanoadsorbents	BET surface area (m^2/g)	Total pore volume (cm^3/g)	Pore size (nm)
Algae	8.189	0.037	0.22
GO	34.801	0.044	9.02
GO@Algae-1:1	9.305	0.037	1.20
GO@Algae-3:1	5.839	0.033	0.83
GO@Algae-1:3	4.376	0.025	0.85
NGO	15.218	0.035	3.88
NGO@Algae-1:1	7.957	0.028	1.06
NGO@Algae-3:1	9.206	0.034	1.27
NGO@Algae-1:3	5.489	0.021	1.05

4.2.6 TGA results

Thermal analysis (TA) enabled the identification of mass losses and thermal transitions that occurred during the decomposition of samples through the interpretation of TGA/DTG curves, which are shown in Figure 4.5 (TGA curves over time are shown in Figure 4.5 (a) and (c) and DTG curves are depicted in Figure 4.5 (b) and (d). The degradation pattern of microalgae biomass was comparable to that of GO and NGO. However, the TGA profile of microalgae combustion revealed three distinct phases. The initial stage ranges from 43 °C to around 150 °C, can be associated with moisture loss. Then, a significant amount was lost around 150 to 350 °C, identified as a loss of 51.40% due to the release and combustion of volatile matter on the DTG curve (Chen and Torii, 2015; Alves et al., 2019)). Moreover, the second drop exhibited two zones of devolatilization: zone one (peak 1 around 210 °C in Figure 4.5) was linked to the burning of proteins and carbohydrates, while zone two occurred at high temperatures from 260 to 600 °C was attributed to the combustion of lipids and char and about 38% of the residual mass remained. Similar results have been reported in the literature for microalgae (Alves et al., 2019).

Moreover, the TGA analysis of GO, NGO, GO@Algae-(1:1, 3:1, 1:3), and NGO@Algae-(1:1, 3:1, 1:3) was performed to elucidate its thermal behaviour and chemical composition. The decomposition of GO was consistent with previous studies (Paredes et al., 2008; Jiang et al., 2019). The thermograph obtained (Figure 4.5 (a)-(d)) exhibited three major stages of decomposition in the temperature range of 50–600 °C. The first stage of GO and GO@Algae composite showed a low weight loss of ~below 10%, while NGO and NGO@Algae composite showed weight loss of ~below 5% at temperature below 100°C, which corresponds to the loss of adsorbed water into its structure. The degradation temperatures shifted towards lower temperatures when algae biomass was added to unmodified GO nanohybrids, (see Figure 4.5 (b)). In addition, the GO@Algae nanohybrids had deteriorated at lower temperatures compared to the bare GO. Whereas the NGO@Algae nanocomposites decomposed at higher temperatures compared to the bare NGO (see Figure 4.5 (c)). This was supported by the temperature derivative curves in Figure 4.5 (d), showing a shift in the main thermal decomposition temperatures. The significant second-step inflexion observed in TGA curves, from 100 to about 220°C, was attributed to the vaporization of water molecules and the decomposition of most stable oxygen and nitrogen-containing functionalities into gas by-products. For GO@Algae-1:1, GO@Algae-3:1 and GO@Algae-

1:3, similar thermal decomposition patterns to that of the NGO@Algae-1:1, NGO@Algae-3:1 and NGO@Algae-1:3 were observed; however, the residual weight percentages and the decomposition temperatures varied with the algae amounts. The total weight loss of GO@Algae-1:3 (55.2wt%) and NGO@Algae-1:3 (43.1wt%) was significantly greater than that of their counterparts, suggesting a larger content of organic compounds introduced from the microalgae in GO@Algae-1:3 and NGO@Algae-1:3 (see Figure 4.5 (a) and (c)).

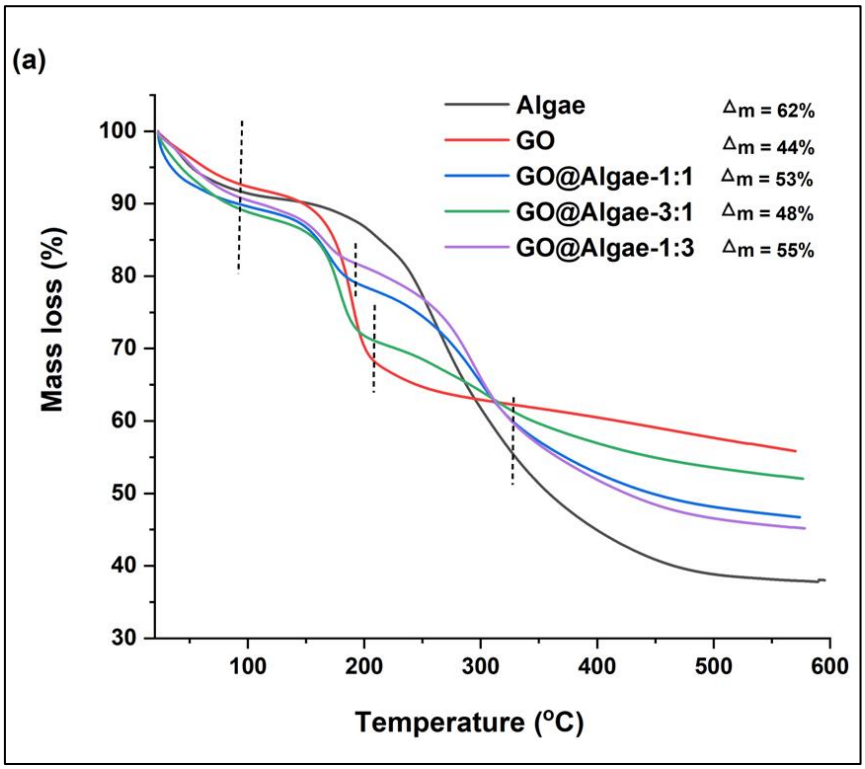

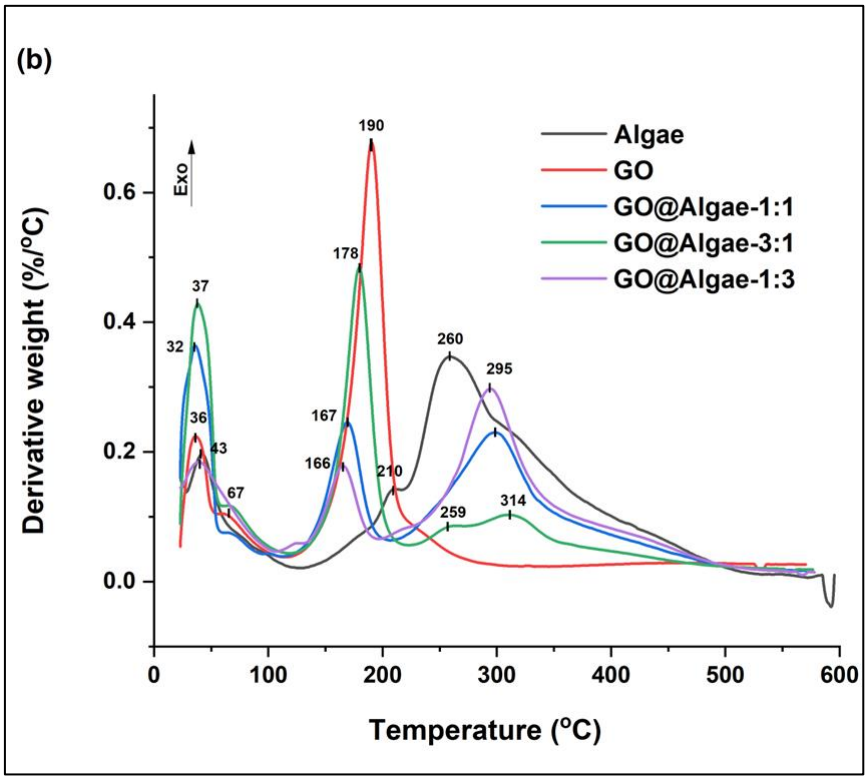
(b)
Derivative weight (%/°C)
Temperature (°C)
Exo
Algae
GO
GO@Algae-1:1
GO@Algae-3:1
GO@Algae-1:3
190
178
37
32
260
295
36
167
43
166
210
67
259
314
0.0
0.2
0.4
0.6
0
100
200
300
400
500
600

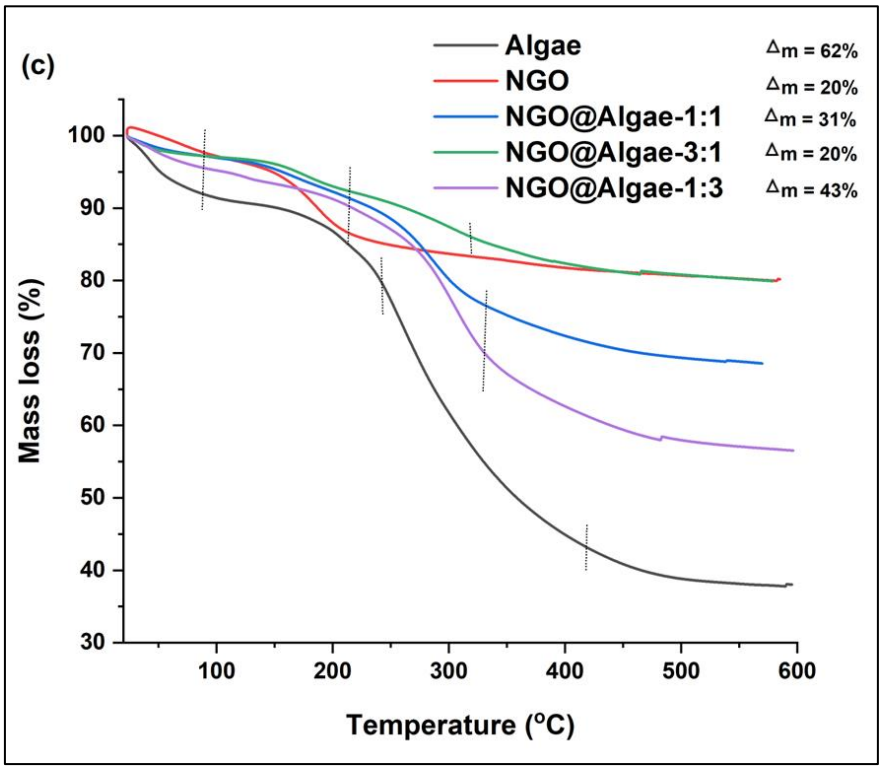
(c)
Mass loss (%)
Temperature (°C)
Algae
NGO
NGO@Algae-1:1
NGO@Algae-3:1
NGO@Algae-1:3
Δm = 62%
Δm = 20%
Δm = 31%
Δm = 20%
Δm = 43%
30
40
50
60
70
80
90
100
100
200
300
400
500
600

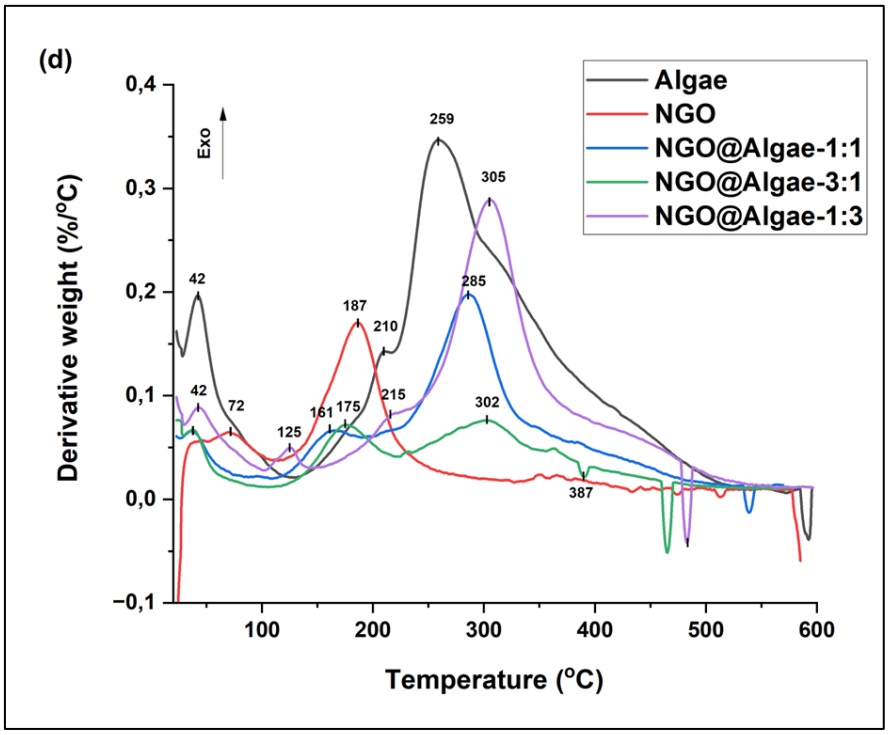

Figure 4.5: TG (a) and DTA (b) curves of Algae, GO and GO@Algae composites and (c) and (d) NGO and NGO@Algae composite respectively.

4.2.7 Zeta potential

The data depicted in Figure 4.6 indicates that the zero-point charge (pH_{pzc}) of modified GO and NGO with microalgae shifted to a lower pH value as a result of the incorporation of newly introduced oxygen and nitrogen-containing moieties. The nanoadsorbents' surface charge became increasingly negative as the pH increased, which led to electrostatic interactions and created a favourable environment for higher adsorption of cationic metal ions at higher pH levels. The zeta potential of GO@Algae (-45.9 mV) and NGO@Algae (-50.9 mV) became more negative as the pH increased and their point of zero charge (PZC) was reached at pH 2.02, respectively. These findings indicated that the surfaces of GO@Algae and NGO@Algae exhibited a positive charge when the pH values were below the PZC. Prior studies showed that modified GO nanomaterials had a lower negatively charged surface (-12.5 mV) compared to raw GO (-9.2 mV), as indicated by their zeta potential values. When pH is below the pHpzc value, the surface of the adsorbent becomes increasingly negatively charged, leading to an increase in the potential for electrostatic

interaction between the adsorbent and anionic metal ions (Daneshvar et al., 2019). At pH = pH_{pzc}, the attractive force exactly balances this electrostatic repulsive force. Thus, at pH < pH_{pzc}, the adsorption of anionic metals is primarily influenced by the attractive electrostatic forces.

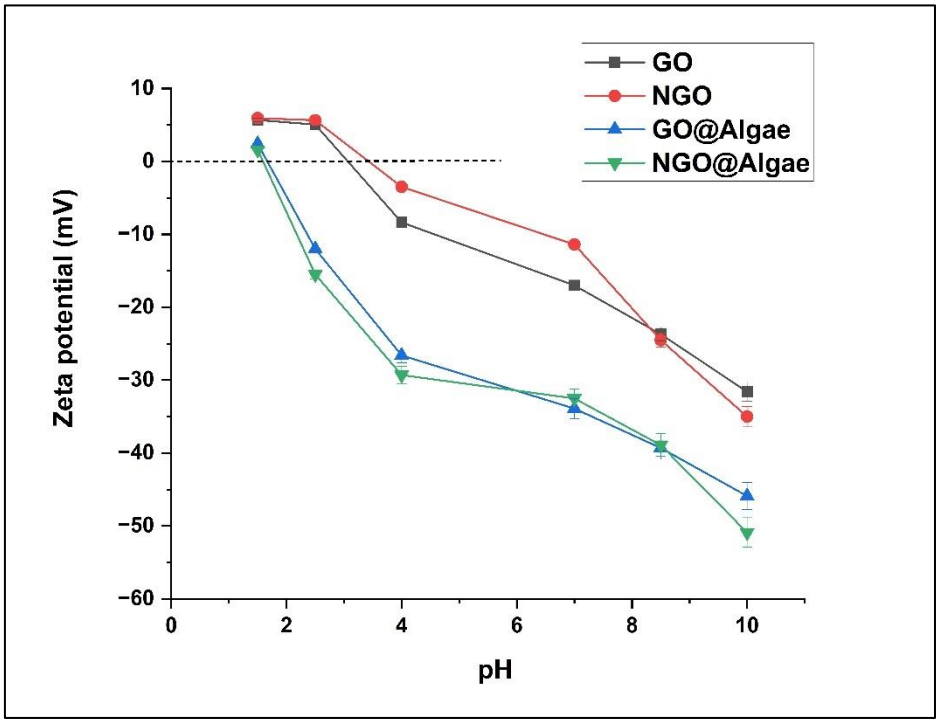

Figure 4.6: Zeta potential for GO, NGO, GO@Algae and NGO@Algae nanocomposites.

4.3 Cr(VI) sorption studies

The adsorption behaviour of chromium species on graphene@microalgea-based nanohybrids as adsorbents was determined under the influence of a number of parameters, including contact time, pH, adsorbent dose, and the initial adsorbate concentration.

4.3.1 Effect of pH

The pH test findings depicted in Figure 4.7 demonstrated that the removal efficiency of all the samples decreased as the pH of the solution increased, due to alterations in the surface chemistry of the adsorbents. When the pH value was low, the adsorbent's surfaces underwent protonation of oxygen and nitrogen-containing groups, resulting in a positive charge, whereas Cr^{6+} species in an aqueous solution had negative charges. Consequently, the nanocomposite exhibited the capacity to form a binding interaction with Cr(VI) ions due to the strong electrostatic adsorption between the positively charged functional groups of the nano-biosorbents and the negatively charged Cr^{6+} species. On the other hand, with an increase in pH, the deprotonation of oxygen- and nitrogen-containing groups occurred, resulting in the biosorbent acquiring a positive charge, this deprotonation is confirmed by the zeta potential result in section 4.2.7. As a result, the presence of anion chromium species and OH^- ions led to a competitive process for adsorption sites on the nano-biosorbent. This phenomenon can account for the observed decrease in the removal efficiency of Cr(VI) at elevated pH levels. Other investigations have also documented similar behaviour when different graphene oxide-based adsorbents were used for the removal of Cr(VI) (Setshedi et al., 2015).

At a lower pH of 2, the composites GO@Algae-1:1, GO@Algae-3:1, and GO@Algae-1:3 showed significant percentages of Cr(VI) removal, specifically 98.7%, 90.5%, and 99.6% respectively. In contrast, unmodified GO revealed a lower removal percentage of 74.5% (refer to Figure 4.7(a)). A comparable pattern was noted in the case of NGO@Algae nanocomposites. The Cr(VI) removal efficiencies for NGO, NGO@Algae-1:1, NGO@Algae-3:1, and NGO@Algae-1:3 were found to be 85.9%, 82.3%, 79.2%, and 91.6%, respectively, as depicted in Figure 4.7(b). The findings of this study suggest that the integration of microalgae into the GO and NGO matrix has resulted in the development of GO@algae and NGO@algae nanoabsorbents with improved functional groups that influence adsorption. These nanoabsorbents exhibited enhanced surface chemistry properties and demonstrated a high capacity for efficiently adsorbing chromium species. Indeed, the GO@Algae-1:3 and NGO@Algae-1:3 samples have demonstrated high removal capability in comparison to their respective counterparts, as depicted in Figure 4.7(a) and (b). This phenomenon can be explained by two factors: an increased quantity of available

binding sites on the microalgae and the presence of distinct compounds within the microalgal cell wall (Gokhale et al., 2009 and Arica et al., 2005).

The predominant species of hexavalent chromium (Cr(VI)) in a water-based solution is shown to change depending on the pH of the solution (Nithya et al., 2019). In an aqueous solution, the presence of Cr(VI) species was observed within a pH range of 2 to 6, where $HCrO_4^-$ species is predominant at pH 2 and a mix of $Cr_2O_7^{2-}$ and CrO_4^{2-} species was predominant at pH 5 (Al-Homaidan et al., 2018). Consequently, the study investigated how the adsorption performance of the nanoadsorbents was affected by changing the pH of the Cr(VI) solution. The study was conducted in pH 2 and 5 at an initial concentration of 10 ppm, adsorbent dosage of 0.05 g and under room temperature conditions for 6 h of adsorption time to determine their adsorption performance. The preliminary experiment was carried out for all samples, including algae, GO, NGO, GO@Algae, and NGO@Algae. The dependence of Cr(VI) removal efficiency and adsorption capacity on solution pH is evident in Figure 4.7.

These factors play a significant role in facilitating the synergistic impact observed in the composition of GO and NGO. It was postulated that having more adsorption sites would facilitate the binding of a higher quantity of Cr(VI) due to the strong electrostatic attraction between the active sites of the adsorbents and the adsorbate. Therefore, a comprehensive investigation was conducted on the GO@Algae-1:3 and NGO@Algae-1:3 nanoadsorbent, with the aim of assessing their efficacy under various batch mode adsorption conditions in order to identify the optimal performance. It was determined that pH 2 is the optimal environment for the adsorption of Cr(VI). Consequently, all further experiments conducted in this study were performed at the optimal pH of 2.0 in order to attain the maximum Cr^{6+} removal.

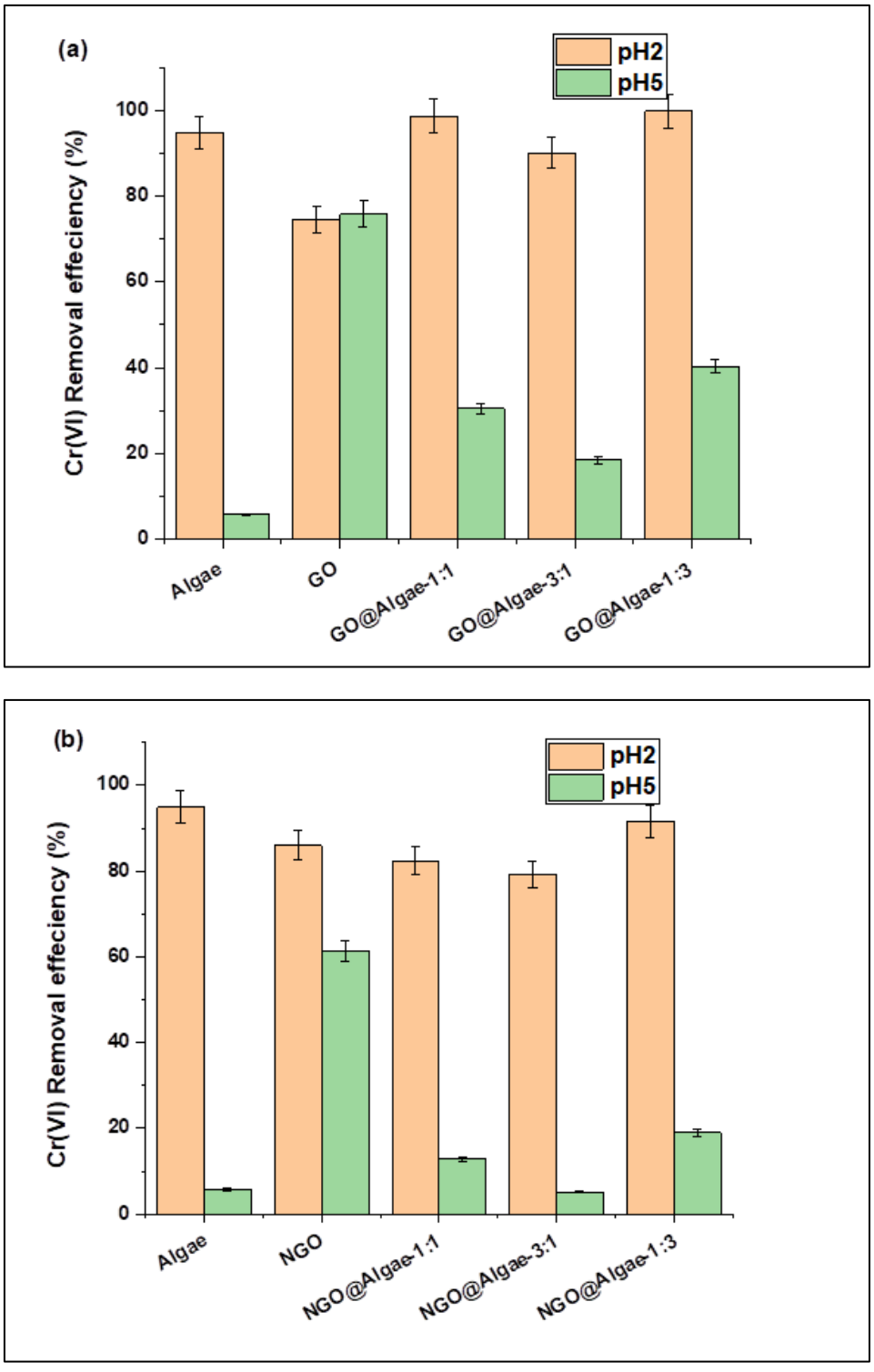

Figure 4.7: Removal efficiency provided by (a) algae, GO and different GO@Algae and (b) NGO and different GO@Algae samples at initial Cr(VI) concentration = 10 mg/L, adsorbent dosage = 0.05 g, contact time = 360 mins, pH 2 and 5 and temperature = 30 °C.

4.3.2 Effect of initial concentration

In this study, the impact of initial concentration on the efficacy of GO, NGO, and GO@Algae-1:3 nanocomposites in removing Cr(VI) ions was investigated at initial concentrations of 5, 10, 20, 50, and 80 mg/L, a pH of 2, and an adsorption time of 360 min. Figure 4.8 shows the trend of Cr(VI) ion adsorption at different concentrations for different nanohybrids. The study revealed that when the initial concentration of Cr(VI) increased, the removal efficiency declined, while the adsorption capacity increased. The high removal of Cr(VI) at lower concentrations is because there are more surface-binding sites on the nanoadsorbents than adsorbate species in the solution. Therefore, when the concentration is low, there are sufficient active sites on the nanoadsorbent's surface to interact with all the metal ions in the aqueous solutions (Pradhan et al., 2019).

It can be noticed that the removal percentage for GO was comparatively lower than that of NGO due to the tendency of GO to form aggregates because of its strong interplanar contacts, leading to a decrease in surface area (Yang et al., 2019). Therefore, this resulted in a decrease in its adsorption performance. On the other hand, NGO exhibited a significant maximum removal percentage of approximately 99% at lower concentrations. This high removal efficiency was attributed to the incorporation of nitrogen atoms on the surface of GO nanosheets, which induced defects and enhanced the number of binding sites accessible for adsorption applications, this was confirmed by the FTIR and XPS results (Yokwana et al., 2018). Most importantly, the results demonstrated a notable decline in removal efficiency, with GO@Algae-1:3 and NGO@Algae-1:3 exhibiting a reduction from 100 to 74.5% and 98.6 to 80.2%, respectively (refer to Figure 4.8). The results suggested that both nanocomposites have exceptional properties as adsorbent materials.

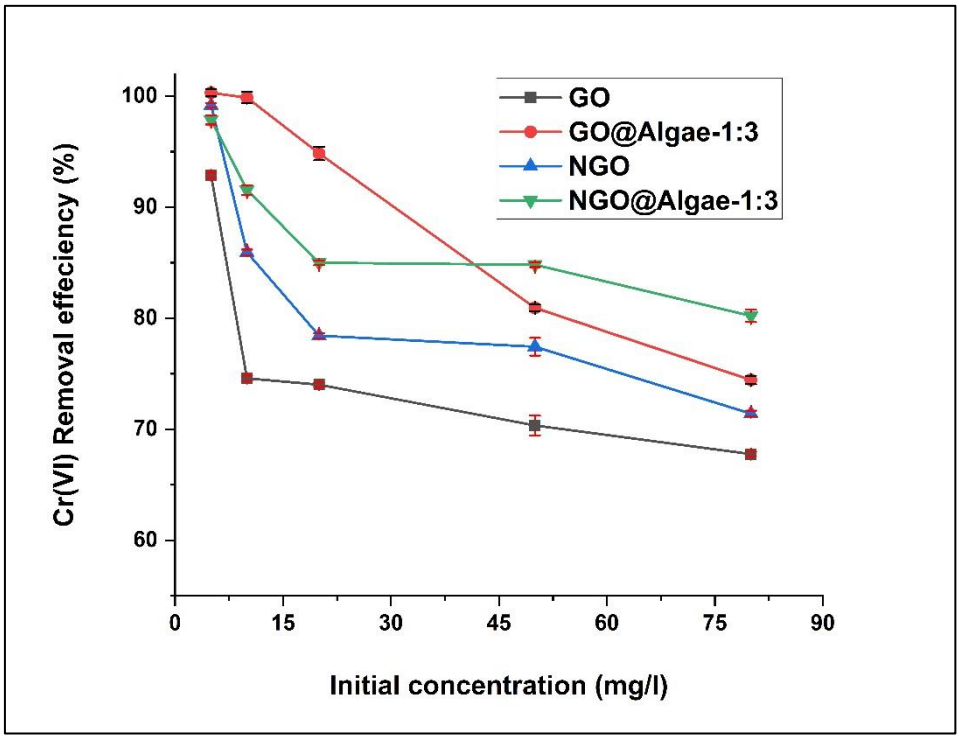

Figure 4.8. The effect of initial Cr(VI) concentration on its removal by GO, NGO, GO@Algae and NGO@Algae nanocomposites.

4.3.3 Effect of graphene oxide@algae-based loading

Figure 4.10 demonstrates the corresponding results for the Cr(VI) removal % and adsorption rate after 360 mins at pH 2 as a function of the additional amounts of nanoadsorbents. The findings showed that the removal efficiency of Cr(VI) increased as the amount of adsorbent used increased for all the samples (Fig. 4.9(a)). As the amount of adsorbent increases, more active sites are available for interacting with the Cr(VI) species, which results in an increase in removal (Setshedi et al., 2015). On the contrary, the adsorption capacity was indirectly proportional to the dosage of the adsorbent because it decreased with an increase in the adsorbent dosage (Fig. 4.9(b)). In the case of bare GO and NGO, it was discovered that the NGO exhibited a better removal percentage and adsorption capacity than the unmodified GO, owing to the formation of defects and the introduction of nitrogen-containing moieties during the N doping (Song et al., 2021).

The removal percentage of GO, NGO, GO@Algae, and NGO@Algae increased from 22.4 to 95.9%, 41.7 to 100%, 29.6 to 100%, and 13.2 to 100%, respectively. Meanwhile, the

adsorbent capacity exhibited decreased from 12.33–1.36 mg/g, 22.98–1.38 mg/g, 16.28–1,38 mg/g, and 7.27–1.38 mg/g for GO, NGO, GO@Algae-1:3, and NGO@Algae-1:3, respectively. This phenomenon occurs due to the restricted binding of Cr species to the sites at specific chromium solution concentrations, resulting from the higher number of adsorptive sites at increased adsorbent doses. The same behaviour was consistent with that seen by other researchers when using carbon-based material for the removal of Cr^{6+} species (Baby et al., 2019; Sabzehmeidani et al., 2021).

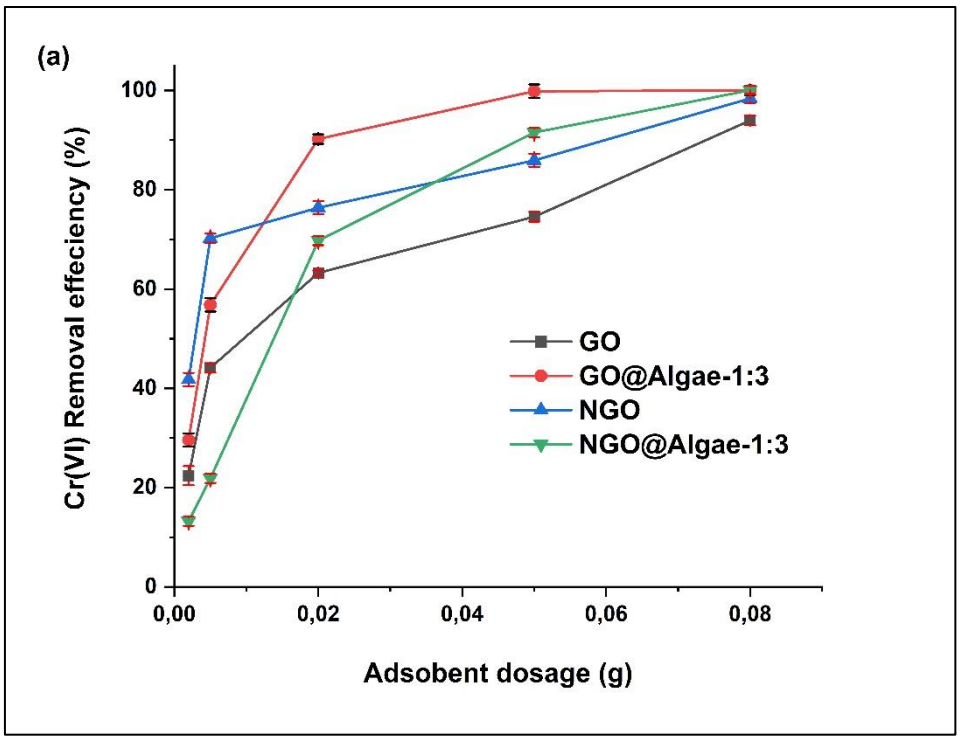

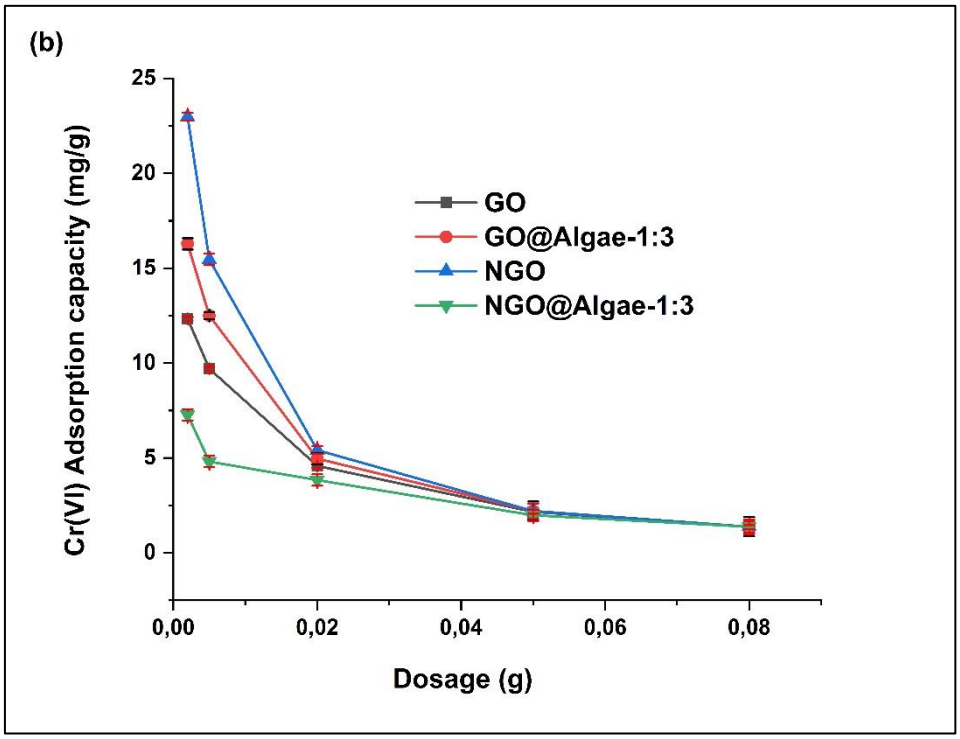

Figure 4.9: Effect of adsorbent loading on Cr(VI) removal and adsorption capacity [Conditions: Contact time (360 mins), pH 2, Initial Concentration (10 mg/L), 250 rpm].

4.3.4 Effect of contact time

The data presented in Figure 4.10 demonstrates the relationship between contact time and the removal percentage as well as the adsorption capacity of Cr(VI) ions. Understanding the impact of contact time is crucial for assessing the effectiveness of a nanoadsorbent. The effect of time studies on the adsorption of the Cr ion were conducted at contact time intervals ranging from 10, 30, 60, 90, 180, and 360 mins, with an initial concentration of 10 mg/L Cr(VI) and pH 2 using 0.05 g of adsorbents. It is evident that both the removal percentage and adsorption capacity increase as the contact time increases. Figure 4.10 shows that the adsorption of Cr(VI) increased rapidly within the first 90 min, followed by a gradual increase up to 360 min. The GO and NGO nanomaterials exhibited a maximum removal rate and adsorption capacity of 75% (1.64 mg/g) and 86% (1.89 mg/g), respectively. The adsorption abilities of GO@Algae-1:3 and NGO@Algae-1:3 nanocomposites were higher than those of unmodified GO and NGO nanosheets. The maximum removal% and adsorption capacity for GO@Algae-1:3 and NGO@Algae-1:3 were found to be 100% (2.24 mg/g) and 92% (2.01

mg/g), respectively. The primary factor contributing to the initial enhancement in efficiency can be attributed to the abundant availability of unoccupied adsorption sites on the adsorbent material (Nasreen et al., 2008). However, over time, these vacant sites slowly become occupied.

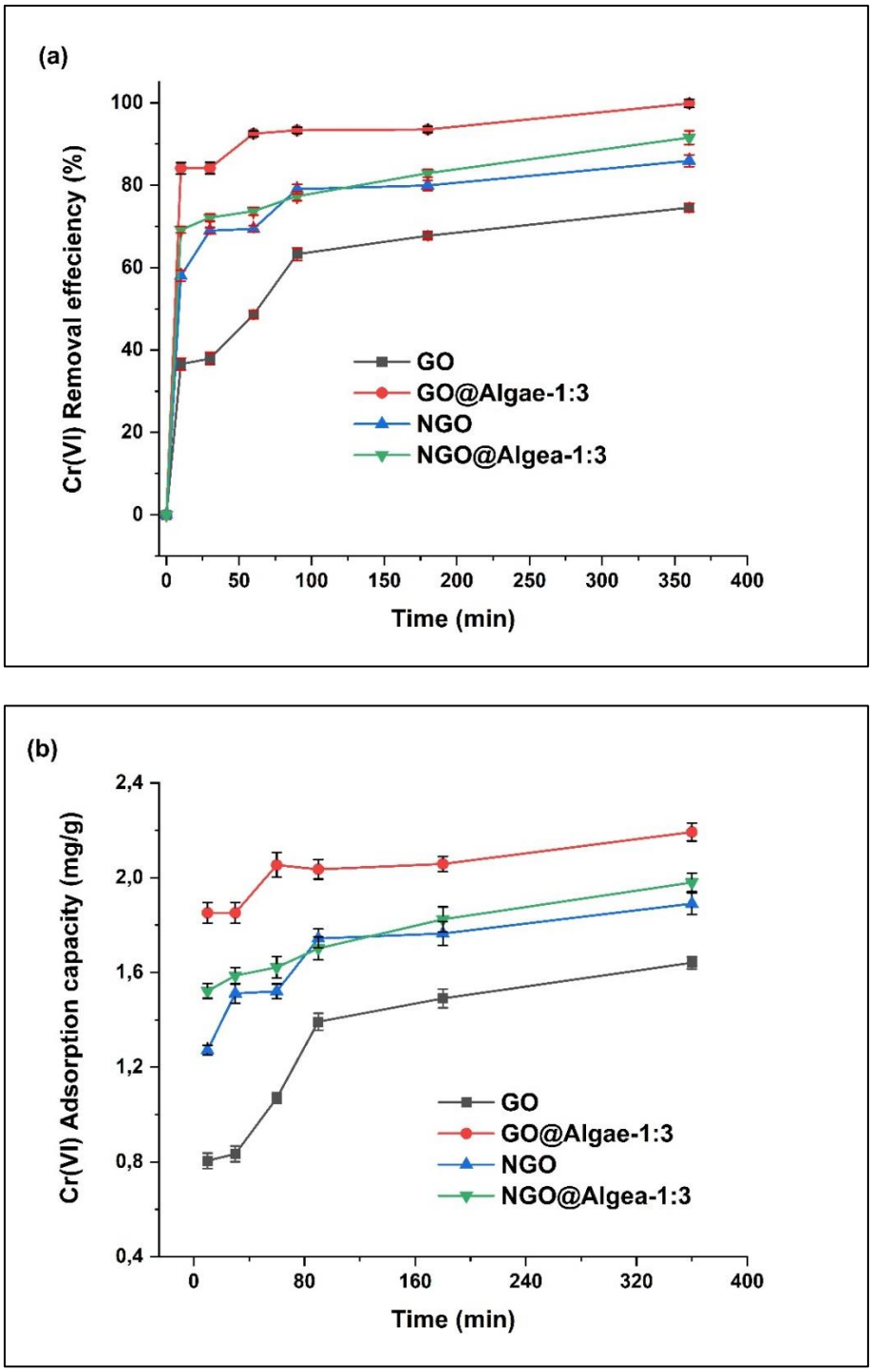

Figure 4.10: Effect of adsorption time on the uptake of Cr^{6+} by GO, NGO, GO@Algae and NGO@Algae nanohybrids.

4.3.5 Adsorption kinetic studies

In order to understand the rate constant of adsorption and adsorption mechanism of Cr^{6+} ions onto GO@algae-1:3 and NGO@algae-1:3 nanocomposites. The PFO, PSO, and IPD kinetic models were employed (see Figure. 4.11(a)-(c)), as outlined in Chapter 3, Sub-Section 3.3.1. A linear correlation was seen between the PFO and PSO graphs, as depicted in Figure 4.11(a) and (b), correspondingly. According to the correlation coefficient (R^2), the PFO exhibits lower values compared to the PSO, with R^2 exceeding 0.9950, indicating a stronger proximity to 1, as demonstrated in Table 4.3. These results consequently show that for all adsorbents, the adsorption data fitted better with the PSO model. This further confirms the chemisorption process via complexation. Similar findings were reported on the adsorption of Cr(VI) ions by GO-based nanoadsorbents (Nasreen et al., 2008). Furthermore, the findings presented in Table 4.3 show that the equilibrium adsorption values (q_e) obtained from theoretical calculations are similar to those of the actual experimental values. The adsorption capacities are revealed to be in the following order: GO@Algae > NGO@Algae > NGO > GO.

The Cr(VI) ion adsorption processes of GO@algae and NGO@algae are illustrated in Figure 4.11(c) and Table 4.4. These results indicate that the adsorption occurs in two distinct stages, implying that the process involves various diffusion stages within the adsorbents' interior and on their surfaces (Nithya et al., 2019). During the first phase, the process of adsorption exhibits rapid kinetics, resulting in a steep slope of the adsorption curve. This is due to the abundance of available binding sites that are readily accessible for adsorption. Then, after 30 min of adsorption, the process transitions into its second stage, characterized by the diffusion of Cr(VI) ions into pores which is slower than that occurred during the first stage (Xu et al., 2022). Moreover, Table 4.4 reveals that the K_p values associated with the initial stage exhibit greater significance compared to those of the subsequent stage. In the second stage, the R^2 values are closer to 1, indicating a higher correlation. This suggests that pore diffusion may be an additional component that affects the transportation of Cr(VI) ions within the adsorbent structure (Rangabhashiyam and Balasubramanian, 2019).

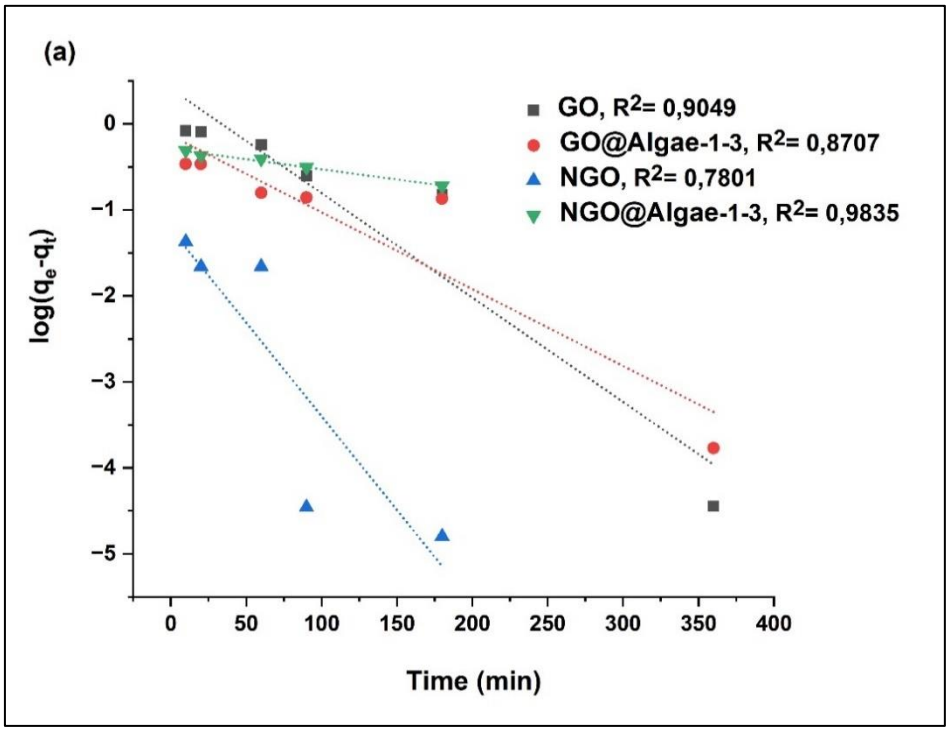
(a)
GO, R2= 0,9049
GO@Algae-1-3, R2= 0,8707
NGO, R2= 0,7801
NGO@Algae-1-3, R2= 0,9835
log(qe-qt)
Time (min)

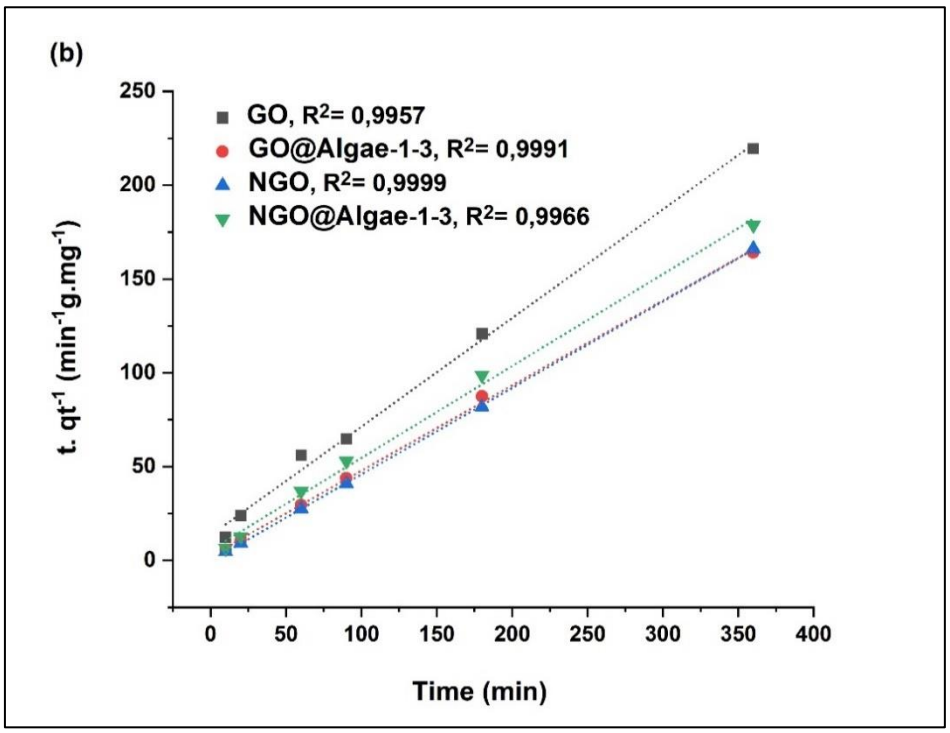
(b)
GO, R2= 0,9957
GO@Algae-1-3, R2= 0,9991
NGO, R2= 0,9999
NGO@Algae-1-3, R2= 0,9966
t. qt-1 (min-1g.mg-1)
Time (min)

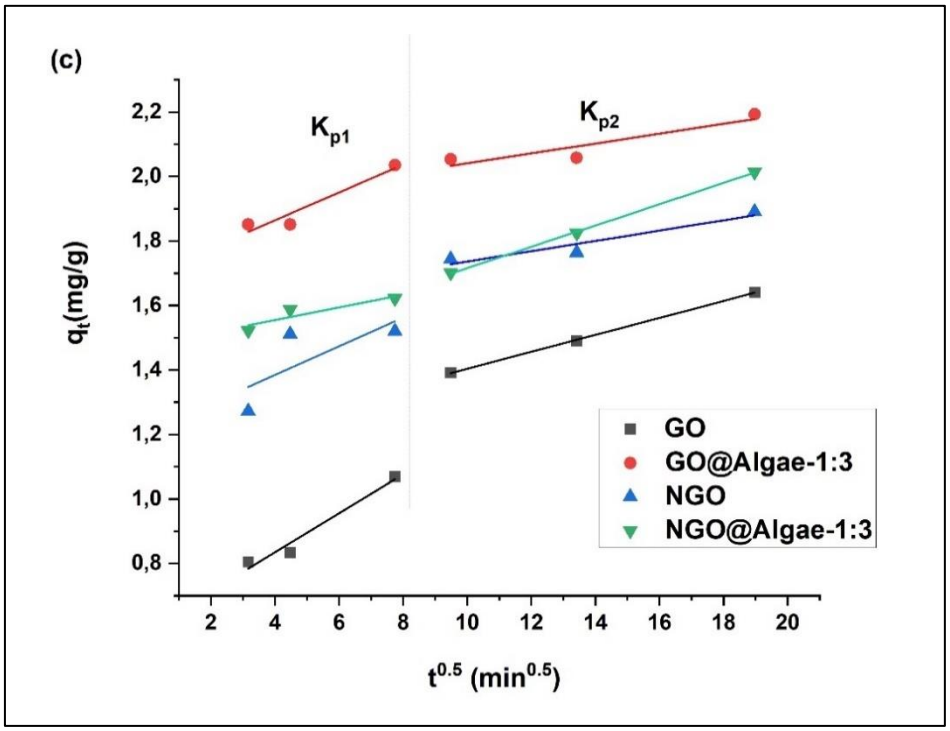

Figure 4.11: The adsorption kinetics: (a) PFO, (b) PSO, (c) intra-particle (IPD) diffusion model for Cr(VI) adsorption on GO@Algae and NGO@Algae nanocomposites (initial conc 10 mg/L; sorbent dosage 0.05 g/10 mL, pH = 2).

Table 4.3: Fitting parameters of the adsorption kinetics models for the equilibrium adsorption of Cr(VI) onto unmodified and modified GO and NGO composite.

Samples	PFO model			PSO model		
	Q_e (mg/g)	k_1 (min^{-1})	R^2	Q_e (mg/g)	k_2(mg/(g min))	R^2
GO	2.565	0.0279	0.9049	1.727	0.0249	0.9957
GO@Algae	0.737	0.0206	0.8707	2.201	0.0884	0.9991
NGO	0.186	0.0502	0.7801	2.040	0.0936	0.9999
NGO@Algae	0.509	0.0054	0.9835	2.169	0.0429	0.9966

Table 4.4: Fitting parameters of intraparticle diffusion kinetic model.

Adsorbent	Diffusion (IPD) model coefficient					
	First Stage			Second Stage		
	K_{p1}	C	R^2	K_{p2}	C	R^2
GO	0.0602	0.593	0.9676	0.0263	0.141	0.9994
GO@Algae	0.0433	1.691	0.9238	0.0153	1.888	0.9512
NGO	0.0444	1.207	0.5592	0.0159	1.577	0.9160
NGO@Algae	0.0197	1.476	0.8381	0.0330	1.386	0.9994

4.3.6 Adsorption isotherms

Adsorption isotherms are useful models that help us better understand the adsorption mechanism between the adsorbent and the adsorbate. In this work, isotherm experiments were carried out with varying initial concentrations of Cr(VI) solutions of 5, 10, 20, 50, and 80 mg/L utilizing the GO@Algae and NGO@Algae nanocomposite adsorbents. The adsorption behaviour of the adsorbents for the removal of Cr(VI) ions was investigated using Langmuir and Freundlich isotherms. From Figure 12(a) and (b) results, we can conclude that the Freundlich isotherm provides a more accurate fit to the data than the Langmuir model, as evidenced by the high values of correlation of determination (r^2 >0.96). This could be ascribed to multilayer adsorption on the heterogeneous active sites of the adsorbent (Wang et al., 2023). The values of the correlation coefficients (r^2) and isotherm constants for Cr^{6+} adsorption on nanocomposites were determined and are summarized in Table 4.5. With GO@Algae showed the best adsorption efficiency of 10.89 mg/g. The R_L values for as-prepared GO, NGO, GO@Algae, and NGO@Algae were found to be in the range of 0 to 1, indicating that Cr(VI) ion adsorption over the adsorbent was favourable (Nasreen et al., 2008). In the case of the Freundlich isotherm, the values of K_F and n were calculated, and n values were found to be greater than 1, which suggests that the adsorbents are favourable adsorbents for the removal of Cr(VI).

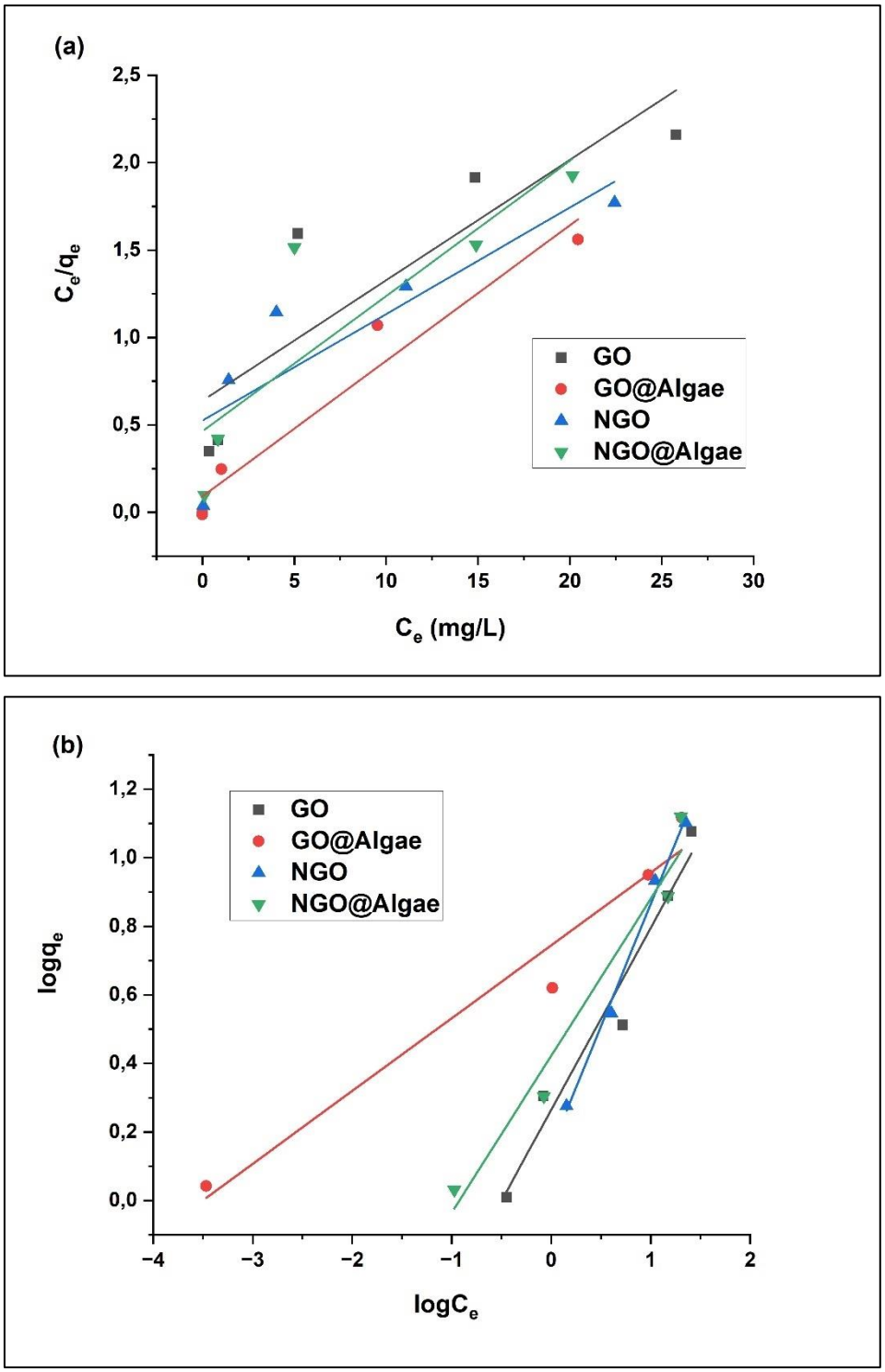

Figure 4.12: (a) Langmuir and (b) Freundlich isotherms for Cr(VI) ions adsorption on GO, NGO, GO@Algae and NGO@Algae nanohybrids (contact time: 360 min; sorbent dosage: 0.05 g/10 mL, pH = 2).

Table 4.5: The values of isotherm parameters for the removal of Cr(VI) species using GO@Algae and NGO@Algae nanocomposites

Samples	Langmuir model				Freundlich model		
	Q_{max} (mg/g)	K_L (L/mg)	R_L	R^2	K_F (L/mg)	n	R^2
GO	1.56	22.692	0.009	0.7698	1.838	1.885	0.9620
GO@Algae	10.89	140.558	0.001	0.9518	5.550	4.708	0.9611
NGO	1.90	31.259	0.006	0.7485	1.417	1.401	0.9928
NGO@Algae	1.93	27.262	0.007	0.8112	2.644	2.184	0.9667

4.3.7 XPS results

XPS analysis was used to investigate the nanoadsorbents surface chemistry properties, such as elemental composition and chemical state (Oh et al., 2013; Zhang et al., 2011). Figure 4.13A depicts the wide-scan XPS spectra of GO@Algae-1:3 and NGO@Algae-1:3, prior to and after the adsorption of Cr(VI). The spectra exhibited peaks corresponding to carbon, nitrogen, oxygen, and Cr 2p. The Gauss function was used to fit the peaks in the N 1s, C 1s, O 1s, and Cr 2p spectra.

Upon comparing the XPS spectrum of GO and NGO@Algae-based nanohybrids before and after adsorption of Cr(VI), it was evident that minor Cr-related peaks emerged after adsorption (Figure 4.13A (b and d)). This indicates that Cr(VI) has been effectively adsorbed onto the surface of the nanohybrids. Figure 4.13B illustrates the XPS spectra associated with Cr 2p. The Cr 2p spectra exhibited two main asymmetric peaks: a lower energy peak around ~577 eV corresponding to the Cr $2p_{3/2}$ state, and a higher energy peak at around 588 eV corresponding to Cr $2p_{1/2}$ (Bandara et al., 2020; Geng et al., 2022). The peaks were deconvoluted into four peaks of Cr $2p_{3/2}$ (at 579.1 eV and 588.5 eV) attributed with Cr(VI) and Cr $2p_{1/2}$ (578.1 eV and 587.6 eV), which aligns with the standard XPS profile of Cr(III) oxidation state (Lei et al., 2014). In addition, the XPS analysis indicated that a portion of Cr(VI) was converted to Cr(III) during adsorption after exposure to nanohybrids. This suggests that the redox reaction is the primarily mechanism responsible for the adsorptive removal of chromium by the nanoadsorbent (Bandara et al., 2020; Geng et al., 2022). This

conclusion is promising, as it implies that the adsorbed extremely dangerous Cr(VI) is converted into less toxic Cr(III) ions.

Figure 4.13C shows the C 1s band spectrum of GO@Algae-1:3 and NGO@Algae-1:3 after Cr(VI) adsorption. The C 1s of both nanohybrids were deconvoluted into four distinct peaks with binding energies of ~284.5, ~285.6, ~286.9, and ~289 eV, which are assigned to the C (non-oxygenated), C-O (epoxy/ether group), C=O (carbonyl carbon), and COOH (carboxylate carbon) bonds, respectively (Figure 4.13C (a and c)) (Al-Gaashani et al., 2019; Zhang et al., 2011). However, after adsorption (Figure 4.13C (b)), the intensities of the C1s peaks associated with C-C and carbon-oxygen bonds decreased as a result of the Cr(VI) ions being deposited into the GO@Algae-1:3 matrix. Whereas the deconvolution analysis of NGO@Algae-1:3 shows that the C-C bonds peak disappeared or decreased significantly after the adsorption, while that of the oxygen-related functional moieties C-O, C=O, and COOH increased (Figure 4.13C (d)). These findings indicate that the functional group played a role in the absorption of Cr(VI) (Al-Gaashani et al., 2019; Zhang et al., 2011).

The O 1s band spectra of both nanohybrids following Cr(VI) adsorption are depicted in Figure 4.13D. The O 1s spectra before adsorption can be deconvoluted into three distinct peaks representing C-O-C, C-OH (at 531.2 eV), C=O (at 530.3 eV), and -COOH (at 533.4 eV) (Figure 4.13D (a and c)). However, the peak strength of oxygen-containing moieties following adsorption differs from its initial state in both nanohybrids prior to the adsorption of Cr(VI). The strength content of the oxygen-containing functional groups, particularly COOH, C-OH, and C-OH, is reduced and shifted to a higher energy level (Figure 4.13D (b and d)). This phenomenon indicates that some of the functional groups, during adsorption, interacted with the Cr ions through ion exchange (Peng et al., 2017; Shchukarev et al., 2020). The presence of C=O in nanohybrids indicates that a portion of them underwent a transformation to C-O subsequent to the absorption of Cr(VI). This indicates that a redox reaction occurred during the adsorption process (Peng et al., 2017; Shchukarev et al., 2020). Furthermore, in the case of NGO@Algae nanohybrids, the COOH peak disappeared completely. The high-resolution spectra at N 1s for both nanohybrids has been fitted, and three distinct peaks at 398.0, 399.5, and 400.9 eV have been identified. These peaks correspond to pyridinic nitrogen (=N-C), amine/amide (-NH_2, -NH), and imine (-C-N, N^+), respectively (Figure 4.13E (a and c)) (Ayiania et al., 2020; Geng et al., 2022; Hummers and Offeman, 1958). After the adsorption of Cr(VI), there was a notable rise in the N^+ peak

intensity, whereas the intensity of =N- and -NH reduced. The findings indicate that a portion of the nitrogen-containing groups in GO@Algae and NGO@Algae nanohybrids experienced further protonation under acidic conditions, leading to a significant decrease in non-protonated nitrogen moieties (Figure 4.13E (b and d)). In addition, the deconvolution analysis of NGO@Algae-1:3 upon adsorption revealed the emergence of two additional peaks at 401.90 eV and 402.45 eV. These peaks can be ascribed to the presence of nitrogen atoms in doped imine ($=NH^+$) and NH_3^+ forms, as depicted in Figure 4.13E (d) (Lei et al., 2014). The amino groups present in the NGO@Algae-1:3 are likely responsible for both the immobilization of Cr(VI) and the formation of complexes with Cr(III) ions.

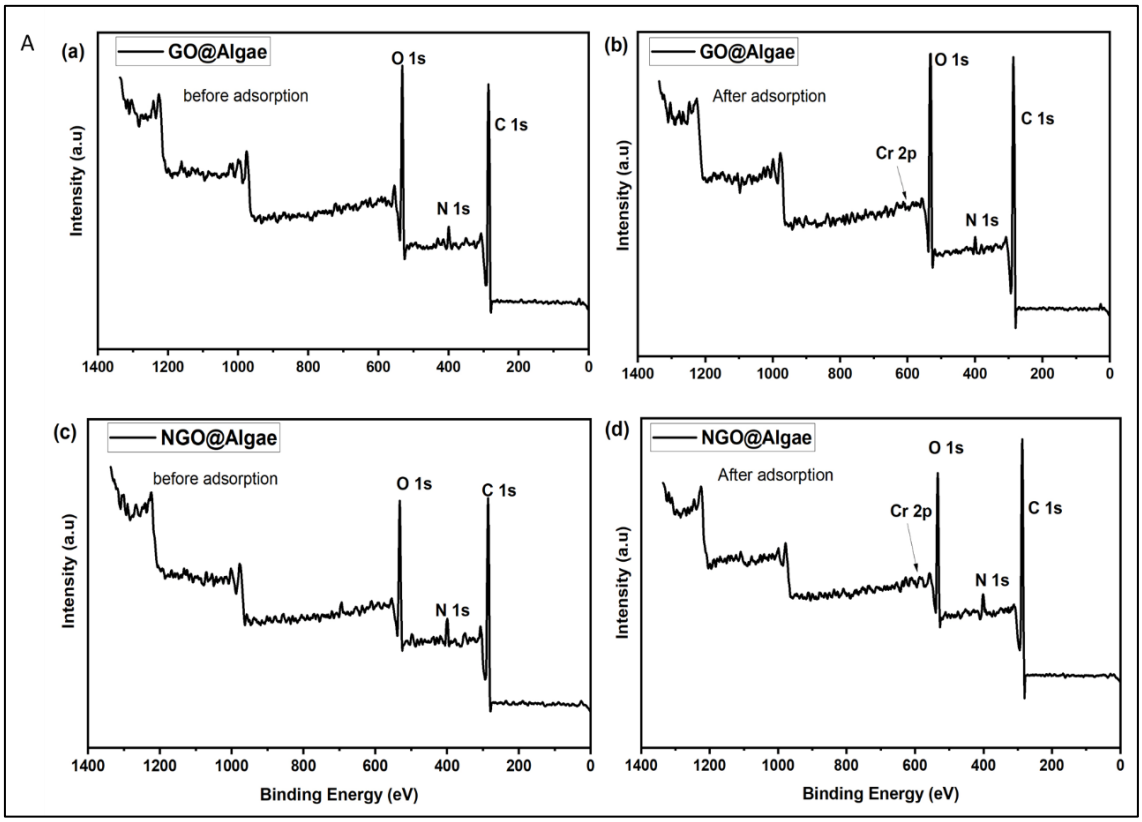

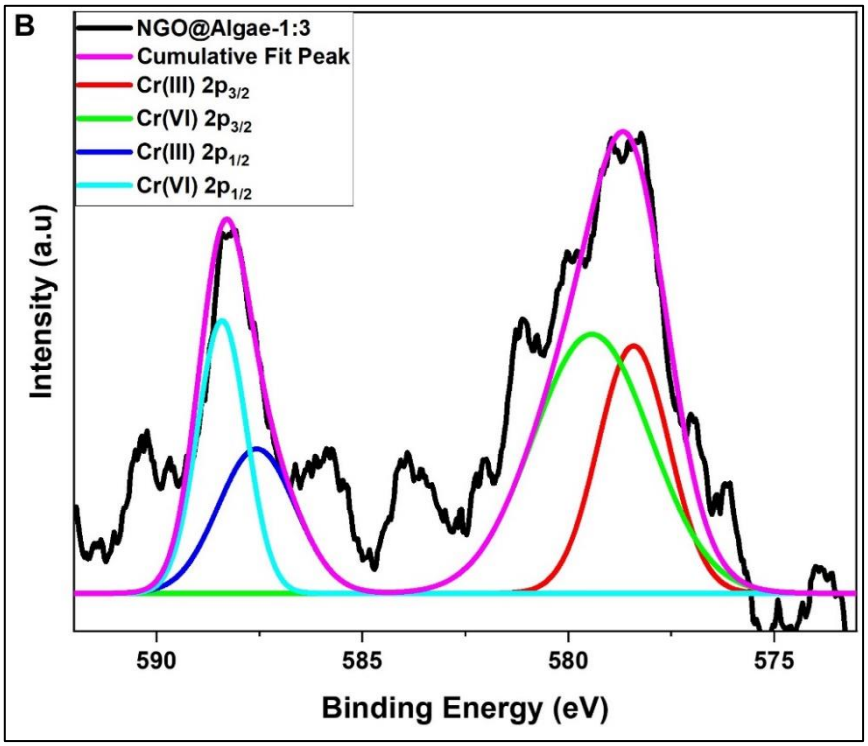
B
NGO@Algae-1:3
Cumulative Fit Peak
Cr(III) 2p3/2
Cr(VI) 2p3/2
Cr(III) 2p1/2
Cr(VI) 2p1/2
Intensity (a.u)
590
585
580
575
Binding Energy (eV)

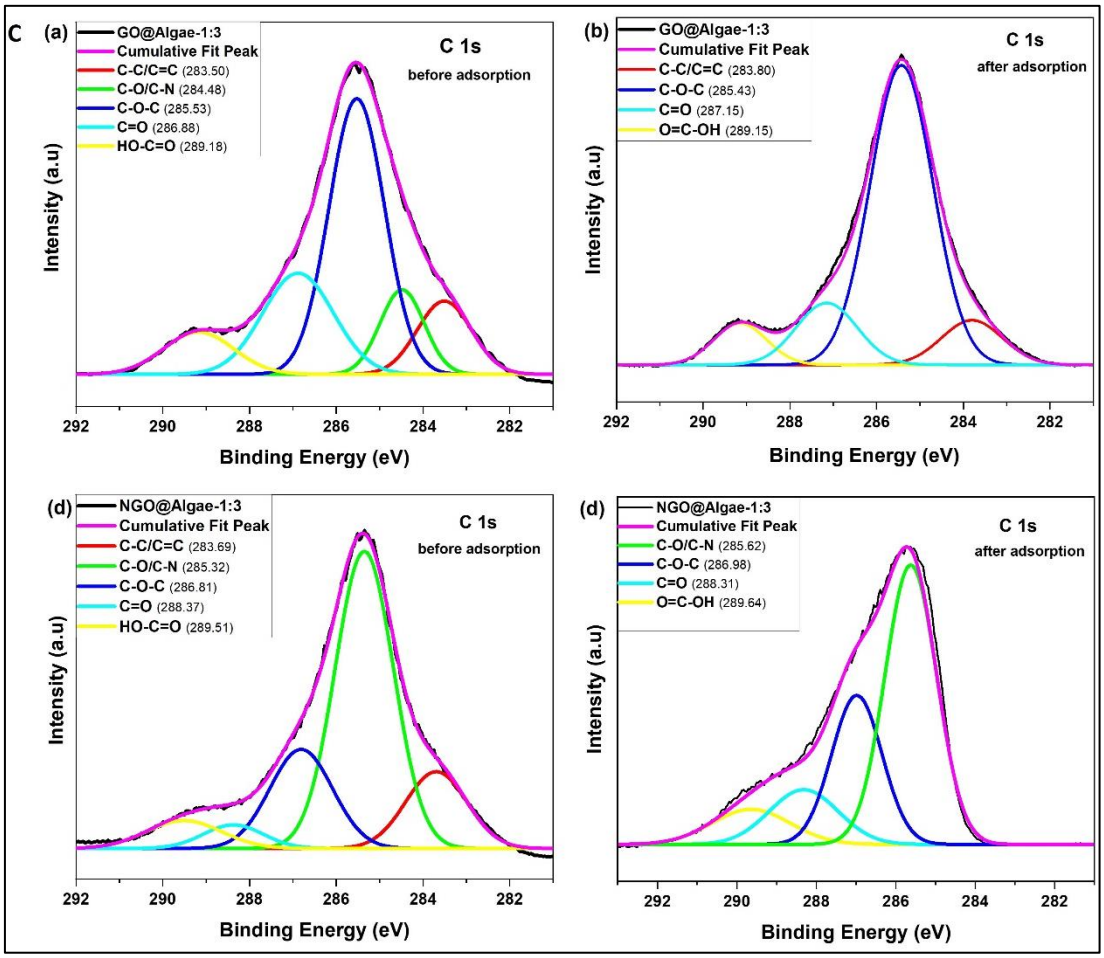
C
(a)
GO@Algae-1:3
Cumulative Fit Peak
C-C/C=C (283.50)
C-O/C-N (284.48)
C-O-C (285.53)
C=O (286.88)
HO-C=O (289.18)
C 1s
before adsorption
Intensity (a.u)
Binding Energy (eV)
(b)
GO@Algae-1:3
Cumulative Fit Peak
C-C/C=C (283.80)
C-O-C (285.43)
C=O (287.15)
O=C-OH (289.15)
C 1s
after adsorption
Intensity (a.u)
Binding Energy (eV)
(d)
NGO@Algae-1:3
Cumulative Fit Peak
C-C/C=C (283.69)
C-O/C-N (285.32)
C-O-C (286.81)
C=O (288.37)
HO-C=O (289.51)
C 1s
before adsorption
Intensity (a.u)
Binding Energy (eV)
(d)
NGO@Algae-1:3
Cumulative Fit Peak
C-O/C-N (285.62)
C-O-C (286.98)
C=O (288.31)
O=C-OH (289.64)
C 1s
after adsorption
Intensity (a.u)
Binding Energy (eV)
292
290
288
286
284
282

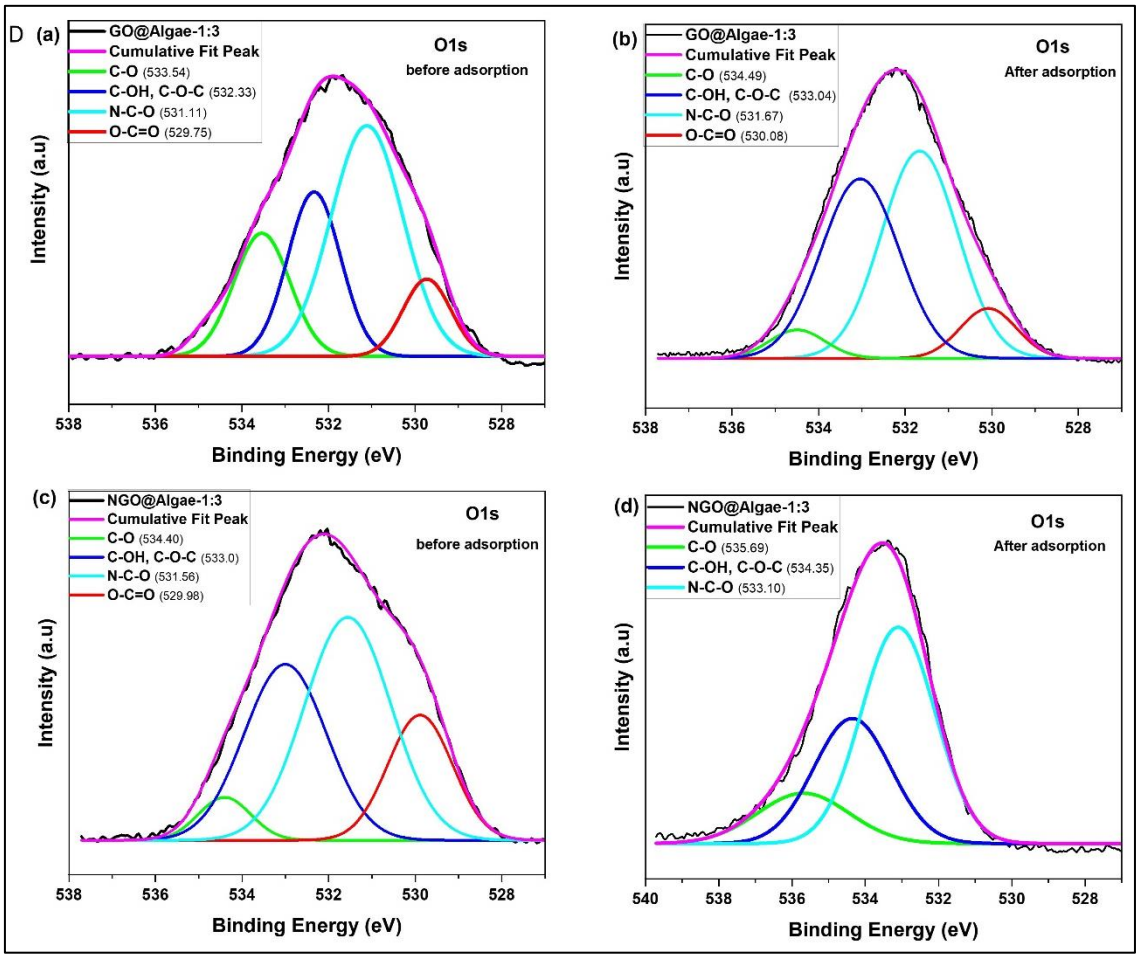
D (a)
GO@Algae-1:3
Cumulative Fit Peak
C-O (533.54)
C-OH, C-O-C (532.33)
N-C-O (531.11)
O-C=O (529.75)
O1s
before adsorption
Intensity (a.u)
Binding Energy (eV)
(b)
GO@Algae-1:3
Cumulative Fit Peak
C-O (534.49)
C-OH, C-O-C (533.04)
N-C-O (531.67)
O-C=O (530.08)
O1s
After adsorption
Intensity (a.u)
Binding Energy (eV)
(c)
NGO@Algae-1:3
Cumulative Fit Peak
C-O (534.40)
C-OH, C-O-C (533.0)
N-C-O (531.56)
O-C=O (529.98)
O1s
before adsorption
Intensity (a.u)
Binding Energy (eV)
(d)
NGO@Algae-1:3
Cumulative Fit Peak
C-O (535.69)
C-OH, C-O-C (534.35)
N-C-O (533.10)
O1s
After adsorption
Intensity (a.u)
Binding Energy (eV)

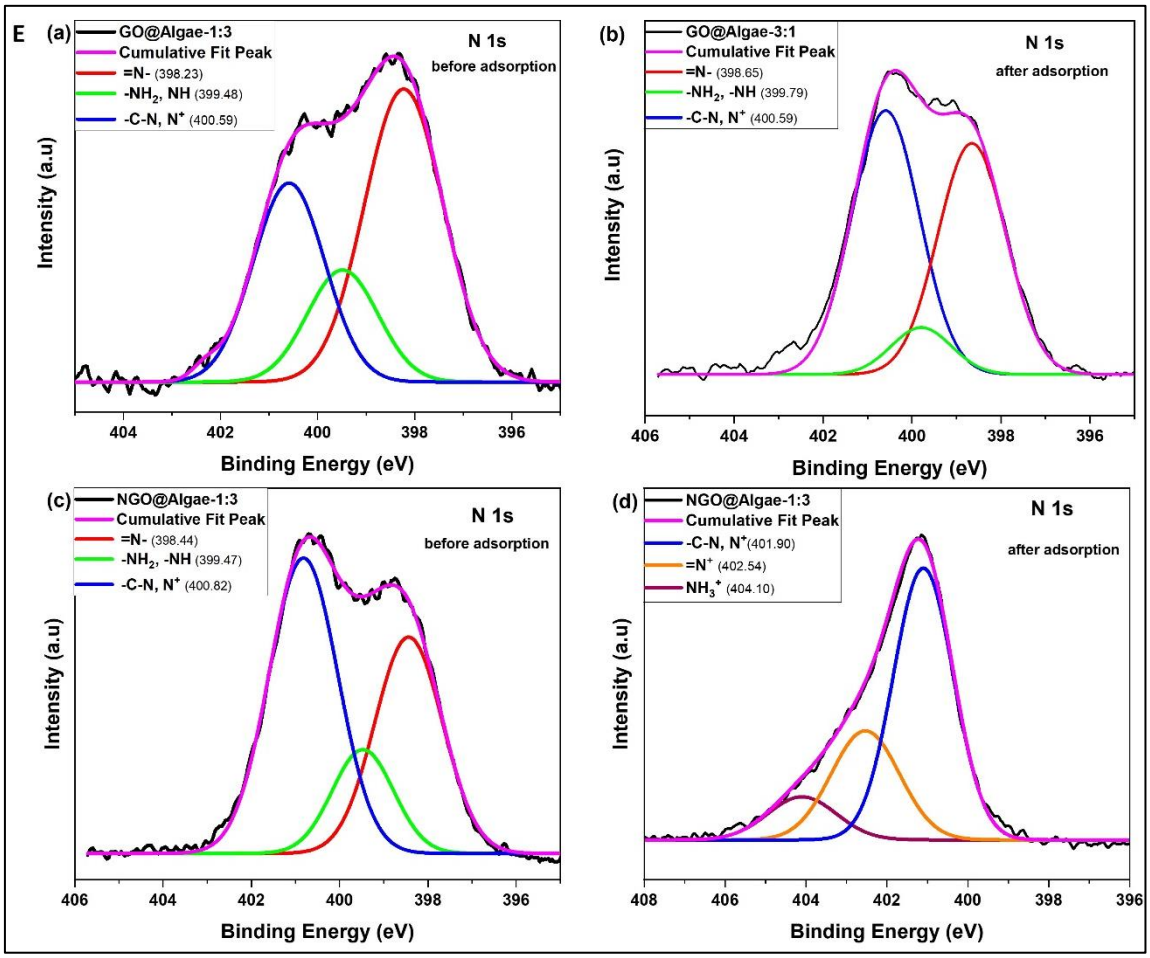

Figure 4.13: XPS spectra of GO@Algae-1:3 and NGO@Algae-1:3 before and after the Cr(VI) adsorption experiment: (A) survey wide scan, (B) XPS spectra of Cr for the NGO@Algae after adsorption, (C) C1s curve-fitting, (D) O1s curve-fitting and (E) N1s curve-fitting.

4.3.8 Adsorption mechanisms for removal of Cr(VI) by GN@microalgae-based nanomaterials

Based on the evaluated parameters, the Cr(VI) adsorption process in these GN@microalgae-based nanomaterials could occur through various mechanisms. These mechanisms include internal adsorption, where Cr(VI) ions enter the adsorbent's pores without forming a bond or interacting, as well as external accumulation within the microalgae cells and within the GO and NGO nanosheet lattices. The probable mechanisms of Cr(VI) adsorption onto the surface of nanohybrids are proposed in Figure 4.14. The graphic depicts the different interactions involved in the process of Cr(VI) adsorption, which encompass electrostatic

interactions, reduction, complexation and pore filling. So, the Cr(VI) species binds to the positively charged groups present at the surface of the nanoadsorbents through electrostatic forces (Rout et al., 2022). Simultaneously, in an acidic environment, the process of adsorption can activate mechanisms that reduce Cr(VI) to Cr(III), which are caused by the electron-donating groups on the surfaces of adsorbents, as presented by the following reaction (Rout et al., 2022 and Putra et al., 2024).

$$HCrO_4^- + 7H^+ + 3e^- \rightarrow Cr^{3+} + 4H_2O$$

Afterwards, the Cr(III) ions that are generated can be eliminated by forming coordination bonds and undergoing ion exchange with the carboxyl and amine groups on the surface of the nanohybrid (Li et al., 2020 and Putra et al., 2024). Thus, during the adsorption of Cr(VI) ions, the functional groups present in the GN@Algae-based composite surface can act both as reducing agents and as adsorption sites.

The pH result in Section 4.2.7 clearly shows that GO@Algae and NGO-Algae were able to effectively remove a significant amount of Cr (VI) ions in a highly acidic environment. This phenomenon can be explained by these mechanisms: the electrostatic attraction between the amino groups and protonated carboxyl and hydroxy groups on the surfaces of the adsorbents and $HCrO_4^-$ anions and the reduced Cr(III) cations can form a donor-acceptor bond with the amine, hydroxyl and carboxyl groups as illustrated by Figure 4.14. While the removal efficiency of Cr(VI) ions in the pH > pH_{zpc} region can be explained by the electrostatic repulsion between the negatively charged surface of the adsorbents and Cr(VI) anions.

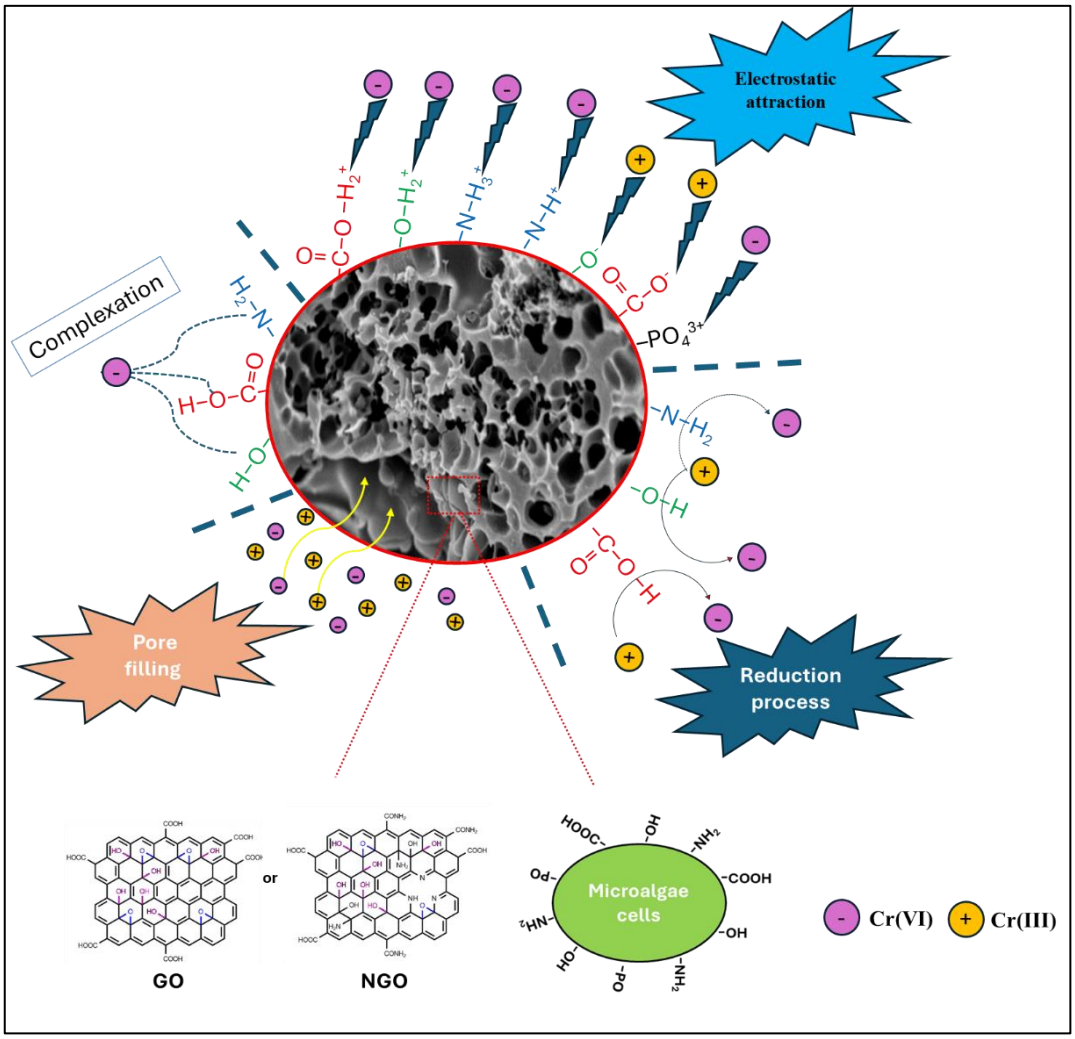

Figure 4.14: The schematic illustration for the proposed adsorption mechanism of Cr(VI) through GN@microalgae-based nanomaterials.

CHAPTER 5
GENERAL CONCLUSIONS AND RECOMMENDATIONS

5.1 General conclusions

The goal of this project was to study the interaction of Cr(VI) heavy metal adsorption on the surface of newly synthesized GO@microalgae and NGO@microalgae-based materials for adsorption applications. Graphene oxide@microalgae-based nanohybrid structures were obtained by the self-assembly of GO or NGO with microalgae using the ultrasonication technique, as mentioned in Chapter 3. This study has demonstrated the successful functionalization of GO and N-doped graphene oxide utilizing microalgae.

- ✓ SEM images revealed a rough surface morphology of the nanocomposite. TGA, FTIR and XPS results confirmed the presence of functional groups.
- ✓ Despite the successful incorporation of algae into the GO and NGO matrices, the specific surface area of GO@microalgae and NGO@microalgae-based nanohybrids such as GO@microalgae-1:3 and NGO@microalgae-1:3 was reduced. However, the results showed that nanostructured composites exhibited improved adsorption removal and capacity for Cr(VI) species as a result of the increased available binding sites on their surface compared to the bare GO nanomaterial.
- ✓ The zeta potential analysis revealed that the point of zero charge (pH_{pzc}) was determined to be 2.03. This indicates that the adsorbent had a negative charge when the pH was above 2.03. As a result, there was an increase in the adsorption of Cr^{6+} ions at pH below the pH PZC point as a consequence of electrostatic interactions between the positively charged adsorbent binding sites and the negatively charged Cr^{6+} species.

Batch adsorption studies were carried out in the removal of Cr(VI) from an aqueous solution, and these included the effects of pH, adsorbent mass, contact time, and lastly, initial ion concentration.

- ✓ The adsorption of Cr(VI) ions on GO@microalgae and NGO@microalgae depended on the pH level. At pH 2, where $HCrO_4^-$ species were predominant, up to 99% of the

ions were removed. The efficacy of Cr(VI) removal improved as the amount of adsorbent used increased. This suggests that the specific surface area affected the adsorption process.

- ✓ Upon evaluating different adsorption isotherm models, it was found that the experimental data exhibited the highest level of agreement with the Freundlich isotherm model. This indicates that the Cr(VI) species were adsorbed in multiple layers.
- ✓ The maximal adsorption capacity of the GO@microalgae-based composites was determined to be 10.89 mg/g, surpassing the values achieved with other adsorbents as discussed in Chapter 4.
- ✓ For the kinetic studies, the PSO model was found to be the most suitable for the adsorption process. According to the intra-particle diffusion model, the adsorption of Cr^{6+} ions occurred in two distinct stages, which indicates their multilinearity.

Furthermore, the use of unmodified GO nanosheets were shown to be ineffective for eliminating Cr ions, while NGO, GO@microalgae, and NGO@microalgae nanostructured adsorbents perform better due to their enhanced surface chemistry and structural properties. The study indicates that electrostatic interactions play a primary role in the adsorption mechanism for the removal of Cr(VI) by GO@microalgae and NGO@microalgae composites, aligning with comparable studies. Overall, this study showed that GO@microalgae and NGO@microalgae nanohybrids are efficient in eliminating heavy metals from water solutions.

5.2 Recommendations for further work

Although this work may be deemed successful, there is still ample opportunity for further investigation. Several suggestions for future investigation include:

- To determine the effect of temperature on adsorption removal and capacity as it affects the rate and extent of adsorption.
- To carrier out the recovery and reusability of the graphene@microalgae-based

nanohybrid through adsorption/desorption studies (energy or photocatalytic applications).

- To carry out the stability studies in adsorption is crucial because they determine the longevity and reliability of adsorbents over time.
- More studies are required to determine the selectivity of the graphene@microalgea-based nanohybrid towards other heavy metals like Cu(II), Hg(II), Pb(II), and Zn(II), as well as organic pollutants in order to optimize these nanohybrids for targeted applications.

Further research is warranted to discover additional cost-effective nanoadsorbents that are capable of efficiently eliminating heavy metals. Moreover, it is crucial to assess the effectiveness of these nanomaterials in real water sources, such as industrial waste, rivers and lakes, and household sewage, by conducting lab bench-scale and pilot testing.

5.3 References

Abdelfattah, A., Ali, S.S., Ramadan, H., El-Aswar, E.I., Eltawab, R., Ho, S.H., Elsamahy, T., Li, S., El-Sheekh, M.M., Schagerl, M., Kornaros, M., Sun, J., 2023. Microalgae-based wastewater treatment: Mechanisms, challenges, recent advances, and future prospects. Environmental Science and Ecotechnology, 13, 100205.

Abiodun, O.A.O., Oluwaseun, O., Oladayo, O.K., Abayomi, O., George, A.A., Opatola, E., Orah, R.F., Isukuru, E.J., Ede, I.C., Oluwayomi, O.T., Okolie, J.A., Omotayo, I.A., 2023. Remediation of heavy metals using biomass-based adsorbents: Adsorption Kinetics and Isotherm Models. Clean Technologies, 5, 934–960.

Ahmadzadeh T.M., Mohammadi, T., 2012. Nitrate removal from water using functionalized carbon nanotube sheets. Chemical Engineering Research and Design, 90, 1815–1822.

Akhter, F., Zoppas, F.M., Soomro, M., Jatoi, A.S., Noureen, F., Akhtar, M.N., Mehreen, F., 2023. Carbon-based sorbets for heavy metal removal from aqueous solution, discrepancies, and future prospects: a state-of-the-art review. Biomass Convers Biorefin, 13, 10343–10359.

Al-Gaashani, R., Najjar, A., Zakaria, Y., Mansour, S., Atieh, M.A., 2019. XPS and structural studies of high-quality graphene oxide and reduced graphene oxide prepared by different chemical oxidation methods. Ceramics International, 45, 14439–14448.

Al-Homaidan, A.A., Al-Qahtani, H.S., Al-Ghanayem, A.A., Ameen, F., Ibraheem, I.B.M., 2018. Potential use of green algae as a biosorbent for hexavalent chromium removal from aqueous solutions. Saudi Journal of Biological Sciences, 25, 1733–1738.

Ali, M.E., Das, R., Maamor, A., Hamid, S.B.A., 2014. Multifunctional carbon nanotubes (CNTs): A new dimension in environmental remediation: Advanced Materials Research, 832, 328–332.

Almutairi, F.M., El Rabey, H.A., Alalawy, A.I., Salama, A.A.M., Tayel, A.A., Mohammed, G.M., Aljohani, M.M., Keshk, A.A., Abbas, N.H., Zayed, M.M., 2021. Application of chitosan/alginate nanocomposite incorporated with phycosynthesized iron nanoparticles for efficient remediation of chromium. Polymers, 13, 248.

Alsaiari, N.S., Amari, A., Katubi, K.M., Alzahrani, F.M., Rebah, F. Ben, Tahoon, M.A., 2022. The synthesis of magnetic nitrogen-doped graphene oxide nanocomposite for the removal of reactive orange 12 dye. Adsorption Science and Technology, 2022, 1–14.

Alves, J.L.F., da Silva, J.G.C., Costa, R.L., dos Santos S.F.J., da Silva V.F.F., Moreira, R.D.F.P.M., José, H.J., 2019. Investigation of the bioenergy potential of microalgae Scenedesmus acuminatus by physicochemical characterization and kinetic analysis of pyrolysis. Journal of Thermal Analysis and Calorimetry, 135, 3269–3280.

Anfar, Z., Ait Ahsaine, H., Zbair, M., Amedlous, A., Ait El Fakir, A., Jada, A., El Alem, N., 2020. Recent trends on numerical investigations of response surface methodology for pollutants adsorption onto activated carbon materials: A review. Critical Reviews in Environmental Science and Technology, 50, 1043–1084.

Arica, M.Y., Tüzün, I., Yalçin, E., Ince, Ö., Bayramoğlu, G., 2005. Utilisation of native, heat and acid-treated microalgae Chlamydomonas reinhardtii preparations for biosorption of Cr(VI) ions. Process Biochemistry, 40, 2351–2358.

Ata, A., Nalcaci, O.O., Ovez, B., 2012. Macro algae Gracilaria verrucosa as a biosorbent: A study of sorption mechanisms. Algal Research, 1, 194–204.

Ayiania, M., Smith, M., Hensley, A.J.R., Scudiero, L., McEwen, J.S., Garcia-Perez, M., 2020. Deconvoluting the XPS spectra for nitrogen-doped chars: An analysis from first principles. Carbon, 162, 528–544.

Baby, R., Saifullah, B., Hussein, M.Z., 2019. Carbon nanomaterials for the treatment of heavy metal-contaminated water and environmental remediation. Nanoscale research letters, 14, 1–17.

Bandara, P.C., Peña-Bahamonde, J., Rodrigues, D.F., 2020. Redox mechanisms of conversion of Cr(VI) to Cr(III) by graphene oxide-polymer composite. Scientific reports, 10, 9237.

Brito, C.H.V., Gloria, D.C.S., Santos, E.B., Domingues, R.A., Valente, G.T., Vieira, N.C.S., Gonçalves, M., 2023. Porous activated carbon/graphene oxide composite for efficient adsorption of pharmaceutical contaminants. Chemical Engineering Research and Design, 191, 387–400.

Chang, Y.S., Chen, F.K., Tsai, D.C., Kuo, B.H., Shieu, F.S., 2021. N-doped reduced graphene oxide for room-temperature NO gas sensors. Scientific Reports, 11, 20719.

Chugh, M., Kumar, L., Shah, M.P., Bharadvaja, N., 2022. Algal Bioremediation of heavy metals: An insight into removal mechanisms, recovery of by-products, challenges, and future opportunities. Energy Nexus, 100129.

Coetzee, J.J., Bansal, N., Chirwa, E.M.N., 2020. Chromium in environment, its toxic effect from chromite-mining and ferrochrome industries, and its possible bioremediation. expo health, 12, 51–62.

Daneshvar, E., Zarrinmehr, M.J., Kousha, M., Hashtjin, A.M., Saratale, G.D., Maiti, A., Vithanage, M., Bhatnagar, A., 2019. Hexavalent chromium removal from water by microalgal-based materials: Adsorption, desorption and recovery studies. Bioresource technology, 293, 122064.

De Beni, E., Giurlani, W., Fabbri, L., Emanuele, R., Santini, S., Sarti, C., Martellini, T., Piciollo, E., Cincinelli, A., Innocenti, M., 2022. Graphene-based nanomaterials in the electroplating industry: A suitable choice for heavy metal removal from wastewater. Chemosphere, 292, 133448.

Esmaili, Z., Barikbin, B., Shams, M., Alidadi, H., Al-Musawi, T.J., Bonyadi, Z., 2023. Biosorption of metronidazole using Spirulina platensis microalgae: process modeling, kinetic, thermodynamic, and isotherm studies. Applied Water Science, 13, 63.

Geng, J., Liang, Q., Yu, W., Chen, W., Lu, G., Luo, H., 2022. Enhanced removal of Cr(VI) from aqueous solutions by polymer-mediated nitrogen-rich reduced graphene oxide. Journal of Hazardous Materials, 436, 129184.

Gholami, A., Emadi, F., Amini, A., Shokripour, M., Chashmpoosh, M., Omidifar, N., 2020. Functionalization of graphene oxide nanosheets can reduce their cytotoxicity to dental pulp stem cells. Journal of Nanomaterials, 2020, 1–14.

Gokhale, S. V., Jyoti, K.K., Lele, S.S., 2009. Modeling of chromium (VI) biosorption by immobilized Spirulina platensis in packed column. Journal of Hazardous Materials, 170, 735–743.

Gunasundari, E., Kumar, P.S., 2017. Higher adsorption capacity of Spirulina platensis alga for Cr(VI) ions removal: Parameter optimisation, equilibrium, kinetic and thermodynamic predictions. IET nanobiotechnology, 11, 317–328.

Gusain, R., Kumar, N., Ray, S.S., 2020. Recent advances in carbon nanomaterial-based adsorbents for water purification. Coordination Chemistry Reviews, 405, 213111.

Hosseini, S.A., Talebipour, S., Neyestani, M.R., Ranjan, S., Dasgupta, N., 2018. Graphene oxide $MgFe_2O_4$ nanocomposites for Cr(VI) remediation: a comparative modeling study. Nanotechnology for Environmental Engineering, 3, 1–11.

Hummers, W.S., Offeman, R.E., 1958. Simultaneous nitrogen-doping and reduction of graphene oxide. Journal of the American Chemical Society, 80, 1339.

Huo, B., Jiang, D., Cao, X., Liang, H., Liu, Z., Li, C., Liu, J., 2019. N-doped graphene /carbon hybrid aerogels for efficient solar steam generation. Carbon N Y 142, 13–19.

Husien, S., Labena, A., El-Belely, E.F., Mahmoud, H.M., Hamouda, A.S., 2019. Adsorption studies of hexavalent chromium [Cr (VI)] on micro-scale biomass of Sargassum dentifolium, Seaweed. Journal of Environmental Chemical Engineering, 7, 103444.

Hussain, N., Bilal, M., M. N. Iqbal, H., 2021. Carbon-based nanomaterials with multipurpose attributes for water treatment: Greening the 21st-century nanostructure materials deployment. Biomaterials and Polymers Horizon, 1, 48–58.

Johra, F.T., Lee, J.W., Jung, W.G., 2014. Facile and safe graphene preparation on solution-based platform. Journal of Industrial and Engineering Chemistry, 20, 2883–2887.

Jung, C., Heo, J., Han, J., Her, N., Lee, S.J., Oh, J., Ryu, J., Yoon, Y., 2013. Hexavalent chromium removal by various adsorbents: Powdered activated carbon, chitosan, and single/multi-walled carbon nanotubes. Separation and purification technology, 106, 63–71.

Kim, N., Cha, B., Yea, Y., Njaramba, L.K., Vigneshwaran, S., Elanchezhiyan, S.S., Park, C.M., 2022. Effective sequestration of tetracycline and ciprofloxacin from aqueous solutions by Al-based metal organic framework and reduced graphene oxide immobilized alginate biosorbents. Chemical Engineering Journal, 450, 138068. .

Kota, M., Yu, X., Yeon, S.H., Cheong, H.W., Park, H.S., 2016. Ice-templated three dimensional nitrogen doped graphene for enhanced supercapacitor performance. Journal of Power Sources, 303, 372–378.

Khan, A., Alamry, K.A., 2022. Surface modified carbon nanotubes: An introduction. Volume 1: Fundamentals, synthesis and recent trends. American Chemical Society, 1–25.

Kumar, K.J., Ramaswamy, A.P., Peera, G.S., 2017. Green synthesis of n-graphene by hydrothermal-microwave irradiation for alkaline fuel cell application. International Journal of Recent Scientific Research, 8, 19049-19053.

Kumar, N., Setshedi, K., Masukume, M., Ray, S.S., 2022. Facile scalable synthesis of graphene oxide and reduced graphene oxide: comparative investigation of different reduction methods. Carbon Letters, 32, 1031–1046.

Kumar, R., Rauwel, P., Rauwel, E., 2021. Nanoadsorbants for the removal of heavy metals from contaminated water: Current scenario and future directions. Processes, 9, 1379.

Lei, Y., Chen, F., Luo, Y., Zhang, L., 2014. Three-dimensional magnetic graphene oxide foam/Fe_3O_4 nanocomposite as an efficient absorbent for Cr(VI) removal. Journal of Materials Science, 49, 4236–4245.

Li, P., Hu, M., Suo, J., Xie, Y., Hu, W., Wang, X., Wang, Y. and Zhang, Y., 2020. Enhanced Cr (VI) removal by waste biomass derived nitrogen/oxygen co-doped microporous biocarbon. Environmental Science and Pollution Research, 27, 5433–5445.

Lian, Q., Ahmad, Z.U., Gang, D.D., Zappi, M.E., Fortela, D.L.B., Hernandez, R., 2020. The effects of carbon disulfide driven functionalization on graphene oxide for enhanced Pb(II) adsorption: Investigation of adsorption mechanism. Chemosphere, 248, 126078.

Liang, Q., Luo, H., Geng, J., Chen, J., 2018. Facile one-pot preparation of nitrogen-doped ultra-light graphene oxide aerogel and its prominent adsorption performance of Cr(VI). Chemical Engineering Journal, 338, 62–71.

Lingamdinne, L.P., Kim, I.S., Ha, J.H., Chang, Y.Y., Koduru, J.R., Yang, J.K., 2017. Enhanced adsorption removal of Pb(II) and Cr(III) by using nickel ferrite-reduced graphene oxide nanocomposite. Metals, 7, 225.

Lu, Y., Zhang, F., Zhang, T., Leng, K., Zhang, L., Yang, X., Ma, Y., Huang, Y., Zhang, M., Chen, Y., 2013. Synthesis and supercapacitor performance studies of N-doped graphene materials using o-phenylenediamine as the double-N precursor. Carbon, 63, 508–516.

Lyubchik, S., Lyubchik, A., Lygina, O., n.d. Comparison of the thermodynamic parameters estimation for the adsorption process of the metals from liquid phase on activated carbons. In Thermodynamics-Interaction Studies-Solids, Liquids and Gases. IntechOpen, 2011.

Mabhaudhi, T., Nhamo, L., Mpandeli, S., Nhemachena, C., Senzanje, A., Sobratee, N., Chivenge, P.P., Slotow, R., Naidoo, D., Liphadzi, S., Modi, A.T., 2019. The water–energy–food nexus as a tool to transform rural livelihoods and well-being in Southern Africa. International journal of environmental research and public health, 16, 2970.

Madima, N., Mishra, S.B., Inamuddin, I., Mishra, A.K., 2020. Carbon-based nanomaterials for remediation of organic and inorganic pollutants from wastewater. A review. Environmental Chemistry Letters, 18, 1169–1191.

Matebese, F., Moutloali, R.M., 2022. Integrating ultrafiltration membranes with flocculation and activated carbon pretreatment processes for membrane fouling mitigation and metal ion removal from wastewater. ACS Omega, 8, 9074–9085

McNeill, L., McLean, J., Edwards, M., Parks, J., 2012. State of the science of hexavalent chromium in drinking water. Water Research Foundation, 6666, 1–35.

Nasreen, A., Muhammad, I., Saeed Iqbal, Z., Javed, I., 2008. Biosorption characteristics of unicellular green alga Chlorella sorokiniana immobilized in loofa sponge for removal of Cr(III), Journal of Environmental Sciences, 20, 231–239.

Nasrollahzadeh, M., Sajjadi, M., Iravani, S., Varma, R.S., 2021. Carbon-based sustainable nanomaterials for water treatment: State-of-art and future perspectives. Chemosphere, 263, 128005.

Nithya, K., Sathish, A., Pradeep, K., Kiran Baalaji, S., 2019. Algal biomass waste residues of Spirulina platensis for chromium adsorption and modeling studies. Journal of Environmental Chemical Engineering, 7, 103273.

Oh, D.X., Shin, S., Lim, C., Hwang, D.S., 2013. Dopamine-mediated sclerotization of regenerated chitin in ionic liquid. Materials, 6, 3826–3839.

Oliveira, A.E.F., Braga, G.B., Tarley, C.R.T., Pereira, A.C., 2018. Thermally reduced graphene oxide: synthesis, studies and characterization. Journal of Materials Science, 53, 12005–12015.

Oliveira, A.R., Correia, A.A., Rasteiro, M.G., 2021. Heavy metals removal from aqueous solutions by multiwall carbon nanotubes: Effect of MWCNTs dispersion. Nanomaterials, 11, 2082.

Ova, D., Övez, B., 2013. Characterization of heavy metal biosorption from aqueous solutions with Nitzschia closterium biomass. Journal of Selcuk University Natural and Applied Science, 2, 96–107.

Padmavathy, K.S., Madhu, G., Haseena, P.V., 2016. A study on effects of pH, adsorbent dosage, time, initial concentration and adsorption isotherm study for the removal of

hexavalent chromium (Cr (VI)) from wastewater by magnetite nanoparticles. Procedia Technology, 24, 585–594.

Peña-Castro, J.M., Martínez-Jerónimo, F., Esparza-García, F., Cañizares-Villanueva, R.O., 2004. Heavy metals removal by the microalga Scenedesmus incrassatulus in continuous cultures. Bioresource Technology, 94, 219–222.

Peng, B., Xu, Y., Liu, K., Wang, X., Mulder, F.M., 2017. High-performance and low-cost sodium-ion anode based on a facile black phosphorus−carbon nanocomposite. ChemElectroChem, 4, 2140–2144.

Piekarski, J., Ignatowicz, K., Dąbrowski, T., 2022. Application of an adsorption process on selected materials, including waste, as a barrier to the pesticide penetration into the environment. Materials, 15, 4680.

Pillay, K., Cukrowska, E.M., Coville, N.J., 2009. Multi-walled carbon nanotubes as adsorbents for the removal of parts per billion levels of hexavalent chromium from aqueous solution. Journal of hazardous materials, 166, 1067–1075.

Pradhan, B., Bhuyan, P.P., Nayak, R., Patra, S., Behera, C., Ki, J.S., Ragusa, A., Lukatkin, A.S., Jena, M., 2022. microalgal phycoremediation: a glimpse into a sustainable environment. Toxics, 10, 525.

Pradhan, D., Sukla, L.B., Mishra, B.B., Devi, N., 2019. Biosorption for removal of hexavalent chromium using microalgae Scenedesmus sp. Journal of Cleaner Production, 209, 617–629.

Priya, A.K., Jalil, A.A., Vadivel, S., Dutta, K., Rajendran, S., Fujii, M., Soto-Moscoso, M., 2022. Heavy metal remediation from wastewater using microalgae: Recent advances and future trends. Chemosphere, 305, 135375

Putra, A., Fauzia, S., Deswati, D., Arief, S. and Zein, R., 2024. The potential of duck egg white as a modifier for activated rice straw to enhance Cr (VI) ions adsorption in an aqueous solution. South African Journal of Chemical Engineering, 48, 204–213.

Raji, Z., Karim, A., Karam, A., Khalloufi, S., 2023. Adsorption of heavy metals: mechanisms, kinetics, and applications of various adsorbents in wastewater remediation—A review. In Waste MDPI, 1, 775–805.

Rangabhashiyam, S., Balasubramanian, P., 2019. Characteristics, performances, equilibrium and kinetic modeling aspects of heavy metal removal using algae. Bioresource technology reports, 5, 261–279.

Rao, G.P., Lu, C., Su, F., 2007. Sorption of divalent metal ions from aqueous solution by carbon nanotubes: A review. Separation and purification technology, 58, 224–231.

Rout, D.R. and Jena, H.M., 2022. Batch and continuous studies on adsorptive removal of hexavalent chromium [Cr(VI)] using reduced graphene oxide. Journal of the Chinese Chemical Society, 69, 1779–1793.

Sabzehmeidani, M.M., Mahnaee, S., Ghaedi, M., Heidari, H., Roy, V.A.L., 2021. Carbon based materials: A review of adsorbents for inorganic and organic compounds. Materials Advances, 2, 598–627.

Setshedi, K.Z., Bhaumik, M., Onyango, M.S., Maity, A., 2015. High-performance towards Cr(VI) removal using multi-active sites of polypyrrole-graphene oxide nanocomposites: Batch and column studies. Chemical Engineering Journal, 262, 921–931.

Sharma, Y., Kumar, V., Sharma, M.M., 2011. Water: an essential nutrient for life; aesthetic quality of drinking water: appearance, taste, and odors. International Journal of Science Technology & Management, 2, 48–54.

Shchukarev, A., Gojkovic, Z., Funk, C., Ramstedt, M., 2020. Cryo-XPS analysis reveals surface composition of microalgae. Applied Surface Science, 526, 146538.

Shimizu, M., Tsushima, Y., Arai, S., 2017. Electrochemical Na-insertion/extraction property of Ni-coated black phosphorus prepared by an electroless deposition method. ACS Omega, 2, 4306–4315.

Shokri R.K., Mirghaffari, N., Farhadian, O., 2015. Removal of three and hexavalent chromium from aqueous solutions using a microalgae biomass-derived biosorbent. Environmental Progress & Sustainable Energy, 34, 949–956.

Sibi, G., 2016. Biosorption of chromium from electroplating and galvanizing industrial effluents under extreme conditions using Chlorella vulgaris. Green Energy and Environment, 1, 172–177.

Singh, S., Anil, A.G., Khasnabis, S., Kumar, Vijay, Nath, B., Adiga, V., Kumar Naik, T.S.S., Subramanian, S., Kumar, Vineet, Singh, J., Ramamurthy, P.C., 2022a. Sustainable removal of Cr(VI) using graphene oxide-zinc oxide nanohybrid: Adsorption kinetics, isotherms and thermodynamics. Environmental Research, 203, 111891.

Singh, S., Naik, T.S.S.K., Anil, A.G., Khasnabis, S., Nath, B., U, B., Kumar, V., Garg, V.K., Subramanian, S., Singh, J., Ramamurthy, P.C., 2022b. A novel CaO nanocomposite cross linked graphene oxide for Cr(VI) removal and sensing from wastewater. Chemosphere, 301, 134714.

Song, T., Tian, W., Qiao, K., Zhao, J., Chu, M., Du, Z., Wang, L., Xie, W., 2021. Adsorption behaviors of polycyclic aromatic hydrocarbons and oxygen derivatives in wastewater on N-doped reduced graphene oxide. Separation and Purification Technology, 254, 117565.

Stafiej, A., Pyrzynska, K., 2007. Adsorption of heavy metal ions with carbon nanotubes. Separation and Purification Technology, 58, 49–52.

Stylianou, S.K., Szymanska, K., Katsoyiannis, I.A., Zouboulis, A.I., 2015. Novel water treatment processes based on hybrid membrane-ozonation systems: A novel ceramic membrane contactor for bubbleless ozonation of emerging micropollutants. Journal of Chemistry, 2015.

Subedi, N., Lähde, A., Abu-Danso, E., Iqbal, J., Bhatnagar, A., 2019. A comparative study of magnetic chitosan (Chi@Fe_3O_4) and graphene oxide modified magnetic chitosan (Chi@Fe_3O_4GO) nanocomposites for efficient removal of Cr(VI) from water. International journal of biological macromolecules, 137, 948–959.

Suresh Kumar, K., Dahms, H.U., Won, E.J., Lee, J.S., Shin, K.H., 2015. Microalgae - A promising tool for heavy metal remediation. Ecotoxicology and environmental safety, 113, 329–352.

Tadjenant, Y., Dokhan, N., Barras, A., Addad, A., Jijie, R., Szunerits, S., Boukherroub, R., 2020. Graphene oxide chemically reduced and functionalized with KOH-PEI for efficient Cr(VI) adsorption and reduction in acidic medium. Chemosphere, 258, 127316.

Tofighy, M.A., Mohammadi, T., 2011. Adsorption of divalent heavy metal ions from water using carbon nanotube sheets. Journal of hazardous materials, 185, 140–147.

Wang, B., Lan, J., Bo, C., Gong, B., Ou, J., 2023. Adsorption of heavy metal onto biomass-derived activated carbon: review. RSC advances, 13, 4275–4302

Wang, H., Yuan, X., Wu, Y., Chen, X., Leng, L., Wang, H., Li, H. and Zeng, G., 2015. Facile synthesis of polypyrrole decorated reduced graphene oxide–Fe3O4 magnetic composites and its application for the Cr (VI) removal. *Chemical Engineering Journal*, *262*, pp.597-606.

Wang, Z., Xia, L., Song, S., Farías, M.E., Li, Y., Tang, C., 2021. Cadmium removal from diluted wastewater by using high-phosphorus-culture modified microalgae. Chemical Physics Letters, 771, 138561.

Xu, X., Zeng, J., Wu, Y., Wang, Q., Wu, S., Gu, H., 2022. Preparation and application of graphene–based materials for heavy metal removal in tobacco industry: A Review. Separations, 9, 401.

Yang, X., Wan, Y., Zheng, Y., He, F., Yu, Z., Huang, J., Wang, H., Ok, Y.S., Jiang, Y., Gao, B., 2019. Surface functional groups of carbon-based adsorbents and their roles in the removal of heavy metals from aqueous solutions: A critical review. Chemical Engineering Journal, 366, 608–621.

Yen, H.W., Chen, P.W., Hsu, C.Y., Lee, L., 2017. The use of autotrophic Chlorella vulgaris in chromium (VI) reduction under different reduction conditions. Journal of the Taiwan Institute of Chemical Engineers, 74, 1–6.

Yokwana, K., Kuvarega, A.T., Mhlanga, S.D., Nxumalo, E.N., 2018. Mechanistic aspects for the removal of Congo red dye from aqueous media through adsorption over N-doped graphene oxide nanoadsorbents prepared from graphite flakes and powders. Physics and Chemistry of the Earth, 107, 58–70.

Yuan, X., Li, J., Luo, L., Zhong, Z. and Xie, X., 2023. Advances in sorptive removal of hexavalent chromium (Cr(VI)) in aqueous solutions using polymeric materials. Polymers, 15, 388.

Zafar, M.A., Varghese, O.K., Robles Hernandez, F.C., Liu, Y., Jacob, M. V., 2022. single-step synthesis of nitrogen-doped graphene oxide from aniline at ambient conditions. ACS Applied Materials & Interfaces, 14, 5797–5806.

Zhang, Lei, Li, Y., Zhang, Li, Li, D.W., Karpuzov, D., Long, Y.T., 2011. Electrocatalytic oxidation of NADH on graphene oxide and reduced graphene oxide modified screen-printed electrode. International Journal of Electrochemical Science, 6, 819–829.

Zhang, X., Yi, G., Zhang, Z., Yu, J., Fan, H., Li, P., Zeng, H., Xing, B., Chen, L., Zhang, C., 2021. Magnetic graphene-based nanocomposites as highly efficient absorbents for Cr(VI) removal from wastewater. Environmental Science and Pollution Research, 28, 14671–14680.

Zhou, J.L., Yang, L., Huang, K.X., Chen, D.Z., Gao, F., 2022. Mechanisms and application of microalgae on removing emerging contaminants from wastewater: A review. Bioresource Technology, 128049.

Zhou, S., Gao, J., Wang, S., Fan, H., Huang, J., Liu, Y., 2020. Highly efficient removal of Cr(VI) from water based on graphene oxide incorporated flower-like MoS_2 nanocomposite prepared in situ hydrothermal synthesis. Environmental Science and Pollution Research, 27, 13882–13894.